Mesoscopic quantum interference experiments in InGaAs and GaAs two-dimensional systems

Shaola Ren

Dissertation submitted to the Faculty of the
Virginia Polytechnic Institute and State University
in partial fulfillment of the requirements for the degree of

Doctor of Philosophy
in
Physics

Jean J. Heremans, Chair
Levon V. Asryan
Victoria G. Soghomonian
Vito W. Scarola

May 1, 2015
Blacksburg, Virginia

Keywords: quantum interference, Aharonov-Bohm oscillations, mesoscopic systems, weak localization, two-dimension, InGaAs, GaAs

Copyright 2015, Shaola Ren

Mesoscopic quantum interference experiments in InGaAs and GaAs two-dimensional systems

Shaola Ren

(ABSTRACT)

The study of quantum interference in solid-state systems yields insight in fundamental properties of mesoscopic systems. Electron quantum interference constitutes an important method to explore mesoscopic physics and quantum decoherence. This dissertation focuses on two-dimensional (2D) electron systems in $\delta-$Si doped n-type $In_{0.64}Ga_{0.36}As/In_{0.45}Al_{0.55}As$, 2D hole systems in Si-doped p-type $GaAs/Al_{0.35}Ga_{0.65}As$ and C-doped p-type $GaAs/Al_{0.24}Ga_{0.76}As$ heterostructures. The low temperature experiments study the magnetotransport of nano- and micro-scale lithographically defined devices fabricated on the heterostructures. These devices include a single ring interferometer and a ring interferometer array in 2D electron system, Hall bar geometries and narrow wires in 2D hole systems. The single ring interferometer yields pronounced Aharonov-Bohm (AB) oscillations with magnetic flux periodicity of h/e over a wide range of magnetic field. The periodicity was confirmed by Fourier transformation of the oscillations. The AB oscillation amplitude shows a quasi-periodic modulation over applied magnetic field due to local magnetic flux threading through the interferometer arms. Further study of current and temperature dependence of the amplitude of the oscillations indicates that the Thouless energy forms the measure of excitation energies giving quantum decoherence. An in-plane magnetic field was applied to the single ring interferometer to study the Berry's phase and the Aharonov-Casher effect. The ring interferometer array yields both AB oscillations and Altshuler-Aronov-Spivak (AAS) oscillations, the latter with magnetic flux periodicity of h/2e. The AAS oscillations require time-reversal symmetry and hence can be used to qualify time-reversal symmetry breaking. More importantly, the fundamental mesoscopic dephasing length associated with time-reversal symmetry breaking under applied magnetic field, an effective magnetic length, can be obtained by the analysis of the AAS oscillations over magnetic field. A theoretical model for confined ballistic system is confirmed by experimental data fitting. The AAS oscillations are barely resolved above 0.16 T and their amplitude decays with increasing magnetic field. The AB oscillations exist till above 2 T and their amplitude doesn't show the monotonic decay with increasing magnetic field. The different behavior of the AAS and AB oscillations originates in the different symmetries, respectively temporal and spatial, that they are sensitive to. The p-type 2D GaAs system has strong spin-orbit interaction (SOI). Antilocalization in a Hall bar geometry was analyzed by the 2D Hikami-Larkin-Nagaoka (HLN) theory to obtain the spin coherence time and phase coherence time. The 2D hole systems we studied have low density and high mobility, quite different from the 2D electron systems. These high-quality 2D hole systems demonstrate semi-classical ballistic phenomena in mesoscopic structures preferentially to quantum-coherence phenomena.

This work received support from DOE DE-FG02-08ER46532.

Acknowledgments

I wish to express my thanks to my advisor Prof. Jean J. Heremans who gave me insightful guidance and tremendous freedom in my research and study. Without his support, I could not be able to pursue what I am interested in. I wish to thank Prof. Victoria Soghomonian whose insightful suggestions led to the publications of my work and what I present here. I wish to thank Donald Leber for the help with the RIE. I wish to thank all the committee members, Prof. Jean J. Heremans, Prof. Levon V. Asryan, Prof. Victoria G. Soghomonian, and Prof. Vito W. Scarola for serving on my committee. I wish to thank Dr. Yao Zhang who helped me transfer helium for my experiments. I am thankful to all of my lab colleagues, Dr. Yao Zhang, Dr. Yong-Jae Kim, Dr. Martin Rudolph, Lingling Xu, Dr. Qifan Yuan, and Yuantao Xie, for the discussions we have shared and the help they have provided over the years. I would like to thank the following for financial support throughout my doctoral studies: the graduate school for a 2010 Ph.D. fellowship, and the Department of Energy Office of Basic Energy Sciences, Division of Materials Sciences and Engineering under award DOE DE-FG02-08ER46532. Some of the materials growth was supported by the National Science Foundation under award DMR-0520550 and DMR-1207537.

Contents

1 Introduction **1**

1.1 2D electron system and 2D hole system 2

1.2 Aharonov-Bohm effect, Aharonov-Bohm and Altshuler-Aronov-Spivak oscillation 2

1.3 Berry's phase 4

1.4 Aharonov-Casher effect 5

1.5 Thouless energy 5

1.6 Weak localization and weak antilocalization 6

1.7 Universal conductance fluctuations 8

2 Fabrication **9**

2.1 Photolithography 9

2.1.1 Preparation 9

2.1.2 Photolithography 12

2.1.3 Wet etching 13

2.2 E-beam lithography 14

2.2.1 Pattern design 15

2.2.2 Preparation 17

2.2.3 E-beam lithography and SEM 17

2.2.4 Inductively coupled plasma reactive-ion etching (ICP RIE) 20

2.3 Contacts and wires 21

2.4 Depositing a thin film on sample's surface 24

3 Measurement setup **27**
3.1 Overview 27
3.2 Cooldown 29
3.3 Techniques of measurements 31
3.3.1 Instruments and programs 31
3.3.2 Improving performance of a sample 34

4 Electron interference in InGaAs/InAlAs **36**
4.1 Introduction 36
4.2 P122 n-type InGaAs/InAlAs, sample pattern design and devices 37
4.3 Overview of experiment 42
4.4 Single AB ring 44
4.4.1 A general view of AB oscillations of a single AB ring 44
4.4.2 AB oscillations of a single AB ring at low magnetic field 47
4.4.3 AB oscillations of a single AB ring at higher magnetic field 50
4.4.4 Current and temperature dependence of the AB oscillations in single AB ring 50
4.4.5 Spin-orbit Interaction and linear Rashba coefficient α 54
4.4.6 Applying in-plane magnetic field to single AB ring 56
4.4.7 In-plane Zeeman effect induced Berry's phase and Aharonov-Casher phase change in single AB ring 56
4.5 AB ring array 66
4.5.1 Overview of AB and AAS oscillations in AB ring array 66
4.5.2 AAS oscillations at different magnetic field regime 70
4.5.3 Magnetic dephasing length $L_B(B)$ and time-reversal symmetry breaking 76
4.5.4 Phase coherence length in an AB ring array 79
4.6 Mounting LED to improve device performance 80

5 Hole system in p-type GaAs/AlGaAs **82**
5.1 M423 and 94121 hole systems 82

5.2 Pattern design and fabricated devices 84
5.3 Results and discussion 87
5.3.1 Hall bar and wires on material M423 89
5.3.2 Hall bar and thin wire on material 94121 99
5.3.3 Antidot array on material 94121 102

6 Conclusions **104**

Bibliography **107**

List of Figures

1.1 Schematic experiment to demonstrate the AB effect, modified from [1]. . . . 3

1.2 Schematic image to demonstrate weak localization in a disordered system with randomly distributed scatters, two opposite directed backscattering loops A_i and A_j are depicted. 6

2.1 Fabrication process sequence diagram. For some blocks if the process is good enough the forward path is used, otherwise the backward path is used. Sometimes, the dashed line sequence alternates the corresponding solid line sequence. 10

2.2 Sample cutting process 11

2.3 Photo-lithography machine in a cleanroom with safe yellow light, it contains a movable stage, a UV light source, a microscope view system and a control module. 12

2.4 Schematic of the photolithography process, sequentially from (a) to (f), (a) a cleaned sample material; (b) AZ5206 is spun on the sample surface; (c) mask is contacted on the sample, and they are exposed to UV light for a while; (d) development is done, pattern is transfered to sample temporarily; (e) wet etching is done, pattern is transfered to sample permanently; (f) AZ5206 is lift-off from the sample's surface. 15

2.5 A pattern designed by DesignCAD. 16

2.6 E-beam lithography setup, it's an SEM integrated with an electron beam control module. 18

2.7 ICP RIE etched edge, the darker area is the etched part, the edge is defined well. 21

2.8 Home made annealing station. 22

2.9 A full-fledged device and a coin, the coin is used to give an eye guide for the size of device 23

2.10 Circuit for contacts testing 23

2.11 Schematic procedure of depositing a pattern on sample's surface, sequentially from (a) to (c). (a) define a pattern on resist by photolithography or e-beam lithography, (b) deposit intended material onto sample's surface, (c) lift-off resist, and pattern is transfered to sample's surface. 25

2.12 A thermal evaporator. 26

3.1 Measurement system. In the left photograph, the Janis dewar and associated electronic instruments to supply power and magnetic field, measure the sample and monitor the system are shown. The right photograph shows the ^{3}He system (home built). 28

3.2 (a) Schematic graph of the intersection view of the cryogenic system. (b) The inner probe with a sample mounted on its tip. In experiments, it is inserted into the central tube of the setup shown in (a). 28

3.3 A typical cooldown trial of an n-type heterostructure device, resistance versus temperature. 30

3.4 Constant current source, consisting of a low noise lock-in amplifier and a set of high resistance resistors. Switch is used to select a different resistor (1 MΩ, 10 MΩ or 100 MΩ) to obtain a different current. The 10 kΩ resistor and its shorting switch are used to test the current value when necessary. 31

4.1 Schematic structure of P122 n-type InGaAs/InAlAs. 37

4.2 The designed pattern is used for a device named "R082410". 38

4.3 The design pattern of the single AB ring, this is the central and essential part of the real pattern, the omitted outer part can be varied according to different photolithography pattern. The central light purple shadowed ring is design as electron conducting channel with width 300 nm, which is the AB ring effectively. This design is used for a device named "R082410". 38

4.4 The designed pattern of a 5×5 array of AB rings, This design is for the device "InGaAsL CoFe2b". The upper part shows the whole view, the lower part emphasizes the ring array. For each ring, the dimensions are the same dimension as Fig. 4.3, other size information is detailed in text. 39

4.5 The designed pattern for a device named "R20110929a". Each ring has the same dimension as in Fig. 4.3. The yellow middle bar separates the ring array into two groups. Combining with the photo-lithography pattern, these two groups can work independently. 40

4.6 The design of the array part of the device "R20110929a". Each ring has the same dimension as in Fig. 4.3. The left and right ring arrays can perform independently. In the real device, the left ring array is covered by ferromagnetic CoFe. 40

4.7 The SEM image of an AB ring with dimension slightly different from Fig. 4.7. This image was obtained from a sample after e-beam lithography but without dry etching. A gold layer is sputtered on the PMMA pattern. 41

4.8 The SEM image of an AB ring array, its dimension is the same as Figure 4.4. This image was taken from a sample after dry etching. 41

4.9 The SEM image of AB ring arrays, its dimension is the same as Figure 4.5 and 4.6. This image was taken from a sample after dry etching and with the left part covered by CoFe which is deposited by thermal physical vapor deposition. 42

4.10 Schematic view of device "R082410". The pattern on the Hall bar is the same as Fig. 4.2 rotated by 90 °, the "L" shaped Hall bar was fabricated by photolithography. The distance between leg 2 and leg 3 is 160 μm, and the width of the Hall bar is 80 μm. 43

4.11 Schematic view of device "InGaAsL CoFe2b". The pattern is the same as the upper part of Fig. 4.4 rotated by 90 °, and Hall bar was fabricated by photolithography. The distance between leg 2 and leg 3 is 40 μm, and the width of the Hall bar is 50 μm. 43

4.12 Schematic view of device "R20110929a". The pattern is the same as Fig. 4.5, and Hall bar was fabricated by photolithography. The distance between leg 2 and leg 3 is 40 μm, and the width of the Hall bar is 50 μm. 43

4.13 Measurement configuration of a Hall bar. 44

4.14 Schematic view of the 4-terminal measurement configuration of a single AB ring. A perpendicular magnetic field is applied. 45

4.15 A schematic electron interferometer which can perform AB effect. 45

4.16 Measured Aharonov-Bohm magnetoresistance oscillations at 0.4 K, as ring resistance $R(B)$ versus B. Panels (a) and (b) show the ring magnetoresistance over smaller ranges of B than panel (c) which emphasizes a view of the modulation with B. 46

4.17 Aharonov-Bohm magnetoresistance oscillations around $B = 0$ at 0.4 K. Panel (a) shows the raw data, Panel (b) shows the data after background removal. Panel (c) contains the Fourier transform of (b), where h/e and $h/(2e)$ modes are indicated in the frequency spectrum. 47

4.18 Black solid oscillatory line: the autocorrelation function in B of the Aharonov-Bohm oscillations in Fig. 4.10(b). Red open circles $\circ$: the maxima of the autocorrelation function, as a guide to the autocorrelation function envelope. Blue line with open squares $\square$: the fit to the autocorrelation function envelope, using the red open circles. The use of a finite range of B leads to deviations between fit and data at higher ΔB as discussed in the text. 49

4.19 Modulation in the amplitude of Aharonov-Bohm oscillations simulated by using the 3 discrete frequencies deduced from the Fourier tansform in Fig. 4.10(c): 376 1/T, 408 1/T, 447 1/T, with intensities 13.2 Ω, 21.6 Ω, 5.89 Ω respectively. 50

4.20 The ring magnetoresistance at 0.4 K over B from -0.6 T to 0.6 T. The Aharonov-Bohm magnetoresistance oscillations (not fully resolved on the scale of the graph) ride on universal conductance fluctuations. The inset shows a selected narrow range of B around 0.57 T to resolve the oscillations. 51

4.21 The excitation current dependence of the Aharonov-Bohm magnetoresistance oscillations at 0.4 K (data from the same sample as before, yet a different cool-down than for Figs. 4.9, 4.10 and 4.20). From top to bottom, the excitation current (rms values) is 5 nA, 10 nA, 20 nA, 50 nA, 100 nA, 200 nA and 500 nA respectively. Curves are offset, actual $R(B = 0) \approx 2.5$ kΩ. 52

4.22 The T dependence of the Aharonov-Bohm magnetoresistance oscillations at 20 nA (data as in Fig. 4.21 from the first sample, yet a different cool-down than for Figs. 4.9, 4.10 and 4.20). From top to bottom T is 0.4 K, 0.6 K, 0.8 K, 1.0 K, 1.2 K, 1.4 K and 1.6 K respectively. Curves are offset, actual $R(B = 0) \approx 2.5$ kΩ. 53

4.23 The excitation current and T dependence of the amplitude of the Aharonov-Bohm magnetoresistance oscillations (open squares $\square$ and filled circles $\circ$ represent data from the first sample at different cooldowns). Panel (a) shows the excitation current dependence at 0.4 K with a logarithmic scale on both axes. Panel (b) shows the T dependence at 20 nA with a logarithmic scale on the vertical axis. 54

4.24 Fourier spectrum of Shubnikov-de Haas oscillation in the heterostructure InGaAs/InAlAs (Hall bar) at 0.4 K. The two peaks marked with “spin down” and “spin up” are the two frequencies of the Shubnikov-de Haas oscillations when plotted versus $1/B$. The inset shows the Shubnikov-de Haas oscillations up to 9 T. 55

4.25 A schematic graph of the tilted setup. 56

4.26 A schematic view of an AB ring with spin-orbit interaction. E is the effective electric field given by SIA of heterostructure. The inset depicts the spin splitting at Fermi surface due to SOI. In the dashed box, electrons propagate in two directions, the electrons' states can be described by the two circled positions in k space at the inset, and B_{SOI} is the effective magnetic field from SOI. The spin direction is parallel to B_{tot} due to the Zeeman effect, B_{tot} is the total magnetic field one electron feels. This graph only describes the case for one spin direction with a counterclockwise motion. 57

4.27 Schematic demonstration of AC effect. (a) and (b) demonstrate the same physics. For clarity, non orthogonal states for spin up and down are both shown in (a) and (b). Taking (a) as an example, it's a typical AB ring. Two electron waves propagate from the entrance point to the exit position through the left and right arms. The electron propagates through the left arm with spin up, the state is denoted as $\psi_-^\uparrow$. The electron propagates through the right arm with spin down, the state is denoted as $\psi_+^\downarrow$. $k_+/-$ denotes the propagating directions, k_+ means counterclockwise, k_- means clockwise. $\sigma^{+/-}$ denotes the spin directions, σ^+ means spin up, σ^- means spin down. The magnetic moment $\boldsymbol{\mu}$ is determined by spin $\boldsymbol{\sigma}$. The effective vector potential is determined by $\boldsymbol{\mu} \times \mathbf{E}$, where $\mathbf{E}$ is the effective electric field due to SOI. $\psi_-^\uparrow$ accumulates negative AC phase when it reaches exit point, $\psi_+^\downarrow$ accumulates positive AC phase when it reaches exit point. 58

4.28 Measurements in a tilted setup as depicted in Fig. 4.25. The tilt angle β varies between 6° and 90° from top to bottom. In-plane magnetic field is $B_\parallel = B_\perp/\tan\beta$. The curves background was removed and curves' vertical positions are offset for clarity. (a) are results around 0 T, (b) are results around 0.15 T. Shadowed stripes on curves indicate a group of AB oscillations. As we discussed in [48], strong correlation is within a region of 0.007 T for $B_\perp$ averagely. There is no meaning to compare oscillations horizontally, only but vertically in each shadowed stripe. The total field is greater than 0.5 T in the regions marked with solid boxes. The value 0.5 T is obtained by setting the Zeeman energy to equal the Thouless energy. 62

4.29 The figures are related to the 90° curve in Fig. 4.28(a). (a) depicts the relation of $\phi_{Berry} + \phi_{AC}$ and θ (Eq. 4.5). In (b), the red solid curve shows the value of $\cos(\phi_{\text{Berry}} + \phi_{\text{AC}})$, with $\phi_{Berry} + \phi_{AC}$ obtained in (a); the black line with dots shows the normalized oscillation amplitudes obtained from the 90° curve in Fig. 4.28(a), corresponding to the right vertical axis. 63

4.30 The figures are related to the 90° curve in Fig. 4.28(b). (a) depicts the relation of $\phi_{Berry} + \phi_{AC}$ and θ (Eq. 4.5). In (b), the red solid curve shows the value of $\cos(\phi_{\text{Berry}} + \phi_{\text{AC}})$, with $\phi_{Berry} + \phi_{AC}$ obtained in (a); the black line with dots shows the normalized oscillation amplitudes obtained from the 90° curve in Fig. 4.28(b), corresponding to the right vertical axis. 64

4.31 Fourier spectrum of the measurements in Fig. 4.28. (a) is for Fig. 4.28(a), and (b) is for Fig. 4.28(b). These Fourier spectrum curves are offset vertically for clarity. 65

4.32 (a) Mach-Zehnder (MZ) interferometer, based on trajectories in spatially separate arms. (b) Sagnac-type interferometer, based on exact time-reversed trajectories (for clarity, trajectories are shown spatially non-overlapping). . . 67

4.33 Schematic graph to show local flux and non-local flux, the red ring area is electron path, the green central area excludes electrons. 67

4.34 AB effect in a chain of rings, the first ring splits the original electron beam into two branches, before they travel to the second ring, these two branches unite into a new electron beam. Solid dark blue lines depict one most likely electron path, dashed red lines depict another choice of electron path. 68

4.35 A schematic description of AAS oscillations in an AB ring. The solid green line and dashed red line indicate the two directed paths of electrons, they are time-reversed states of each other. A magnetic field is applied uniformly across the rings' surface. 69

4.36 Schematic view of the measurement configuration of a 5×5 AB ring array. . 70

4.37 AB oscillations in a 5×5 AB ring array at magnetic fields from 0.2 T to 1.4 T. 71

4.38 AB oscillations in a 5×5 AB ring array at magnetic fields from 1.4 T to 2.3 T. 72

4.39 AAS and AB oscillations in a 5×5 AB ring array at magnetic fields from -0.1 T to 0.2 T. AAS oscillations are stronger in panel (a) than panel (b). 73

4.40 Fourier transformation of AAS and AB oscillations in the interferometer array. Fourier spectrum in (a) is for magnetic field -0.02 T to 0.02 T, (b) 0.02 T to 0.06 T, (c) 0.06 T to 0.10 T, (d) 0.10 T to 0.14 T, (e) 0.14 T to 0.18 T, (f) 0.32 T to 0.36 T, (g) 0.84 T to 0.88 T, (h) 1.32 T to 1.36 T, (i) 1.80 T to 1.84 T and (j) 2.16 T and 2.20 T. As the magnetic field increases, the AAS oscillation component in Fourier spectrum becomes less, and invisible finally, however, the AB oscillation component is almost unchanged. 74

4.41 (a) R(B) versus B at low B spanning ± 200 G; (b) After removing the WAL positive magnetoresistance background from (a), AAS and AB oscillations clearly appear. (c) Fourier transform of the data in (a) with two peaks clearly marked out: the h/e peak corresponding to AB oscillation and the h/2e peak corresponding to AAS oscillation. 75

4.42 Fourier component amplitudes (arbitrary units) versus B ($B-$values determined as explained in the text). (a) AAS (h/2e) Fourier component versus B, illustrating the decay of AAS oscillations with increasing B. (b) AB (h/e) Fourier component versus B, illustrating the lack of monotonic decay of AB oscillations with increasing B. 75

4.43 Calculated values of l_B according to different models, f1 is Eq. 4.8, f2 is Eq. 4.9, f3 is Eq. 4.10, f4 is Eq. 4.11, f5 is Eq. 4.12 (curves for Eq.4.9 and Eq.4.10 mostly overlap for the present paramters and cannot be distinguished on the graph). The data labeled with f shows the values calculated from experimental data according to Eq. 4.13. Details about the method are explained in the text. . 78

4.44 The fit to Eq. 4.14 to extract phase coherence length l_ϕ. The inset shows the Aharonov-Bohm magnetoresistance oscillations used for the Fourier transform, itself depicted as the black solid line in the main graph. The red line with open circles depicts the fit to Eq. 4.14. 80

4.45 An LED is mounted on the device “R082410”. 81

5.1 Schematic structure of M423 Si-doped p-type GaAs/$Al_{0.35}Ga_{0.65}$. The 2DHS layer is located 100 nm beneath the surface. 83

5.2 Schematic structure of 94121 C-doped p-type GaAs/$Al_{0.24}Ga_{0.76}As$. The 2DHS layer is located 136 nm beneath the surface. 83

5.3 Optical microscope view of the device made from M423 and measurement configuration. The darker part is conducting, the light-colored parts are etched out by wet etching. A schematic measurement configuration and crystal directions are shown as well. 84

5.4 Optical microscope view of the wires patterned on the chip. The 10 parallel wires appear as 10 lines in this image as the resolution of the optical microscope is unsufficient. 85

5.5 SEM view of part of the wire pattern with dimensions. The darker parts are etched out by ICP RIE, the light-colored part is conducting. 85

5.6 Optical microscope view of the device made from 94121 and measurement configuration. 86

5.7 SEM view of the narrower wire on the 94121 device. 87

5.8 A design of antidot array, each square is an antidot. The side length of each square if 0.5 μm, the spatial periodicity of this antidot array is 1.2 μm, the separation between antidot is 0.7 μm. The whole design can cover more than 160 μm $\times$ 80 μm area, this view is part of the whole pattern. 87

5.9 Optical microscope view of the pattern in Fig. 5.8 on a Hall bar after e-beam lithography. 88

5.10 SEM view of the antidot array, the pits are the antidots. As stated in Fig. 5.8, each antidot has a size of 0.5 μm $\times$ 0.5 μm, the spatial periodicity of this antidot array is 1.2 μm. 88

5.11 Shubnikov-de Haas oscillations on a Hall bar on material M423 along direction $[01\bar{1}]$ at 0.4 K. The inset graph shows the measurement setup, the red lines indicate the corresponding filling factors. 89

5.12 Shubnikov-de Haas oscillations of a Hall bar on material M423 along direction $[01\bar{1}]$ and on wires along direction $[\bar{2}33]$ below 2 T at 0.4 K. 90

5.13 Fourier transform of the SbdH oscillations in Fig. 5.12. 90

5.14 Temperature dependence of antilocalization of a Hall bar along $[00\bar{1}]$. Temperature varies from 0.4 K to 3.0 K, each curve is offset for clarity. The actual value of R_{xx} is about 200 Ω at $B = 0$. 92

5.15 Metallic behavior of resistivity of M423 at low temperatures. 92

5.16 One HLN fit for the data of antilocalization on a Hall bar n material M423 at 0.4 K. 94

5.17 Temperature dependence of τ_{SO} and τ_{ϕ}. 94

5.18 Intra-subband scattering rates K_1 and K_2 versus temperature T. The red line is a parabolic fit of temperature. 95

5.19 Inter-subband scattering rates K_{12} versus temperature T. An exponential model is applied to the data to obtain the activation characteristic energy between the two subbands. 96

5.20 Temperature dependence of magnetoresistance of Q1D wires. Temperature varies from 0.4 K to 3.0 K, curves are offset for clarity. The typical value of R is about 800 Ω at zero magnetic field. 98

5.21 1D antilocalization fit of experimental data. Inset shows the measurement configuration. 98

5.22 Quantum Hall effect in 94121 p-type C-doped GaAs/$Al_{0.24}Ga_{0.76}As$ heterostructure at 0.4 K, lower red line shows the result collected from the sample without back gate, upper blue line shows the result collected from the sample with back gate. Filling factors are marked on the corresponding plateaus. The inset graph shows the measurement configuration. 99

5.23 Magnetoresistance of the 2 μm width wire with magnetic field from 1 T to 4 T at different temperatures 2.0 K, 1.0 K and 0.4 K corresponding to curves from up to down. The inset shows the measurement configuration. The shadowed part is analyzed by autocorrelation in order to figure out the phase coherence length l_ϕ. 100

5.24 The autocorrelation function over magnetic field from 2.8 T to 3.0 T of a Q1D wire at different temperatures 0.4 K, 1.0 K and 2.0 K. 101

5.25 Calculated δG (a) and phase coherence length l_ϕ (b) versus T. 101

5.26 Ballistic transport peaks after subtracting a quadratic background at different temperatures of the grid area. From top to bottom: 0.4 K, 0.5 K, 0.7 K, 1.2 K, 1.7 K, 1.9 K, 3.0 K. 103

5.27 Temperature dependence of the relative ballistic scattering rate $\Delta(1/\tau_\beta)$ defined as Eq. 5.14. The red solid line is a quadratic fit to the data. 103

Chapter 1

Introduction

Phase is an important variable in quantum interference. In phenomena related to quantum magnetotransport, the quantum phase associated with the wave function of the carriers in the system determines the properties of the specific system. In classical physics, although phase term of a wave contains information, people prefer to use other mechanical terms to describe the properties of a classical wave. However, in quantum physics, phase is indispensable. The discussion of a quantum system is based on wave functions, and the interactions in a quantum system reflects the quantum phase.

The Aharonov-Bohm (AB) effect is a famous phenomenon related to phase, and is an important method to study quantum interference in magnetotransport experiment. Other similar effects include Altshuler-Aronov-Spivak (AAS) oscillations, Berry's phase and Aharonov-Casher (AC) effect. Weak localization (WL) and universal conductance fluctuations (UCFs) are also phenomena related to phase in disordered system.

In quantum physics, sometimes we have to involve spin or magnetic moments to explain a phenomenon: Berry's phase, AC effect, Zeeman effect and weak antilocalization (WAL) are such examples.

In this dissertation, chapters 4 and 5 discuss experiments about the above mentioned phenomena. The materials we use in the experiments are several kinds of III-V semiconductors, which all have a 2-dimensional (2D) system which is either a 2D electron system or a 2D hole system buried beneath the material's surface. Chapters 2 and 3 state the techniques of fabrication and measurements. Chapter 6 is a summary of the whole research. The following gives a brief introduction to the basic knowledge used in this study.

1.1 2D electron system and 2D hole system

The study of this dissertation used 2D electron systems and 2D hole systems, formed in quantum well layers in heterostructure. With molecular beam epitaxy and micro- or nano-scale fabrication techniques, 2D systems became a useful tool to study fundamental physics.

Here, some concepts in 2D systems used widely in this dissertation are introduced. We call the systems we studied mesoscopic systems, greater than the atomic size but still maintains the property of quantum interference. The carriers of an electron system are electrons, the carriers of a hole system are holes.

The mean free path l_e can be understood as the length one carrier can pass before an elastic scattering happens. We calculate it as $l_e = v_F \tau_e$, where v_F is the Fermi velocity, τ_e is time between two elastic scattering events of one carrier.

The phase coherence length l_ϕ depicts the length one carrier can pass before it loses its phase information. Phase coherence time is τ_ϕ, and $l_\phi = \sqrt{D\tau_\phi}$, where D is the diffusion constant. In 2D systems, D is obtained as $D = \frac{1}{2} v_F l_e$. Sometimes τ_ϕ is interpreted as the inelastic scattering time.

The spin-orbit interaction length l_{SO} depicts the length one carrier can pass before a spin-orbit coupled state is altered by scattering; τ_{SO} is the time between two such scattering events of one carrier, and $l_{SO} = \sqrt{D\tau_{SO}}$.

The magnetic length l_m is defined as $l_m = \sqrt{\hbar/eB}$, which means in a presented magnetic field B, when a carrier encloses an area l_m^2, due to AB effect. It will pick up a unity phase of 2π.

The magnetic dephasing length L_B means the effective magnetic length in a confined system. In a confined system, the property of the geometry boundary should be counted in the calculation of L_B besides l_m.

The effective coherence length L_C combines the effects of l_ϕ and L_B, $L_C = \sqrt{l_\phi^{-2} + L_B^{-2}}$.

1.2 Aharonov-Bohm effect, Aharonov-Bohm and Altshuler-Aronov-Spivak oscillation

AB effect was first discussed by Aharonov and Bohm in late 1950's [1] and early 1960's [2]. It is a non-local non-trivial effect given by electromagnetic potentials. They initially suggested a setup as showed in Fig. 1.1. The Hamiltonian of an electron in such a setup can

be expressed as

$$H = \frac{[\mathbf{P} - e\mathbf{A}]^2}{2m} \tag{1.1}$$

where A is the vector potential given by magnetic field and $\nabla \times \mathbf{A} = 0$. In singly connected regions, the solution of this Hamiltonian can be expressed as

$$\psi = \psi_0 e^{-iS/\hbar} \tag{1.2}$$

where ψ_0 is the solution when $\mathbf{A} = 0$, and $\nabla S/\hbar = e\mathbf{A}$. For the setup in Fig. 1.1, the wave function splits into two parts $\psi = \psi_1 + \psi_2$, where ψ_1 and ψ_2 represent electron beam on the two paths respectively. According to [1], the phase difference between the two beams is

$$(S_1 - S_2)/\hbar = (e/\hbar) \oint_C \mathbf{A} \cdot d\mathbf{r} = (e/\hbar)\phi \tag{1.3}$$

where ϕ is the magnetic flux threading through the area enclosed by the two electron beams. Thus even when there is no magnetic field in the electron paths B and C, a non-trivial effect is generated at F with a non-local magnetic field. This is the AB effect. When the magnetic field varies, the probability of electrons at F varies as well, and this is the origin of the AB oscillations discussed in this dissertation.

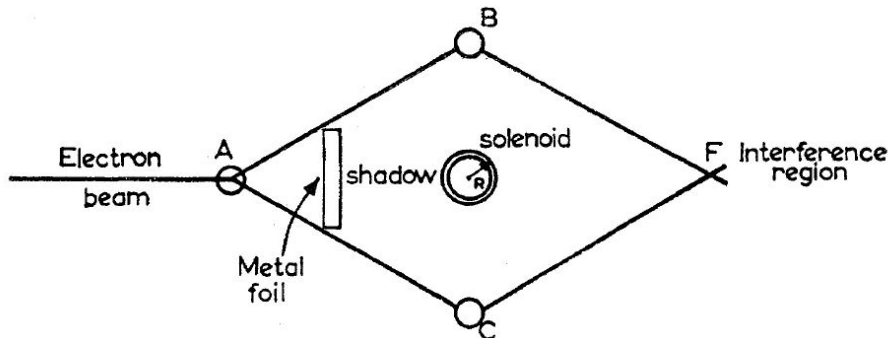

Figure 1.1: Schematic experiment to demonstrate the AB effect, modified from [1].

Experiments about the AB effect were first demonstrated in electron microscopy in 1960's. More evidence of the AB effect were claimed in 1980's, where the methods including electron holography [4, 5, 6] and magnetotransport measurement in metal rings [7, 32]. The experiments using the electron microscope and electron holography are similar to the free electron double slit interference. The metal rings experiments are about transport measurements, validating the AB effect by an oscillation of the magnetoresistance of the metal rings over magnetic field. Later on, with the progress in material growth, theoretical advances [9, 10] and refined experiments [11] AB effect in micro- or nano- semiconductor structures appeared

in late 1980's and 1990's. Nowadays, the AB effect in a semiconductor is more likely to be used as a tool to study the properties of a system [12, 13, 34, 60]. I will discuss the Berry's phase [12, 13] in AB oscillations in chapter 4.

The experiments in metal rings [7, 32] are akin to our experiments, both are about magnetotransport measurements. Reference [7] in the literature discusses an experiment in a single submicron-diameter Au ring, where AB oscillations were observed. Reference [32] performed experiments in chains of submicron-diameter Au loops, where both AB and AAS [8] oscillations were observed at low magnetic field.

AB oscillations and AAS [8] oscillations are both based on the AB effect. The magnetic flux periodicity of AB oscillation is h/e, the magnetic flux periodicity of AAS oscillation is $h/2e$; the electron beams for AB oscillation enclose the inner area once and the electron beams for AAS oscillation enclose the inner area twice. AB oscillation is caused by the interference of two spatially separated electron beams, and AAS oscillations are caused by the interference of the electron beam and its time-reversed beam. This will be discussed in chapter 4.

1.3 Berry's phase

Berry's Phase [14] is a famous geometric phase in quantum mechanics. Berry's phase happens in an adiabatic system, whose Hamiltonian H is slowly altered in time. From [14], a quantum system in an eigenstate will acquire a geometrical phase $\gamma(C)$ in addition to the dynamical phase when this quantum system is slowly transported around a contour C by varying parameters $\mathbf{R}$ in its Hamiltonian $H(\mathbf{R})$. This geometrical phase $\gamma(C)$ is Berry's phase. There is a detailed discussion and derivation in [14], only results are quoted here. Generally, with the requirements stated above, a system in eigenstate $|n\rangle$ has a Berry's phase

$$\gamma_n(C) = i \oint_C \langle n(\mathbf{R}) \nabla_{\mathbf{R}} n(\mathbf{R}) \rangle \, d\mathbf{R} \tag{1.4}$$

after a contour C. Berry's phase is independent of how the contour is traversed as long as the process is slow enough to hold the adiabatic approximation.

More specifically, consider a particle with spin s in a slowly rotating magnetic field $\mathbf{B}$, whose Hamiltonian is

$$H(\mathbf{B}) = \kappa \hbar \mathbf{B} \cdot \mathbf{s} \tag{1.5}$$

where κ is a constant involving the gyromagnetic ratio and $\mathbf{s}$ is the spin vector. When the magnetic field fulfills a revolution, the accumulated Berry's phase is

$$\gamma_n(C) = -n\Omega(C) \tag{1.6}$$

where n denotes the eigenstate, and $\Omega(C)$ is the solid angle that C subtends. Equation 1.6 is used to discuss Berry's phase in one of the experiments in chapter 4. In our experiment,

a perpendicular magnetic field is applied externally, the 2D electron system has a strong spin-orbit interaction internally, and the electron traverses a circular contour. All those conditions fulfill the specific situation described above. When one electron traverses a full contour, the effective magnetic field it feels completes one revolution, a Berry's phase is accumulated in this process. However, in our experiments, one contour splits into two parts spatially without changing the physics describing above. More details are found in chapter 4.

A further explanation in [14] demonstrates that the AB effect is a special case of Berry's phase.

1.4 Aharonov-Casher effect

The AC effect [15] is like the AB effect and Berry's phase, they are all examples of topological quantum effects which are not caused by direct force interactions but "are manifested through the generation of relative phases which accumulate on the wave function of a particle moving though a non-simply-connected force-free region" [15]. The following content is from [15].

The AC effect happens to a particle with a magnetic moment traversing a contour in an effective electric field, no matter if the particle is charged or neutral. For a magnetic moment $\boldsymbol{\mu}$ in an electric field $\mathbf{E}$, the corresponding Hamiltonian is

$$H = \frac{[\mathbf{P} - (1/c^2)\boldsymbol{\mu} \times \mathbf{E}]^2}{2m} \tag{1.7}$$

so long as $\mu E \ll mv$, where $\nabla \times (\boldsymbol{\mu} \times \mathbf{E}) = 0$, similar to the situation of the AB effect. Thus a nontrivial phase is cumulated along the particle's moving path. The phase accumulated after a contour C is

$$\phi_{AC} = (1/\hbar c^2) \oint_C \boldsymbol{\mu} \times \mathbf{E} \cdot d\mathbf{r} \tag{1.8}$$

In our experiments, the 2D electron system has strong spin-orbit interaction, the electron's magnetic moment is determined by its spin, and the effective electric field is given by the structure inversion asymmetry of the heterostructure. Such a system satisfies the situation with a possible AC effect. A detailed discussion is in chapter 4.

1.5 Thouless energy

The Thouless energy [37] is a critical energy scale for phase decoherence by energy smearing in a finite system. The Thouless energy E_c is expressed as the eigenenergy change that would

cause a phase shift of 1 over a path length L [37]

$$E_c = \frac{\hbar}{\tau} = \frac{\hbar^2 k_F}{m_e^* L} \tag{1.9}$$

where $\tau = L/v_F$ is the traversal time, and k_F is the Fermi wavevector. The disturbance by thermal energy or electric potential to a quantum state is consistent with Thouless energy in our experiment. The thermal energy $k_B T$ leads to an uncertainty ΔE in a quantum state's eigenenergy (thermal smearing) and will lead to phase decoherence between electrons, due to a phase difference accumulated over a finite path length L. Equivalently, the excitation voltage V_{exc} generated across a system of resistance R and traversed by an excitation current I, will also lead to an energy smearing $\Delta E = eV_{exc} = eIR$.

If $\Delta E > E_c$, then $\Delta E/E_c$ independent and incoherent channels contribute to transport, averaging out the interference signal proportionally to $\sqrt{E_c/\Delta E}$ [40]. For AB oscillations, a reduction in the amplitude prefactor A_0 is expected $\sim \sqrt{E_c/\Delta E}$. For thermal excitation, a value $\kappa > 1$ is used in the expression of ΔE as $\Delta E = \kappa k_B T$, since averaging occurs if the thermally accessible energy range ΔE is sufficiently wide to give rise to a significant number of statistically independent Thouless energy intervals E_c. We adopt $\kappa \approx 3$ as suggested in [38].

1.6 Weak localization and weak antilocalization

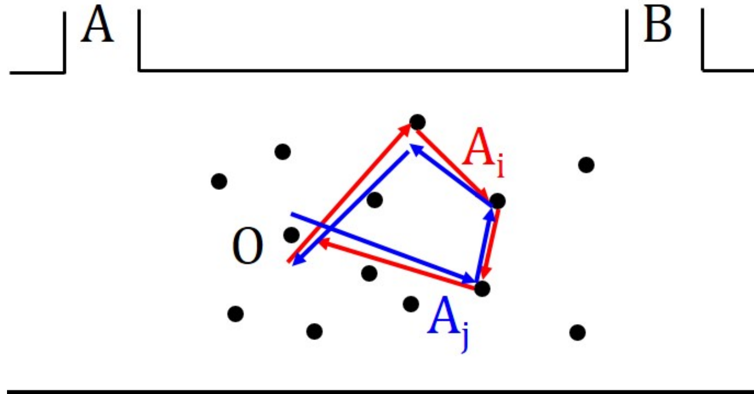

Figure 1.2: Schematic image to demonstrate weak localization in a disordered system with randomly distributed scatters, two opposite directed backscattering loops A_i and A_j are depicted.

Weak localization [16, 17] is a conductance correction in disordered systems. Considering a disordered system as showed in Fig. 1.2, the resistance between A and B can be altered by

the backscattering between the region of A and B. The following interpretation about weak localization is learned from [16, 17].

Consider the probability of an electron moving from $\mathbf{r_1}$ to $\mathbf{r_2}$ within time t, $P(\mathbf{r_1}, \mathbf{r_2}, t)$ is the squared sum of all probability amplitudes A_i for this propagation within t in a Feyman path description,

$$P(\mathbf{r_1}, \mathbf{r_2}, t) = |\sum_i A_i|^2 = \sum_i |A_i|^2 + \sum_{i \neq j} A_i A_j \tag{1.10}$$

When phases of A_i are uncorrelated, the interference term averages to 0. When we choose $\mathbf{r_1} = \mathbf{r_2}$, we can form time-reversed symmetric pairs of propagators to have identical paths. At zero magnetic field, the phases of each such paired propagators are identical, thus the interference between them is constructive. Figure 1.2 depicts such time-reversed symmetric propagators for two opposite directed backscattering loops. For a specific point, more than one such pairs exist, and those loops are coherent backscattering loops [17]. With a nonzero perpendicular magnetic field applied to the system, what happens to those paired loops is similar to the AAS oscillation, the phases of paired propagator are not identical any more. The phase difference picked up by each paired loop depends on the size of the loop. When the phase difference caused by magnetic field is small enough, the constructive interference weakens but doesn't disappear. As the magnetic field increases, once the phase difference picked up by the smallest loop reaches the order of π, the interference term of such time-reversal symmetric paired propagator averages to 0 as well. Thus, in a magnetotransport measurement of such a disordered system, in an R versus B graph, a peak around zero magnetic field can be observed. Such a phenomenon is weak localization. The above discussion is in the regime where the length of the backscattering loop is shorter than the phase coherence length l_ϕ.

Weak antilocalization happens in a disordered system, similar to the case described above, but where there is a spin-orbit interaction in the system, with the condition that the spin-orbit interaction length l_{SO} is comparable to the phase coherence length l_ϕ and the length of the backscattering loop [18]. Phenomenon of weak antilocalization in magnetotransport measurement is observed in a R versus B graph, with a valley around zero magnetic field caused by the spin-orbit interaction that weakens the constructive interference described above. A theoretical derivation to explain the effect given by spin-orbit interaction is in [77]. As weak localization, an increasing magnetic field gradually changes the property of the interference term; when the magnetic field is strong enough, the interference term averages to 0.

There are several models to describe weak localization and weak antilocalization in 2D and 1D confined systems which will be discussed in chapter 5.

1.7 Universal conductance fluctuations

The phenomenon of universal conductance fluctuations, UCFs, has been studied in mesoscopic systems in metals and semiconductors since 1980s. The magnetoresistance of small structures with UCFs has fluctuations [19, 20, 21] which are noise-like aperiodic signals. UCFs are a general phenomenon in mesoscopic systems, caused by quantum interference when the phase coherence length exceeds sample dimensions [22]. The feature of UCFs is independent of the sample size as long as the structures' dimensions don't exceed the phase coherence length. The conductance fluctuation amplitude is of the order of e^2/h ($4 \times 10^{-5}\Omega^{-1}$) [21, 95]. The detailed physical mechanism causing UCFs are discussed in the mentioned literature.

Autocorrelation function is used to analyze the correlation property of UCFs. As UCFs are a function of magnetic field, magnetoresistance $R(B)$ and magneto conductance $G(B)$ can both be used to construct an autocorrelation function. Here, we use $R(B)$ to demonstrate this method. Antocorrelation function $C(\Delta B)$ is expressed as

$$C(\Delta B) = \frac{\langle R(B)R(B + \Delta B)\rangle}{\langle R(B)^2\rangle} \tag{1.11}$$

where $\langle R(B)R(B+\Delta B)\rangle$ means ensemble average of $R(B)R(B+\Delta B)$. $C(\Delta B)$ is a decaying curve of ΔB. The critical magnetic field B_c is defined using $C(B_c) = 0.5C(0)$. B_c implies that when two values of $R(B)$ are separated larger than B_c, they are statistically independent of each other. UCFs are observed and discussed in detail in chapter 5.

Chapter 2

Fabrication

The materials we used in the experiments detailed in this thesis are InGaAs/InAlAs and GaAs/AlGaAs heterostructures, the details of the heterostructures will be presented in the relevant chapters. The effective part of these heterostructures for our electronic transport experiment is the two-dimensional quantum well layer introduced by doping; the quantum well is situated tens or hundreds of nanometers beneath the surface. We use a well developed fabrication process to define the designed pattern down to the quantum well layer. The generic process sequence is depicted in Fig. 2.1, and detailed description is stated in the following sections of this chapter.

2.1 Photolithography

In order to measure our mesoscopic devices, we use photolithography and electron-beam (e-beam) lithography to delineate pattern and contacts. Nowadays, photolithography is a mature technique in industry. We use a similar technique, which is a process used to transfer a pattern on a thin film. We use ultraviolet light to transfer a geometric pattern from a mask to a photon-sensitive chemical resist (photoresist) on a substrate. The following sections will talk about the whole process of photolithography.

2.1.1 Preparation

With the restriction of dimensions of the setup we used in measurements, samples we made, called chips, are smaller than 5×5 mm^2 typically, thus we need to cut a piece of rectangle material from a bigger wafer. The materials I handled are always brittle and the properties of their surface also tend to effect the following process critically, especially the photolithography and e-beam lithography; thus it's better to get sharp edges and clean surface for each

Figure 2.1: Fabrication process sequence diagram. For some blocks if the process is good enough the forward path is used, otherwise the backward path is used. Sometimes, the dashed line sequence alternates the corresponding solid line sequence.

piece of chip. In the whole course, a strict routine should be followed and processed in a cleanroom.

As Fig. 2.2 shows, (a) put a piece of graph paper on a cleanroom wiper, then cover the graph paper by a piece of lens paper, the graph paper is used to decide the size of a sample, and the lens paper is used to avoid scratches on the material wafer. The wafer is put on the lens paper in an upside -down way; (b) put a slice of clean glass with steep edge carefully on the back on the wafer, push it straight down to avoid sliding between these layers, meanwhile use a carbide pin to score along the glass edge on the backside of wafer, make sure a clean line is made on the wafer's back; (c) carefully remove the glass and flip the whole wafer to let surface be up using a tweezer, there may be scraps from the scratch, blow them away by a nitrogen (N_2) gun gently, then cover the wafer by a new piece of lens paper, and roll a glass rod over the top of lens paper to cleave the wafer along the scratch by pressure. You may cut the material several times to get the right size you want, however, be careful at each step, the smaller the piece is the harder for you to handle it.

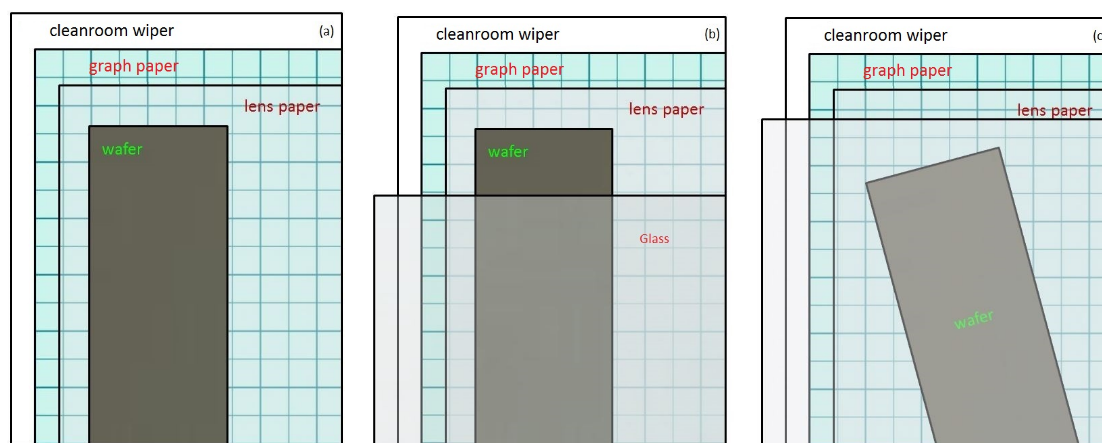

Figure 2.2: Sample cutting process

After we get a piece of material with appropriate size (sample), we need to clean it before any other operation. Three chemicals are needed, trichloroethylene (TCE) C_2HCl_3, acetone (ACE) $(CH_3)_2CO$ and isopropyl alcohol (IPA) C_3H_7OH. Soak the sample chip in TCE, ACE, IPA in sequence, 3 minutes for each step, then take the sample out from IPA, squirt its surface with IPA and blow it dry with a nitrogen gun gently. After this step, any possible organics deposited on the sample is mostly removed. Glue the sample to a piece of glass slide (about 18×18 mm^2) by AZ5206E photoresist (the purpose of gluing is to make the sample easier to handle), then bake in an oven at 90 °C for 30 minutes to ensure attachment. The next step is doing photo-lithography.

2.1.2 Photolithography

The mask (it's a copy of original mask which is made a commercial producer, this copy mask is a piece of glass with depth about 2 mm coated with FeO on one side) to define the pattern for photolithography is preprocessed, the dimension of the effective pattern is usually from several micrometers to several millimeter. The advantages of photo-lithography are the high efficiency and high successful rate comparing to e-beam lithography which will be discussed in a later section. The disadvantage is the resolution limitation caused by the wavelength of ultraviolet (UV) ligtht used in the process.

Chemical AZ5206 is a photon-sensitive material, it is a positive photoresist. To avoid exposure to unnecessary light, photolithography is operated in a cleanroom with safe yellow light. Photoresist AZ5206 is spun on a sample's surface at a speed of 4000 rpm for 40 s. After spinning, a thin layer of AZ5206 covers the sample's surface, then the sample is baked in a 90 °C oven for 30 min before doing photo-lithography.

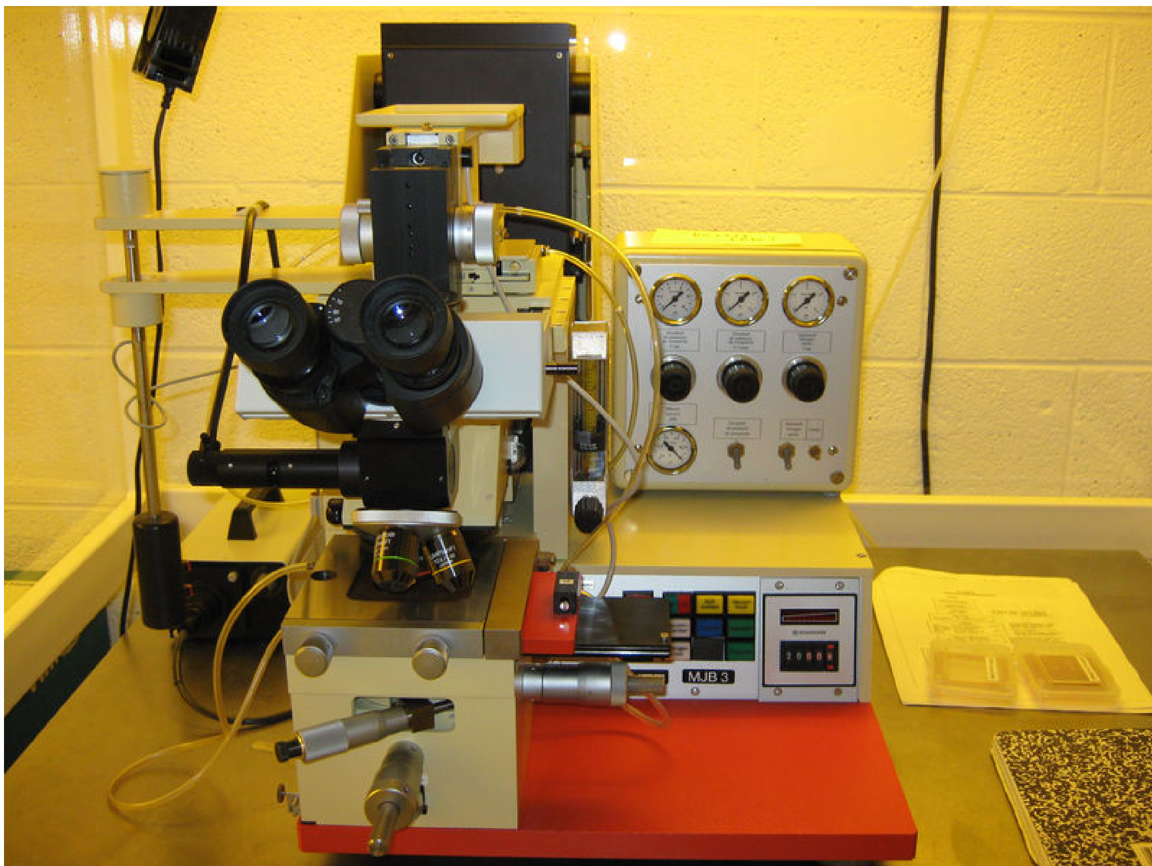

Figure 2.3: Photo-lithography machine in a cleanroom with safe yellow light, it contains a movable stage, a UV light source, a microscope view system and a control module.

Photolithography module is integrated with a microscope as Fig. 2.3 shows (Karl Suss,

model MJB3). The exposure and development time depend on the materials and setting of the machine. During my experiments, I used several different materials, and the UV light source power is always set to 275 W. For the n-type InGaAs, the exposure time is 23 s and the development time is between 12 s to 14 s. For the p-type GaAs, the development time is longer, usually around 15 s, sometimes up to 33 s; this depends on the result of the development which can be monitored by your eyes. The development gives a drastic change on the view of the material's surface when the developing time is long enough, the pattern appears gradually and the process can be stopped when the pattern is clear enough. The developer is a solution of a part AZ351 developer and 5 parts H_2O, and we used distilled water to rinse.

There are several tricks when doing photo-lithography. First, make sure that the sample's surface is contacting the mask solidly. This can be judged by Newton's ring; slowly rising the sample stage, Newton's ring appears on the surface of the sample when you look through the microscope when the sample's surface touches the mask. Second, when you separate the sample and the mask, make sure to lower down the sample stage a little before you do anything else. Third, after one time development, watch the sample under the microscope to check if the surface is clean and the edges of the pattern are sharp. If everything looks good then you can continue to do the next step, otherwise (such as there are some dirty dots or areas on the sample surface, most of the time this is because the development is not thorough enough) try to develop the sample several seconds additionally until it looks good enough.

Post baking is optional, it is also done in the 90 °C oven, time is 15 min.

2.1.3 Wet etching

When development is done, the pattern needs to be permanently transfered on the sample, wet etching can accomplish this task. For each material, a different etchant is used.

The principle to decide the etching time is to ensure that the etched depth is deeper than the quantum well in the chip. In this step, a relatively deeper etch is better. Generally the etched depth is around 2000 nm, as the depth of quantum well is several tens to several hundreds nanometers below the surface. The advantage of wet etching is that the operation is easy, the disadvantage is that the etched edged is more fuzzy comparing to dry etching which will be discussed in section 2.2.4.

For the material I used, the concrete recipes are showed below.

n-type InGaAs with InP cap, three steps:

1. $HCl : H_2O = 1 : 2$, 10 s.

2. $H_3PO_4 : H_2O_2 : H_2O = 1 : 1 : 38$, 120 s.

3. Distilled water rinse, usually several tens of seconds will be fine, I usually use 30 s.

n-type InGaAs withou InP, just two steps:

1. $H_3PO_4 : H_2O_2 : H_2O = 1 : 1 : 38$, 120 s.

2. Distilled water rinse, usually several tens of seconds will be fine, I usually use 30 s.

p-type GaAs, two steps:

1. $H_2SO_4 : H_2O_2 : H_2O = 1 : 8 : 40$, 18 s.

2. Distilled water rinse, usually several tens of seconds will be fine, I usually use 30 s.

It's a good habit to observe and record every thing that happens, use a microscope to watch the etched sample and take pictures, if everything is operated correctly as proposed, a good result is obtained and we move to the next step, which is to remove photoresist AZ5206 from sample's surface.

To remove the photoresist AZ5206:

1. Soak the sample in ACE for 1 hour, gently and carefully lift the sample off the piece of glass by a tweezer, avoid any scratch to the sample.

2. Soak the sample in another beaker with boiling ACE for 1 hour. This step is always operated on a hot plate with temperature set to 75 °C.

3. Soak the sample in another beaker with fresh ACE for 1 hour. To avoid the sample's surface becoming dry, spray ACE on the sample when taking the sample out of the boiling ACE before dropping it into the new beaker.

Figure 2.4 pictorially depicts photolithography from sample cleaning to AZ5206 lift-off sequentially from (a) to (f), explanations are detailed in figure's caption.

Generally, after the above steps, you will get a good sample with the pattern permanently printed on its surface. Sometimes, the result is not as expected. For example the surface is not etched, and the most probable reason is that the wrong side of the sample is used. It's easy to distinguish the right surface when one side of a wafer is polished and one is not, but sometimes, two sides of a wafer are both polished, and a wrong flipping during the cutting may cause this problem.

2.2 E-beam lithography

A mercury (Hg) lamp is the source of the UV light used, and the spectral lines are at 436 nm ("g-line"), 405 nm ("h-line") and 365 nm ("i-line") are used, the resolution of the product from photolithography cannot be infinity small. Another limitation of photo-lithography is that the mask of a pattern is fixed, if a small change is needed then a new mask is required.

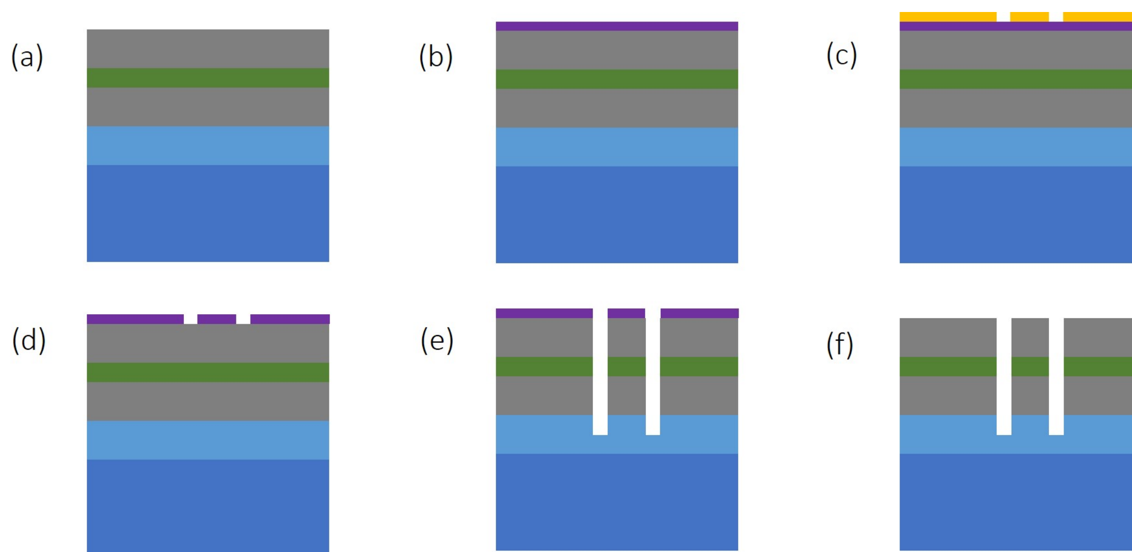

Figure 2.4: Schematic of the photolithography process, sequentially from (a) to (f), (a) a cleaned sample material; (b) AZ5206 is spun on the sample surface; (c) mask is contacted on the sample, and they are exposed to UV light for a while; (d) development is done, pattern is transfered to sample temporarily; (e) wet etching is done, pattern is transfered to sample permanently; (f) AZ5206 is lift-off from the sample's surface.

If a pattern needs to be changed frequently, photolithography is not the optimal option due to the long production cycle and relevant cost. With these limitations, another fabrication technique electron-beam (e-beam) lithography is used. The process of e-beam lithography is similar to photolithography, it contains the preparation, e-beam lithography, development and dry etching, and pattern design, which is not always needed for photo-lithography as each mask is predefined. The following part starts with pattern design.

2.2.1 Pattern design

The flexibility of e-beam lithography is that you can design various patterns. Our equipment for e-beam lithography is for research applications, it is essentially a scanning electron microscope (SEM) integrated with a electron beam control module. E-beam lithography system used in commercial applications are more expensive and precise than ours. E-beam lithography can make smaller structures than photolithography, it's common to have sub-100 nm resolution, even sub-10 nm resolution. However, the electron beam also has a limitation in wavelength, and a dry etching is followed after e-beam lithography in my experiment, it's hard to make devices with structures smaller than 100 nm by this equipment. The pattern is designed by DesignCAD. Figure 2.5 shows a typical designed pattern, the left part shows the whole pattern, and the right one is a zoomed view of the center of the whole pattern.

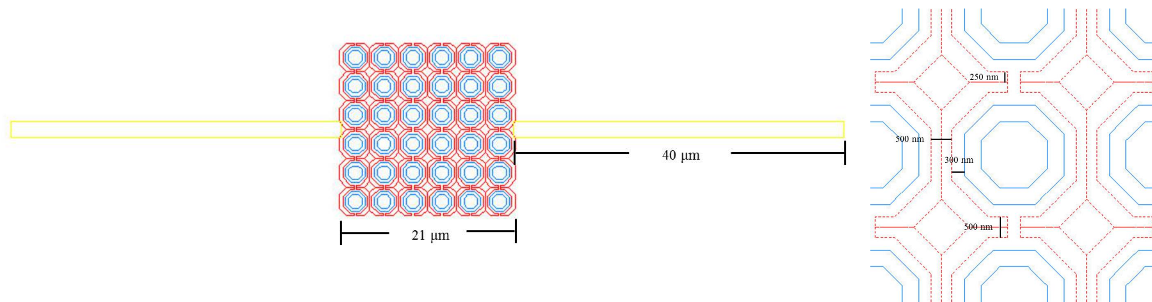

Figure 2.5: A pattern designed by DesignCAD.

The use of DesignCAD is simple, and some frequently used commands are listed below.

Commands of DesignCAD, quotation marks for clarity:

1. Input coordinates by pressing“ctrl + ;”.

2. Check one point’s coordinates: move the cursor close the the targeted point and press “,”.

3. Select an object: move the cursor close to one point and press “.”.

4. Zoom in: press “z”, then press down left key of mouse and drag out a box over the interested area.

5. Zoom in or zoom out: press “+” or “-”, then left click mouse.

6. Use a handle to move an object: select a point as a handle, sequentially press “ctrl + h” and “m”, then input the destination coordinates.

7. One special command needs to mention is that when designing a polygon shape for e-beam lithography, it’s better to use the choice from the “menu”, “edit”, “draw polygon”.

There are some other useful commands like how to draw a line, an arc, check and alter writing order of e-beam lithography, etc, please explore the “help” in menu.

Some tips in design:

1. Understand what is going to do, the designed pattern should match the corresponding photo-lithography pattern, and pay attention to alignment.

2. There is no one time success for experiment, most of the time you need to test several times, especially when the structure’s scale is around 100 nm, or the structure is large, solid and located in a sensitive area, or the material has a quantum well layer buried several hundreds nanometers beneath. One experience of mine, for a central anti-dot, if the diameter is relatively large, i.e. greater than 1 μm, design it as a ring instead of a solid filled dot to avoid too much electron exposure to the target area.

2.2.2 Preparation

This step is very similar to the preparation for photolithography, except we use different chemicals. Using the sample done with photolithography.

Preparation steps:

1. Pick up a piece of glass whose surface is covered by a thin layer of metal, glue the sample on the conducting side of the glass with colloidal graphite which is also conducting. The purpose of gluing is to make the sample easier to work with, a conducting film is required in e-beam lithography.

2. Bake the sample in a 165 °C oven for 30 min to anneal the colloidal graphite.

3. Spin PMMA or ZEP to the sample's surface, spinning PMMA at 7800 rpm for 40 s, spinning ZEP at 4000 rpm for 40 s.

4. Bake the sample in a 165 °C oven for 4-5 hour for PMMA, or 2 hours for ZEP.

The PMMA (Para-Methoxy-N-methylamphetamine) solution is PMMA dissolved in chlorobenzene, the concentration is 3%. ZEP is ZEP520A. Both of these chemicals are sensitive to a beam of electrons, and ZEP is more sensitive. This difference is reflected in the dose parameters in e-beam lithography.

When the sample is prepared through above steps, we can start with the e-beam lithography. In order to track the sample's pattern more easily, we always carefully make a scratch close to the photolithography pattern on the sample. Here, we are defining the larger structures with photolithography, and using them as guides to write smaller structures with e-beam lithography.

2.2.3 E-beam lithography and SEM

The key point of doing e-beam lithography is following instructions strictly. Figure 2.6 shows the e-beam lithography setup we use, which consists of a LEO EVO SEM and a Nano-Pattern Generating Software (NPGS). we need to have an appropriate pattern and its corresponding dose setting.

An SEM is capable to magnifying a properly loaded target to as high as 20000 times, however, the magnification we use to do e-beam lithography for most patterns is around 1000. For PMMA, the electron current is set to 12 pA, line-line distance and spot-spot distance is about 135 Å, and the dose is always around 200 $\mu C/cm^2$; For ZEP, the electron current is set to 9 pA, line-line distance and dot-dot distance is about 275 Å, and the dose is always around 60 $\mu C/cm^2$. The exact dose value depends on the structure and dimension of the pattern, which usually requires several tests with different doses.

A guide to set the dose:

Figure 2.6: E-beam lithography setup, it's an SEM integrated with an electron beam control module.

1. The exposure of electron beam is essentially a spot on the sample's surface, the e-beam moves in a way controlled by NPGS. Each spot can also effect the area around itself as the electron beam can be reflected out.

2. For different parts of the pattern, use colors in the CAD program in order to have the option to set a different dose per part.

3. For some isolated small structure whose dimension is around several hundreds nanometers, set a relatively high dose.

4. For large solid area whose dimension is above 1 μm, and it is not in a sensitive position, dose is not critical, a little high or low won't matter too much.

The development of PMMA and ZEP uses different developer and requires different developing time.

Development of PMMA:

1. Develop, IPA : MIBK (methyl-isobutyleketone) = 3 : 1, 70 s.

2. Rinse, IPA, 40 s.

Development of ZEP:

1. Develop, ZEP developer (ZDMAC or N, N-Dimethylacetamide), 40 s.

2. Rinse, IPA, 30 s. IPA acts as a developer as well, so don't rinse longer than this time.

It's a good habit to check and record at every step. After development, watch the sample

under a microscope and take pictures.

When the e-beam lithography step is not successful, such as the pattern is over exposed or the alignment of the pattern is not right or some other unexpected event happens, don't worry, failure is not unusual in such experiments. So far, the pattern fabricated by e-beam lithography is temporarily transfered to the sample surface, and it can be erased by removing the PMMA or ZEP from the sample's surface. Then, one can redo the preparation step for e-beam lithography. The following tells how to lift-off PMMA or ZEP.

How to remove PMMA is the same as how to remove photoresist AZ5206.

To remove ZEP:

1. Soak the sample in ZEP remover, several hours, at least 1 hour for my samples.

2. Follow the steps of how to remove photoresist AZ5206. This is optional.

3. Squirt IPA to the sample and use nitrogen gun to blow dry the sample.

If successful, we proceed to the next step of dry etching. A preprocess is needed to prepare the sample.

Preparation for dry etching:

1. Lift the sample off the piece of glass. Drip a little IPA on the glass piece but avoid from the sample's surface, carefully use a tweezer to push the IPA drop to the bottom of the the sample and wait several seconds, then use a tweezer to push the sample on a safe edge, usually, it's not too hard to lift the sample off the glass piece. Then spray some IPA on a clean wipe, use a tweezer to hold the sample's two edges, and gently rub the sample's bottom on the wet wipe to clean off the left colloidal graphite.

2. Get a clean 3 inch silicon wafer, put a little Apezion N grease in the center, and put the sample's bottom on the grease. Bake it in a 90 °C oven for 30 min, this process melts the grease to glue the sample on the silicon wafer flatly.

Now, the sample is ready for dry etching.

Before going to the next section, one more issue needs to be presented, namely, how to get a good SEM image. In the process of e-beam lithography, focusing the e-beam properly quickly leads to locating the target area and a successful pattern writing. Sometimes, we only need to image a sample to see whether a process problem is present, or obtain a good figure for publication. An etched sample can be used directly to do imaging, there is strong contrast between the etched part and other parts. Sometimes, a transfered e-beam lithography pattern needs to be observed before dry etching is done. In order to image such samples, a thin layer of gold with thickness about several nanometers needs to be deposited on the sample's surface by sputtering. This electrically conducting layer is helpful to get a good focus in the SEM. For e-beam lithography, the current is about 10 pA; in a pure image process, 40 pA is a good choice for this instrument (LEO EVO). In an image process,

a higher resolution and slower scanning speed setting than e-beam lithography may be used.

2.2.4 Inductively coupled plasma reactive-ion etching (ICP RIE)

Reactive-ion etching (RIE) uses chemically reactive plasma to remove material on a wafer. High-energy ions from the plasma are generated by an electromagnetic field under low pressure and bombard the wafer surface to displace unneeded part. Inductively coupled plasma (ICP) RIE is one type of RIE systems where the plasma is generated with an RF (Radio Frequency) powered magnetic field and has a very high plasma density. It tends to give more isotropic etch profiles, useful for the samples in this thesis.

The RIE recipe is different for different material, aspects of a recipe include type of chemical, RF power, chamber pressure and etching duration. In my experiments, I only used one kind of recipe for both InGaAs and GaAs, except the etching times varied based on the depth of quantum well layer in the different material. The base recipe is: pressure of 15 mTorr, ICP RF power 220 W, RIE RF power 110 W, and BCl_3 was used with flow parameter of 20 mTorr. The process time used varies from 30 s to 3 min, and I will discuss this issue for different material in later chapters.

The RIE step is similar to the wet etching step in photo-lithography. However, the etched depth is shallower, it just etches to or close to the quantum well layer, usually less than 200 nanometers. The advantage of dry etching is that it can define an edge very precisely, the precision can approach to less than 10 nm which can be validated by SEM. A typical etched edge's SEM picture is showed in Fig. 2.7, where the darker area is the etched part, and the edge is defined well. The disadvantage is that the operation is more complicated and delicate, and there is risk in burning the PMMA or ZEP that is on the sample's surface due to the high energy ion when the process time is too long. There is not a critical value to classify how much time is too long, it depends on the material.

The etching duration should be estimated roughly right before doing RIE, however it is a little hard to decide due to the limitation of material and equipment; we can only estimate it from a previous worked sample's process time and the corresponding depth of quantum well.

When doing RIE, make sure the reflected power reading for ICP RF and RIE RF is lower than 5 W. Another sign to show the plasma goes well is that the chamber is bright and not shining.

This is experiment, often many trials are needed to obtain desired results.

When RIE is done, push the sample off the silicon wafer using the back of a tweezer carefully. Use TCE to clean the grease from the bottom of the sample by soaking the sample in TCE about 1 hour, then squirt with IPA, and blow dry the sample with a nitrogen gun. Now it's ready to go to the next step, contacting.

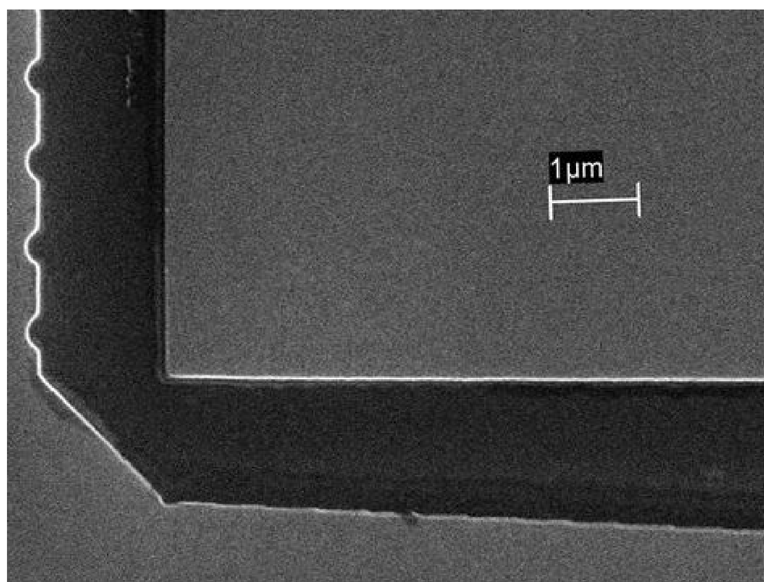

Figure 2.7: ICP RIE etched edge, the darker area is the etched part, the edge is defined well.

2.3 Contacts and wires

Eventually, we intend to make a working device not just a pattern. Contacts and wires need to connect to the current chip, and then we mount the chip on a 14-pin DIP (dual-inline package) header.

The 2D quantum well layer is buried beneath the chip's surface, so we need to make contacts conducting through the surface to the quantum well layer. We use different alloys for the n-type semiconductor and the p-type semiconductor to make those contacts pads. For n-type InGaAs, eutectic In-Sn alloy with weight ratio 52 : 48 is used, and a temperature of 210 °C is used to melt the In-Sn. After making contacts on the right position, we anneal the sample at 210 °C for 5 min in a mixed gas of 10% H and 90% N. For p-type GaAs, eutectic In-Zn alloy with weight ratio 96 : 4is used, and a temperature of 235 °C is used here. After making contacts, we anneal the sample at 450 °C for 10 min. Figure 2.8 shows the home made annealing setup used, the high pressure gas of 10% H and 90% N is not included in this figure.

When using the annealing station, to avoid oxidation, the annealing tube should be filled with gas of 10% H and 90% N during the whole process, the pressure is kept to 4 psi. When annealing is done, before taking the sample out of tube, make sure the temperature inside the tube is below 80 °C.

Instruction for doing annealing:

1. Open the tube, load sample in the center of the tube, then close it.

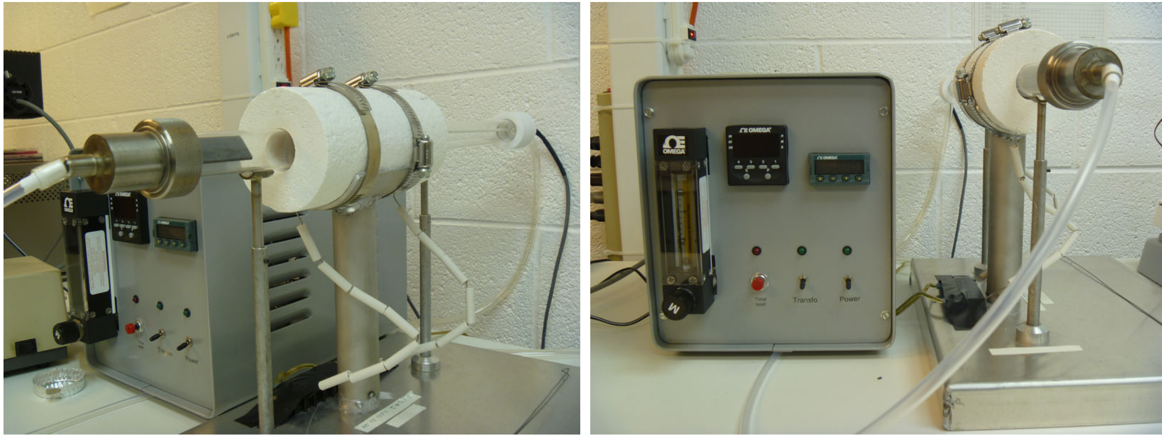

Figure 2.8: Home made annealing station.

2. Open the gas valve, adjust the pressure to 4 psi which is monitored at the front panel as shown on the right side of Fig. 2.8. This step is called flushing; keep it on for about 5 min before turning on the power for annealing.

3. Turn on the power by the button on the front panel, adjust the temperature to the target value. If the target temperature is above 400 °C, first adjust temperature to 100 °C.

4. Turn on the power of the heater, the "transfo" button in this device. If the target temperature is lower than 400 °C, when the temperature reaches the target value, keep it on for 5 min, then turn off the heater power. If the target temperature is above 400 °C, when the temperature reaches 100 °C, keep it on for about 2 min, then adjust the temperature to the target value. Keep heating until this target value is reached, keep it on for 10 min, then turn off the heater power.

5. The system will slowly cool down. When the temperature below 80 °C, close the gas valve, turn off panel power, and take out the sample.

Now, the sample is ready to be wired up. Indium sticks well to the sample at low temperature and is used as solder. Gold wire also works well at low temperature and is used to connect the sample's conducting pads to DIP header's forks. Figure 2.9 shows a DIP header with a chip wired. To solder the wire, 240 °C is used to melt indium.

The last thing before measuring is to test the contacts, which is important since after we load the sample into the measuring system, any change to the sample is not trivial. A simple serial circuit is used to accomplish this test, which is shown in Fig. 2.10.

The power source is supplied by a lock-in amplifier, and the voltage is adjusted accurately to 1 V. The typical resistance of a sample is about several hundreds or several thousands of Ohms. The voltage across the 10 kΩ resistor is measured by the same lock-in amplifier, as a 10 MΩ resistor is in the circuit, if the samples contacts work well, the voltage monitor should read very close to 1 mV (usually can approach to 0.99 mV), otherwise it means the contacts

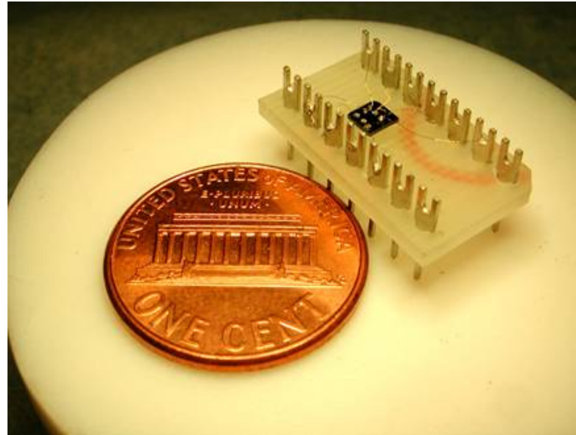

Figure 2.9: A full-fledged device and a coin, the coin is used to give an eye guide for the size of device

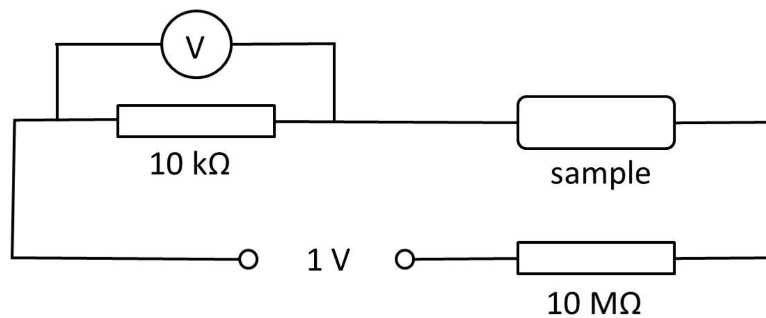

Figure 2.10: Circuit for contacts testing

pair of the sample are not good enough, and it's better to fix this problem by soldering these bad wires again.

The above described technique allows one to judge whether a contact will suitably work for most samples. In my experiments, all the n-type semiconductor samples are consistent with this method. However, there are exceptions, for example, for the p-type GaAs, the sample is very resistive at room temperature even when measured through a good pair of contacts, it's hard to make the voltage across 10 kΩ resistor close to 0.99 mV, and it turns out that the pair of contacts work well at low temperature as long as the measured voltage at room temperature is above 0.9 mV. These p-type GaAs samples have others abnormal characteristics when compared to the n-type semiconductor samples that I used, and these will be discussed in later chapters.

2.4 Depositing a thin film on sample's surface

Not all samples need this fabrication step, and this step is always after photolithography or e-beam lithography. A schematic procedure of depositing a pattern on a sample's surface is pictorially depicted in Fig. 2.11; this is essentially a negative transferring process. A pattern is first transfered to a resist layer on sample's surface (Fig. 2.11(a)), the area that is not coated by resist will be covered by deposited material finally. Then intended material is deposited onto sample's surface, and the whole sample's surface is coated by deposited material temporally (Fig. 2.11(b)). The final step is lift-off (Fig. 2.11(c)), where we use the previous standard lift-off method to remove the resist, when resist is removed, a pattern made of deposited material is transfered onto the sample's surface.

In my experiments, I used a thermal evaporator (a commercial Edwards model auto 306 evaporator) to deposit various material, the evaporator is showed in Fig. 2.12. Before evaporation, the chamber's pressure is pumped down to 7-8 $\times 10^{-7}$ Torr with assistance of a liquid N_2 trap. It can evaporate Gold (Au), Chromium (Cr), CoFe ($Co_0.6Fe_0.4$), SiO, etc. The source material is loaded in a tungsten (W) boat and heated up by a large current flowing through the boat. The evaporating current is different for each material. To successfully evaporate CoFe, an aluminum (Al_2O_3) coated molybdenum (Mo) boat is used. CoFe can be deposited on sample's surface directly, with an evaporation rate of around 1 Å/s. To deposit Au, we need to preprocess the sample's surface. A Cr layer is deposited first to act as a sticking layer for Au, where the Cr is evaporated at a rate of around 1 Å/s to a thickness about 60 Å, and the Au is evaporated at a rate of 0.5-2 Å/s. The thickness of evaporated film is monitored by a quartz crystal microbalance.

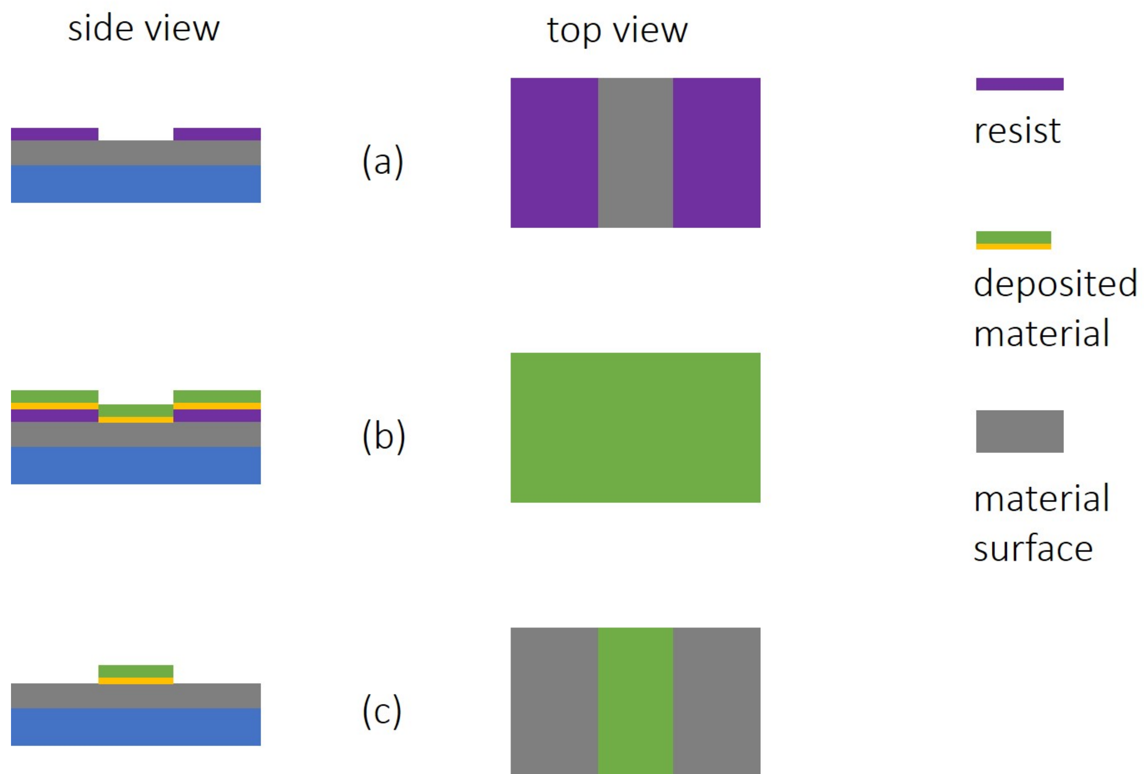

Figure 2.11: Schematic procedure of depositing a pattern on sample's surface, sequentially from (a) to (c). (a) define a pattern on resist by photolithography or e-beam lithography, (b) deposit intended material onto sample's surface, (c) lift-off resist, and pattern is transfered to sample's surface.

Figure 2.12: A thermal evaporator.

Chapter 3

Measurement setup

3.1 Overview

The main measurement system is a ^{3}He sample-in-liquid system shown in Fig. 3.1. The temperature of this system can approach to 0.35 K when using ^{4}He and ^{3}He that is recycled. When only ^{4}He is used, the temperature can approach to 1.2 K.

A schematic graph of the cryogenic equipment is shown in Fig. 3.2. During measurement, the sample is immersed in liquid ^{3}He or ^{4}He gas. As we study the magnetotransport property of a sample, a superconducting magnet is built in this system, which is immersed in liquid ^{4}He and uses ^{4}He to maintain its superconducting state. The central tube is removable, and houses a probe itself also removable, that carries the sample. Vacuum is used to isolate this system from the outside environment to prevent heat transport.

We have several probes for different purposes, each probe has a 14 dual-inline socket on its one end, and accepts a dual-inline pin header loaded with the sample. One probe is used for combining with the ^{3}He system, it can be used individually as well. Another probe has a tilting mechanism which can tilt the 14 dual-inline socket 0 to 90 degrees from its original position, such that the angle between applied magnetic field and sample's surface is adjustable, so that not only perpendicular magnetic field but also in-plane magnetic field can be achieved. However, this probe cannot be connected with the ^{3}He system, and thus the lowest temperature it can reach is 1.2 K.

We have two power supplies for the superconducting magnet, one is a bipolar superconducting magnet power supply Model CS-4, it can generate magnetic field from -9 T to 9 T. However the sweeping step cannot be controlled precisely, and it is useful for high B measurement. When magnetotransport measurement is sensitive to the change in magnetic field, another power system is used which is a Keithley 2400 SourceMeter, combined with a Kepco bipolar power supply. Its changing step can be controlled well, and with a proper setting

Figure 3.1: Measurement system. In the left photograph, the Janis dewar and associated electronic instruments to supply power and magnetic field, measure the sample and monitor the system are shown. The right photograph shows the ^{3}He system (home built).

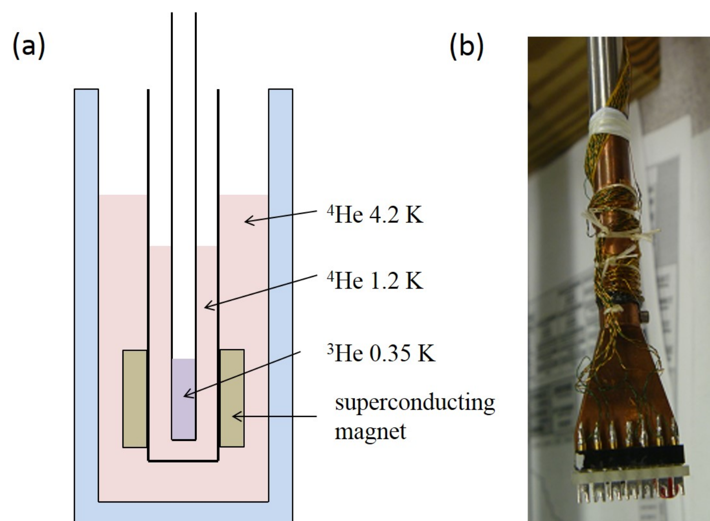

Figure 3.2: (a) Schematic graph of the intersection view of the cryogenic system. (b) The inner probe with a sample mounted on its tip. In experiments, it is inserted into the central tube of the setup shown in (a).

the finest step can be smaller than 0.5 G. With this setup, the magnetic field may vary from -2.3 T t0 2.3 T. Depending on the purpose of each experiment, different power supply and setting are selected. The following will discuss various situations and their corresponding setup.

3.2 Cooldown

Our measurement system is inside a dewar. Cooldown of the system is a gradual change of temperature from room temperature to 1.2 K or 0.4 K. Roughly, it can be separated into two steps. First cool down the system with liquid nitrogen to approximate 80 K, then take nitrogen out and cool the system by liquid helium. The liquid nitrogen cooldown process takes at least 24 hours, and sometimes longer. When the liquid nitrogen in the dewar is consumed too much, a refilling is probably needed. Before filling the dewar with liquid helium, the nitrogen has to be taken out completely otherwise freezing at some inner valves may happen. Removing the liquid nitrogen out of the dewar requires a clear logic and experience to tell whether the last drop of liquid nitrogen is out. Pure He gas is used to chase the nitrogen out of the dewar at the last step. When nitrogen is out, the temperature inside the dewar remains low and He gas is left in the dewar, and liquid helium has to be filled in immediately with special tools and practiced skills. With liquid helium in the dewar, the temperature of this cryogenic system will keep dropping. The eventual purpose of this low temperature system is to cool down the sample and offer a low temperature environment for the measurement. We usually fill about 30 inches liquid helium in the dewar for this cryogenic system, then put the probe with sample mounted on its one end in this cryogenic system and make all the necessary electronic connections.

The sample's temperature starts to drop from room temperature, and a typical cooldown process result is shown in Fig. 3.3. The resistance of the sample shows a typical metallic behavior. At the beginning, the resistance drops with temperature decreasing, which is caused by phonon freezing. When the temperature is lower than 50 K, the slight resistance increase is caused by carrier freezing. The current through the sample is 100 nA in this stage. The lowest temperature in this graph is about 1.2 K.

For measurements at 1.2 K, the ^{3}He system is not needed. For measurements at 0.4 K, the ^{3}He system has to be connected to the probe before the sample's temperature drops too much. The mechanical connection between any joints should be sealed well to avoid gas leakage. So one has to make sure to use the right O-ring, and verify that the tubes or chambers are under the proper vacuum, and perform every operation in a logical order. For measurements at 0.4 K, the ^{3}He is condensed to the central tube of Fig. 3.2 from its reservoir before the temperature of the system drops to 1.2 K. Then with help of a diffusion pump and a mechanical pump, the condensed ^{3}He evaporates to its original reservoir. The evaporation process cools the system to 0.4 K, and this is the last cooldown step from 1.2 K to 0.4 K.

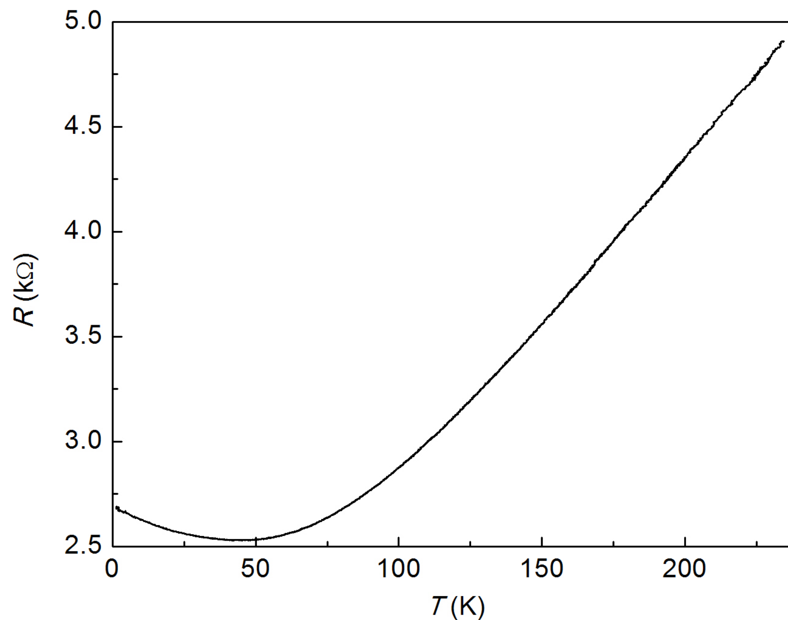

Figure 3.3: A typical cooldown trial of an n-type heterostructure device, resistance versus temperature.

The essential step to use ^{3}He system is the condensation. Condensation is a gradual process. Usually the first condensation along with the sample's cooldown process takes about 12 hours. When more measurements are needed, recondensation is required, which usually takes about 3 to 4 hours as the temperature of the cryogenic system is low enough (below 20 K) to make the process go faster.

The cooldown process from 1.2 K to 0.4 K requires experience; several valves and pumps need to function in precise order. Once the system achieves 0.4 K, it can last for more than 24 hours with appropriate fine adjustments, and most of the measurements are done during this time duration. The applied current, voltage, magnetic field, connection configuration can be changed in experiments. Sometimes, we need to do temperature dependent experiments, which are always at the last stage of a measurement cycle. The system is heated up by a resistor with a temperature monitor, where we always go from low, 0.4 K, to higher temperature as it's easier to control the temperature by heating rather than cooling. As the temperature goes up, the condensed ^{3}He is lost from the central tube to its original reservoir when the temperature is above 1.2 K. Almost all of the ^{3}He goes back to its original reservoir, and only a little thermal convection gas is left in the central tube. If further measurement is needed on the same sample, a recondensation and a cooldown from 1.2 K to 0.4 K follow. Although the behavior of a sample won't change among different cooldowns, the fingerprint of a sample varies. Thus we always try to get all the data which will be potentially used in a comparison during a single cooldown.

3.3 Techniques of measurements

3.3.1 Instruments and programs

The instruments that we use to supply power and monitor signals are voltage/current sources and lock-in amplifiers. All the instruments are connected into a network with a master program to control and monitor all their functions, the protocol is TCP (transmission control protocol), the program communicates with instruments, and instruments are connected to each other via a general purpose interface bus (GPIB). The logic of managing the control program follows the data flow, and the tool we used is LabView. Basic programming skills and I/O knowledge are helpful to understand the entire setup and measurement process.

The master control program and instruments network are already built, and only some necessary maintenance are needed for my experiments. The main task during a measurement is to find the optimal setting parameters for each instrument.

During measurements, the current through a sample affects its environment. So for a general measurement, the current I is always below 50 nA, with 20 nA as a typical value. In exceptional cases, e.g. when current dependence experiments are performed or an intended interruption is needed, current values above 50 nA, typically up to 300 nA will be supplied. When the current is too high, the thermal energy generated by the sample will heat up the environment, and the temperature then can't keep to 0.4 K. Also, too high a current may introduce more noise, or heat the carriers.

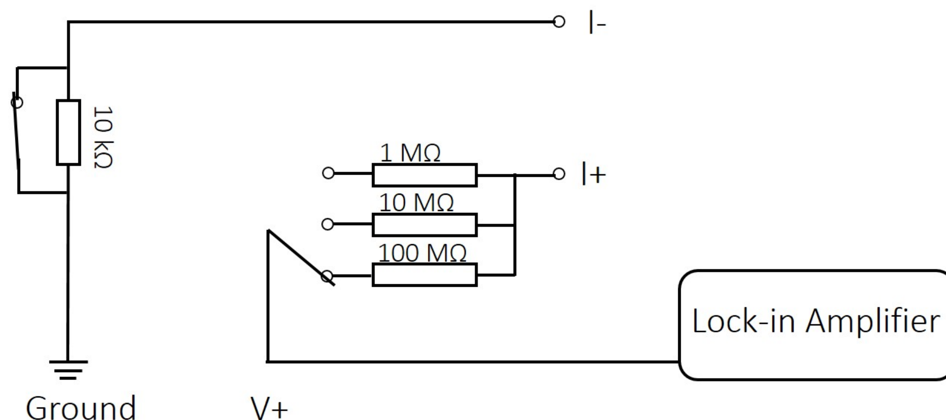

Figure 3.4: Constant current source, consisting of a low noise lock-in amplifier and a set of high resistance resistors. Switch is used to select a different resistor (1 MΩ, 10 MΩ or 100 MΩ) to obtain a different current. The 10 kΩ resistor and its shorting switch are used to test the current value when necessary.

We use a constant current source to power a sample, as shown in Fig. 3.4. This constant

current source is composed of a low noise lock-in amplifier and a resistor with sufficient large resistance R. A constant current of 20 nA may be obtained by 2 V given by the lock-in amplifier and a 100 MΩ series resistor. The noise at the input introduced by this setup to the sample is pretty low. The noise of the lock-in amplifier is characterized by the manufacture[23] as

$$V_N = \sqrt{4k_B T R_{lock-in}} \quad \mathrm{V}/\sqrt{\mathrm{Hz}} \tag{3.1}$$

with $R_{lock-in} \approx 1000\ \Omega$ and assuming $T = 300$ K. The current noise introduced by the large resistor R to the constant current is about

$$I_N = \sqrt{\frac{4k_B T}{R}} \quad \mathrm{A}/\sqrt{\mathrm{Hz}} \tag{3.2}$$

The noise is denoted by its RMS (root mean square) value. In our setup, we usually used two different lock-in amplifiers to supply the voltage, PAR124 (Princeton Applied Research Model 124A lock-in amplifier) and SR830 (Stanford Research System Model 830 lock-in amplifier). The SR830 is used in raw measurements, such as early phase cooldown and contacts test, while the PAR124 is used for delicate measurements. In this constant current source, when the PAR124 and $R = 100$ MΩ resistor are used, the voltage noise introduced by this constant current source for a sample with resistance of $R_S = 2500\ \Omega$ is about the sum of the noise given by the large resistor N_R and the noise given by PAR124 $N_{lock-in}$. Here, $N_R \approx I_N \times R_S = 3.2 \times 10^{-11}$ V/$\sqrt{\mathrm{Hz}}$ and $N_{lock-in} = 4 \times 10^{-9}$ V/$\sqrt{\mathrm{Hz}}$ given by the manufactures. My samples' signal is always in a microvolt level, thus this constant current source has pretty high quality for my samples.

My research includes studying the magnetotransport of heterostructure devices at low temperature. In different magnetic field regimes, the sensitivity of the measurement system is different and the setting parameters are tuned separately. We separate the magnetic field into three regimes along with three independent programs; large field -9 T $\sim$ 9 T, medium field -2.3 T $\sim$ 2.3 T and small field -2300 G to 2300 G.

The large field program has a fixed data collected rate about 180 points per minute, the magnetic field step varies by the sweeping rate. The sweeping rate can be tuned. For a very fast sweep, a value of 2.17 min/T can be used, but this is rarely used as the magnetic field step is about 77 G/s which is too large and thus we may miss meaningful information about the sample. Usually, for the first rough sweep, I always chose 3.08 min/T, later on, for a careful large scale sweeping, 3.49 min/T or 4.72 min/T is used, with hardly any difference. For a small range on the large magnetic field regime, 6.17 min/T or 10.02 min/T is used; this corresponds to a magnetic field step about 17-27 G/s which is still too large for a careful magnetotransport measurement such as mine. The accuracy of the power supply, CS-4, can't reach a finer step practically via this program. Theoretically, any rate between the fastest and the slowest value can be used in this system, the principle of setting the rate is to keep dB/dt low enough to ensure the induced voltage of the superconducting magnet is less than 3 V which is the maximum limit it can bear.

The medium field program is used most often, its magnetic field can go up to 2.3 T which is large enough to reach the quantum Hall effect regime or the Shubnikovde Haas effect regime for my devices, and it also has the ability to push the magnetic field step to below 1 gauss which is small enough to resolve almost all the quantum interference effect my experiments look for. A more accurate power supply, Keithley 2400 SourceMeter is used here in combination with a voltage-controlled Kepco bipolar power supply, and a stable and well controlled magnetic field can be generated through this combination. The voltage source function is selected which has different resolution for different ranges. If measurements need to have a magnetic field above 0.46 T, we set the voltage range value to 20 V, and within this range the voltage resolution is 0.0005 V which corresponds to a magnetic field step of about 1.15 G. In a sensitive measurement, this range is not a good choice practically to give a good result, that means when the magnetic field goes above 0.46 T, the magnetic field resolution is always greater than 1.15 G. When the intended magnetic field is below 0.46 T, it's best to select the 2 V voltage range, as in this range the voltage resolution is ten times less and reaches 0.00005 V. However, most of the time, we don't need to go to this limit. So a voltage step between 0.0003 V and 0.0005 V is more likely to be used which gives a magnetic field resolution about 0.6 G to 1.2 G. The concrete values above are specific to our system, for a different experimental setup, these values may vary, however, the idea of getting a good measurement result is similar.

Generally, there is a trade-off between the resolution of the magnetic field and the time consumed during one measurement. When the resolution is too high and the sweeping magnetic field range is relatively large, for example, the resolution of magnetic field is about 1 gauss, the range is about 0.5 T and the duration between two datapoints is 1 s (this duration depends on the time consumed by instruments for taking one datapoint), then one sweep takes more than 1 hour to complete. When the sweep time is too long, the temperature may vary and overall you have less trials per cooldown. On the other hand, if the resolution is too low, although you can make many more measurements per cooldown, you may lose some important details of the signals. Therefore, it's better to estimate how much time one trial will take and what the resolution of a particular setting is before really running a trial. The estimation can also give you a hint about what to do in the next step and help you to discover problems and improve setting instruments parameters.

The small field program is not used too much in my experiments. It uses the Keithley 2400 SourceMeter as the current supply, where the difference from the medium field program is that it uses the current source function of the Keithley 2400; it has the same resolution ability as the medium field program with field below 0.46 T.

Our measurements are in the low frequency regime, and we use lock-in amplifiers to pick up signals. In my experiments, three kinds of lock-in amplifier are used, PAR124, SR830 and EGG7265 (EG&G 7265 DSP Lock-in Amplifier). PAR124 is an analog lock-in amplifier, a Keithley 2000 Multimeter is used to convert the signal picked up by PAR124 to a digital signal before signals are recorded by the program. To use lock-in amplifiers, a good frequency is important for avoiding noise, the frequencies we used are 46.0 Hz and 37.6 Hz.

A 370AC (LakeShore 370 AC Resistance Bridge) monitors the system's temperature, and it also controls the system's temperature in a temperature dependence measurement. A GS200 (YOKOGAWA DS 200 DC Voltage/Current Source) is used to supply gate voltages.

3.3.2 Improving performance of a sample

A sample's performance is important in a measurement. Sometimes, no useful results are not, or at least not all, caused by defects in a sample; some tricks and experiences can improve a sample's performance in some cases.

During the process of making a sample, try to do every fabrication step as well as possible. During the preparation of a measurement, try to make every connection logically, avoid any potentially risky operation. Experiment is different from theory, there is a large probability to encounter unexpected phenomena. Examples include contacts which even when verified prior to a cooldown do not work at lower temperatures, a sample with a good geometry gives noisy signals, etc. The following discusses some of my experiences.

When designing a pattern, try to align the pattern in a way that more than one configuration of contacts can be made to accomplish the measurements, and try to avoid correlations between different parts of sample such as even if one part of the sample does not work it won't influence other parts of the sample. When making contacts, try to use every possible contacting pad even if it is a duplicate, it may become the only working contact later on. Before a real measurement, test the performance of all contacts via the method described in chapter 2, and if possible test at both room temperature and liquid nitrogen temperature. After loading the sample into the cryogenic system, double check the contacts' performance. If some contact does not work, try to organize the working contacts in different ways, or transfer one contact into two by a splitter when necessary. We prefer to use a four-point measurement configuration, but a three-point measurement is used when one does not four working contacts. If all these methods do not work, have to take the sample out and fix the bad contacts.

Test different values of the constant current flowing through the sample and select the value which gives the least noise. For the setup of each instrument, referring to a historically similar setting is a good start point when you have no idea what to do. The applied current is AC, the measured value is the RMS value of the corresponding attribute, the data is collected by a lock-in amplifier where changing the integral constant time will change the noise level. Generally, a longer constant time gives less noise, but the trade-off is some details of the signal may be lost if the time constant is inappropriately long. In my experiments, 1 s is the most often choice.

The above are normal operations to achieve a good measurement. Sometimes, exceptional operations are needed, and I describe these. Giving a high current pulse to the sample, e.g. above 300 nA. Building a front gate or a back gate to a sample, then trying to apply

a gate voltage to add or deplete electrons in the sample. Mounting an LED, which works at low temperature, close to a sample. As some materials are light sensitive. Turning on the LED for a short time (usually several seconds) results in the photon generated carriers in the sample, thus giving a better quality signal. The last method worked most effectively in my experiments. An LED can generate thermal energy and a high current through it may disturb the low temperature environment, thus current used was only 10 μA for the particular kind of LED in my experiments.

Chapter 4

Electron interference in InGaAs/InAlAs

This chapter is focused on samples made from an n-type InGaAs/InAlAs heterostructure referred to as P122, where P122 is the name given by the MBE group who grew this material at the University of Oklahoma. Two kinds of electron interferometers are made from this material, Aharonov-Bohm (AB) ring and ring array. An AB ring is essentially a Mach-Zehnder (MZ) interferometer [24, 25, 26, 27], while ring array performs like a combination of Mach-Zehnder interferometer and Sagnac-type interferometer. A Fabry-Perot-type interferometer [28] is another typical electron interferometer used in mesoscopic physics. This chapter describes aim of this work, material, sample pattern design, devices, data analysis and conclusions.

4.1 Introduction

Various successful mesoscopic electronic interferometers are reported in publications [24, 25, 26, 27, 28, 29, 30, 31, 32, 33]. Before 1980's, interferometers for electron interference were made of metals and superconductors, which were mostly used to verify the existence Aharonov-Bohm (AB) oscillations. Nowadays, electron interferometers are often made of semiconductor. The focus of this study is extended to investigate the factors related with quantum phase decoherence.

The electron interferometers used in this chapter are made of the P122 n-type InGaAs/InAlAs heterostructure, composed of one single ring or an array of rings. As stated in chapter 3, the magnetic field B resolution is about 1 G, which means in order to practically get a good measurement result of AB oscillation, the expected periodicity of the designed AB ring should be greater than 10 G. The larger the periodicity the more accurate and clean the interference signals will be, however, a larger periodicity requires a smaller dimension of the

designed AB ring. As stated in chapter 2, given the uncertain depletion layers it is hard to make structures less than 100 nm, thus we decided to design the ring structure with an AB periodicity between 10 G and 40 G. The details of design of those electron interferometers are discussed in section 4.2.

Mesoscopic system are large compared to atomic scales, but are still of a length scale preserving quantum phenomena. The structures we designed in this chapter are sub-micron, which have a comparable length scale of the phase coherence length l_ϕ at low temperatures (T) of the respective material, and we can take their systems as mesoscopic systems. Thus the study of quantum phase decoherence in our devices can give insight of fundamental properties of mesoscopic systems. Electron quantum interference is an important method to explore mesoscopic physics and quantum decoherence. The AB effect is a remarkable manifestation of quantum interference and has proven experimentally accessible if devices are prepared properly. Weak-localization is another valuable phenomenon to use which will be discussed in chapter 5.

4.2 P122 n-type InGaAs/InAlAs, sample pattern design and devices

This n-type Si-δ doped InGaAs/InAlAs heterostructure is grown by molecular beam epitaxy (MBE) technique. It has an InP (001) substrate. The quantum well is a 10 nm layer of $In_{0.64}Ga_{0.36}As$ between two layers of $In_{0.45}Al_{0.55}As$. In order to have sufficient electrons in the quantum well, Si-δ doping is used. The schematic structure of this heterostructure is depicted in Fig. 4.1. Its quantum well is relatively shallow compared to the materials used in chapter 5, the quantum well layer buried 50 nm underneath the surface.

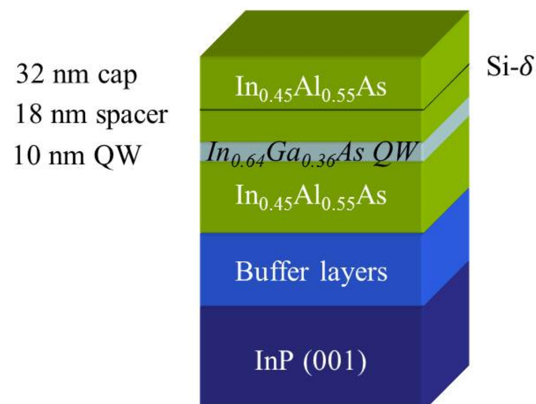

Figure 4.1: Schematic structure of P122 n-type InGaAs/InAlAs.

Generally, the fabrication process remains similar for different materials, only some aspects need to be adjusted. The depth of quantum well layer affects the ICP-RIE duration and

annealing duration, in ICP-RIE the etched depth needs to reach or close to the quantum well layer, and in annealing the metal eutectic needs to diffuse to the quantum well layer. n-type heterostructure and p-type heterostructure have different annealing temperature, and different metal eutectic is used. Using the parameters stated in chapter 2, for this material, the ICP-RIE duration is 40 s, the annealing temperature is 210 °C and duration is 5 min.

Figure 4.2: The designed pattern is used for a device named “R082410”.

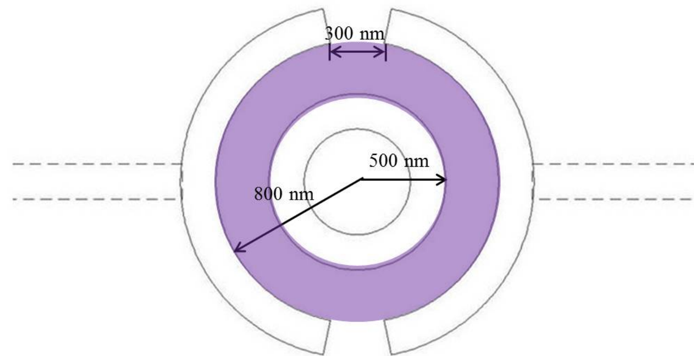

Figure 4.3: The design pattern of the single AB ring, this is the central and essential part of the real pattern, the omitted outer part can be varied according to different photolithography pattern. The central light purple shadowed ring is design as electron conducting channel with width 300 nm, which is the AB ring effectively. This design is used for a device named “R082410”.

Figure 4.2 shows the design pattern for the device named “R082410”. Figure 4.3 shows the designed single AB ring which is the essential central part of the device “R082410”, the detailed dimension information is depicted in figure itself. The parts beyond the center need to match the photolithography pattern which is preprocessed on the same device, whose function is to block electrons and force electrons to only flow through the designed electron conducting channel, the shadowed ring in Fig. 4.3. This device is used to study AB oscillation and Berry’s phase.

Figure 4.4 shows the designed pattern of a 5×5 ring array, which is for a device named “InGaAsL CoFe2b”. The neck between each rings has a width of 300 nm and length of 200 nm, the width of each row is 2.2 μm, the width of each column is also 2.2 μm. In order to derive a reasonable comparison between device “R082410” and device “InGaAsL CoFe2b”, each ring’s dimension in Fig. 4.4 is the same as the ring’s in Fig. 4.3. The size of other parts is designed more flexibly. They don’t affect the experimental result too much, except that

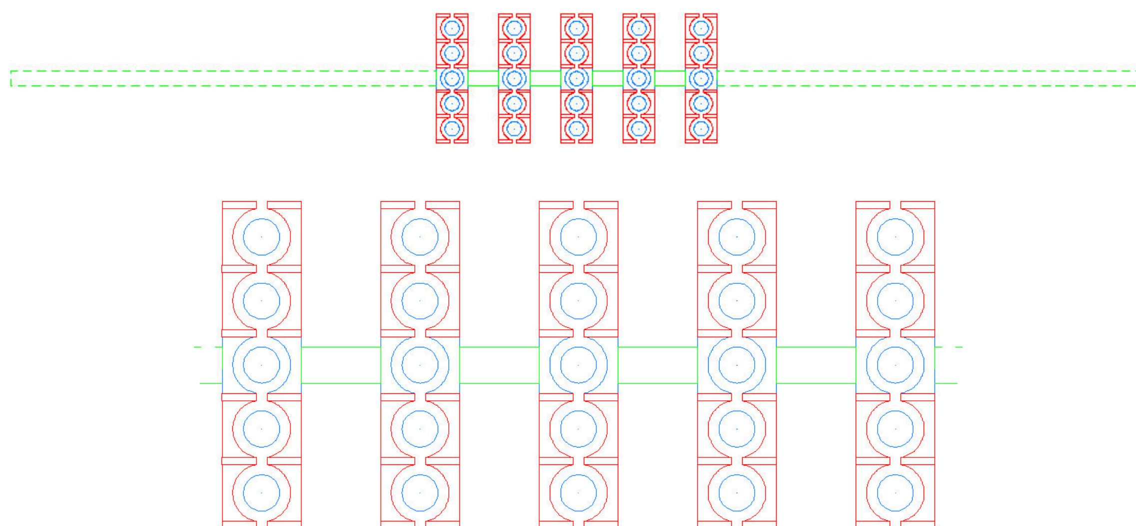

Figure 4.4: The designed pattern of a 5×5 array of AB rings, This design is for the device "InGaAsL CoFe2b". The upper part shows the whole view, the lower part emphasizes the ring array. For each ring, the dimensions are the same dimension as Fig. 4.3, other size information is detailed in text.

they need to fit in the photolithography properly. This device is used to study AB oscillation, Altshuler-Aronov-Spivak (AAS) oscillation and time-reversal symmetry breaking.

Figure 4.5 shows the design of a device named "R20110929a", Fig. 4.6 giving a zoomed view of the ring array part. The rings are separated into two groups which can work independently, each group is a 25×12 ring array, one group will be covered by ferromagnetic CoFe in the real device. There are some designed defects (short path) in the array, which are used to avoid conducting failure. This device is designed to study the effect of magnetic field in time-reversal symmetry breaking initially, however, the resistance of this device is too high which may be caused by the dense e-beam lithography. Although we were aware of this potential problem and designed some short paths, it turned out such a dense design is a challenge for our fabrication.

Figure 4.7 is an SEM image of a single ring pattern, this is taken from a test sample which has a slightly different size compared to Fig. 4.3. This picture was taken before ICP RIE, a thin layer of gold is sputtered on the sample's surface after e-beam lithography development. This gold layer improves the contrast of the image when performing SEM image. Figure 4.8 is an SEM image obtained on a test sample with the same design as Fig. 4.4.

Figure 4.9 is an SEM image of device "InGaAsL CoFe2b". Since this device didn't work, it was disassembled and studied using SEM. In Fig. 4.9, we can see that the necks between rings almost disappeared, this explains why device "InGaAsL CoFe2b" was so resistive.

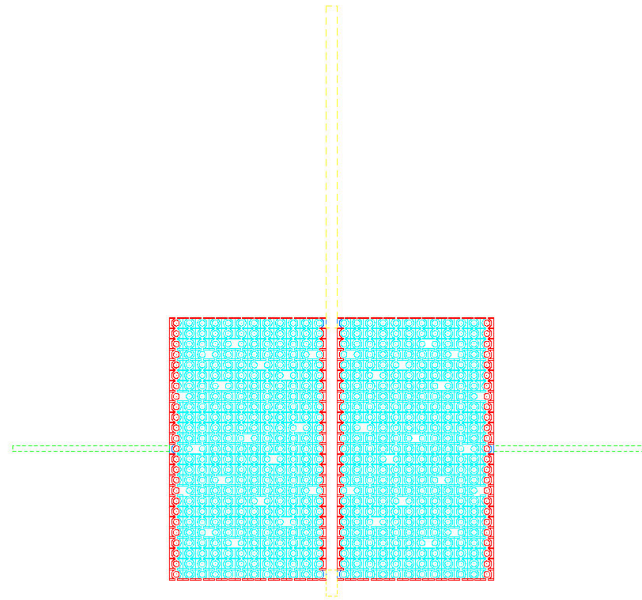

Figure 4.5: The designed pattern for a device named “R20110929a”. Each ring has the same dimension as in Fig. 4.3. The yellow middle bar separates the ring array into two groups. Combining with the photo-lithography pattern, these two groups can work independently.

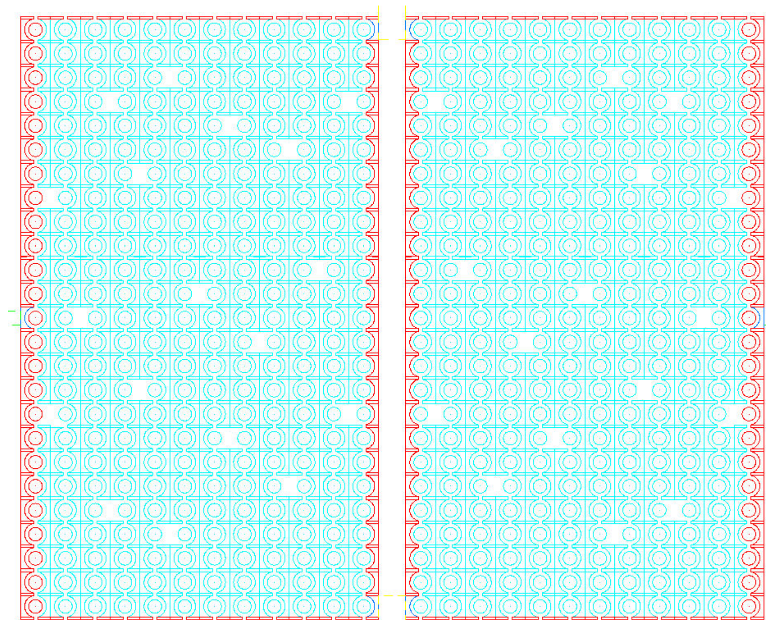

Figure 4.6: The design of the array part of the device “R20110929a”. Each ring has the same dimension as in Fig. 4.3. The left and right ring arrays can perform independently. In the real device, the left ring array is covered by ferromagnetic CoFe.

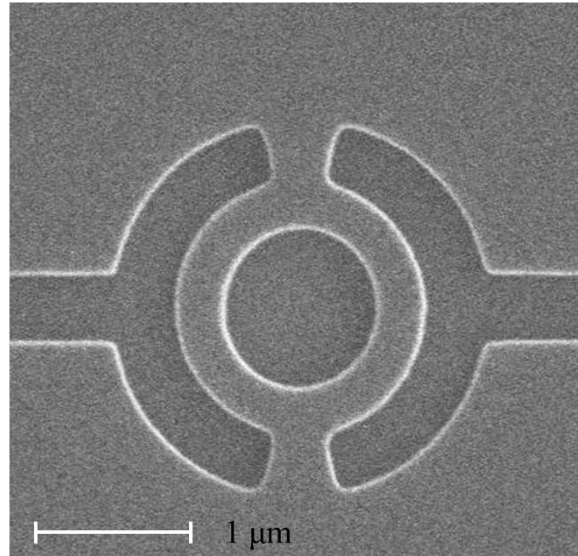

Figure 4.7: The SEM image of an AB ring with dimension slightly different from Fig. 4.7. This image was obtained from a sample after e-beam lithography but without dry etching. A gold layer is sputtered on the PMMA pattern.

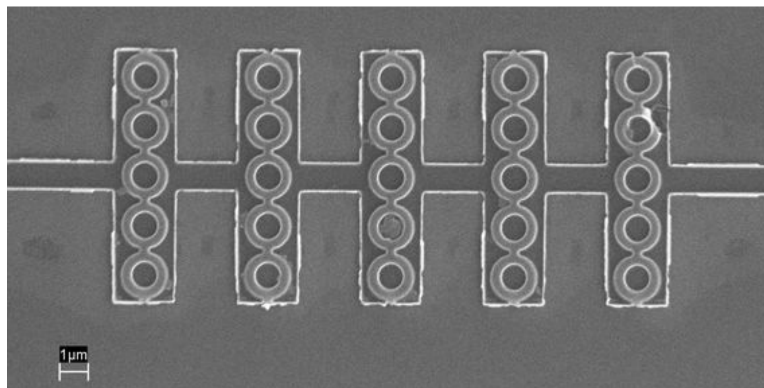

Figure 4.8: The SEM image of an AB ring array, its dimension is the same as Figure 4.4. This image was taken from a sample after dry etching.

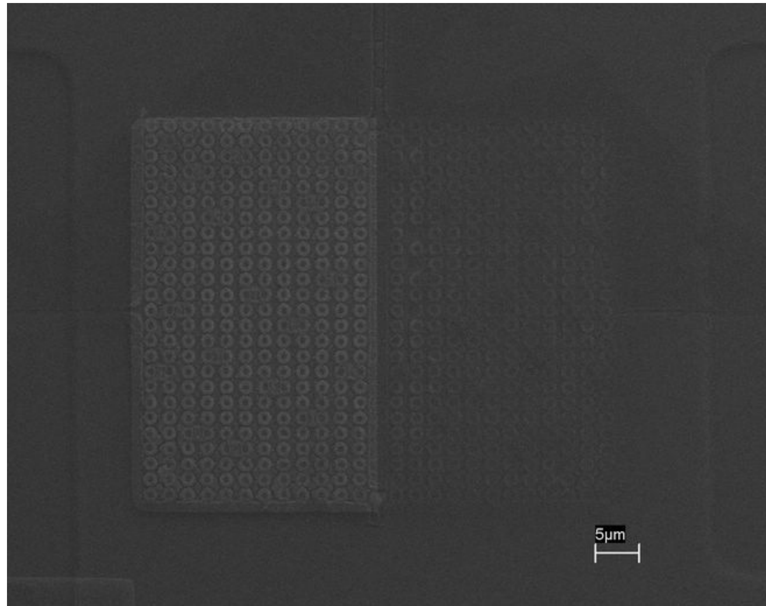

Figure 4.9: The SEM image of AB ring arrays, its dimension is the same as Figure 4.5 and 4.6. This image was taken from a sample after dry etching and with the left part covered by CoFe which is deposited by thermal physical vapor deposition.

The dim half part of Fig. 4.9 is covered by CoFe. The technique used to deposit CoFe on the surface is stated in chapter 2. After ICP RIE, the ZEP is lifted off completely and then the sample is prepared for e-beam lithography. A simple rectangle pattern was designed with size $55 \times 26.4\ \mu\text{m}^2$. When doing e-beam lithography, we align this rectangle to the part that will be deposited with CoFe. A good alignment requires skill and carefulness. After ZEP development, we use the technique stated in chapter 2 to deposit CoFe.

4.3 Overview of experiment

Figure 4.10, 4.11 and 4.12 show the schematic structure of the 3 devices "R082410", "InGaAsL CoFe2b" and "R20110929a", contacts labeled with numbers, and patterns indicated.

The measurement for these three devices are similar, however, depending on the layout of device's pattern and quality of contacts, the configuration varies. We will use the labeled contacts in Fig. 4.10, 4.11 and 4.12 to depict how each measurement is implemented. Generally, a constant AC current is supplied to a device, and the voltage signal across a specific pattern is collected when varying magnetic field which is perpendicular to the 2D pattern's surface.

To get the general properties of a heterostructure at low temperature, a spare Hall bar is needed, where a Hall bar is a rectangle structure, contacts 4, 5 and 7 form a Hall bar in

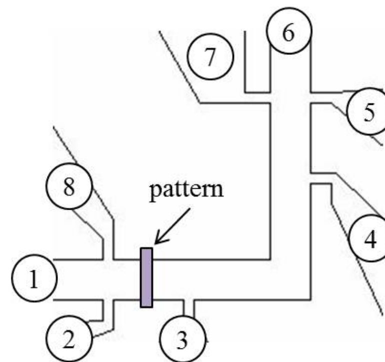

Figure 4.10: Schematic view of device "R082410". The pattern on the Hall bar is the same as Fig. 4.2 rotated by 90 °, the "L" shaped Hall bar was fabricated by photolithography. The distance between leg 2 and leg 3 is 160 μm, and the width of the Hall bar is 80 μm.

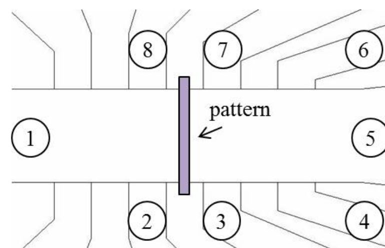

Figure 4.11: Schematic view of device "InGaAsL CoFe2b". The pattern is the same as the upper part of Fig. 4.4 rotated by 90 °, and Hall bar was fabricated by photolithography. The distance between leg 2 and leg 3 is 40 μm, and the width of the Hall bar is 50 μm.

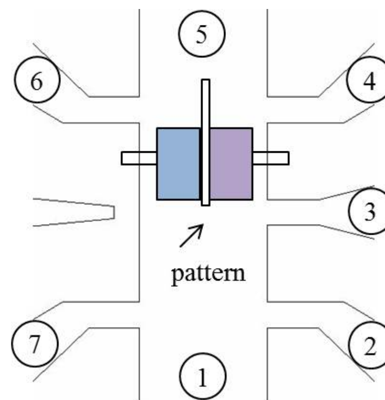

Figure 4.12: Schematic view of device "R20110929a". The pattern is the same as Fig. 4.5, and Hall bar was fabricated by photolithography. The distance between leg 2 and leg 3 is 40 μm, and the width of the Hall bar is 50 μm.

Figure 4.10, contacts 3, 4, 6 and 7 form a Hall bar in Figure 4.11, contacts 2, 3 and 7 form a Hall bar in Figure 4.12. As stated in the previous section, this heterostructure contains a 2D electron system (2DES) in a 10 nm wide $In_{0.64}Ga_{0.36}As$ quantum well located 50 nm underneath the surface, the aim is to obtain the 2DES density, mobility and resistivity.

Figure 4.13 shows the measurement configuration of Hall bar. A constant current I is supplied through contacts 1 and 6, a sweeping magnetic field B which is perpendicular to the Hall bar surface is also supplied, the Hall voltage signal $V_H(B)$ is collected through contacts 5 and 7, the magnetoresistance signal $V_{MR}(B)$ is collected through contacts 4 and 5.

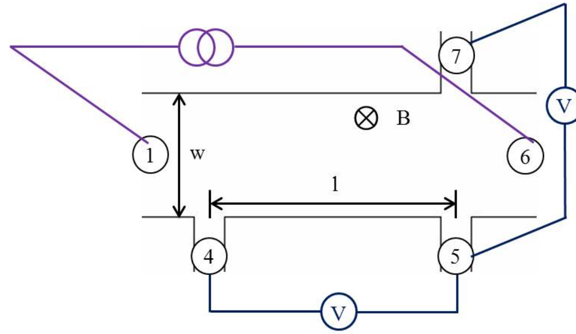

Figure 4.13: Measurement configuration of a Hall bar.

Resistance of Hall bar is $R = V_{MR}(0)/I$. The Hall coefficient of this 2D Hall bar is $R_H = V_H(B)/(IB) = -1/(ne)$, where n is the 2DES density, e is the electron charge, thus the 2DES density is $n = -1/(R_H e)$. In two-dimension, resistance can be expressed as $R = \rho l/w$, thus the resistivity of a Hall bar is $\rho = Rw/l$. Mobility can be obtained by $\mu = 1/(\rho ne)$. Taking the device "R082410" depicted in Figure 4.10 as an example, $l = 160$ μm, $w = 80$ μm.

At 0.4 K, for this heterostructure, the 2DES density $n = 9.4 \times 10^{11}$ cm^{-2}, 2DES resistivity $\rho = 110$ $\Omega/\square$, mobility $\mu = 5.9 \times 10^4$ cm^{-2}/(Vs).

4.4 Single AB ring

4.4.1 A general view of AB oscillations of a single AB ring

Figure 4.14 depicts the measurement configuration of the single AB ring. A constant low frequency AC current is supplied through contacts 1 and 6, AB ring's voltage signal is collected through contacts 2 and 3, magnetic field is perpendicular to the device's surface, whose direction can be either into or out of the surface. The supplied current is usually 20 nA except when studying current dependence. Magnetic field varies between -2.3 T to 2.3

T, and can reach up to 9 T is necessary.

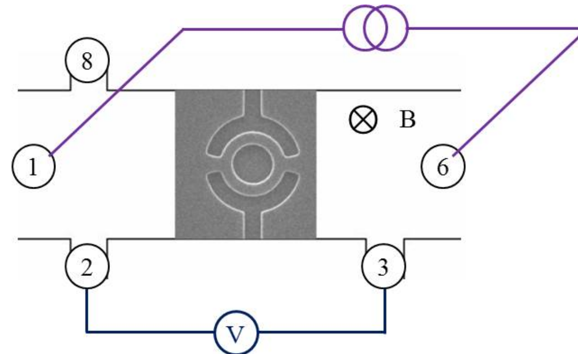

Figure 4.14: Schematic view of the 4-terminal measurement configuration of a single AB ring. A perpendicular magnetic field is applied.

The AB effect occurs in a setup as in Fig. 4.15. The dark blue lines depict the trajectory of the electrons. A perpendicular magnetic field threads through the center area represented by a circle with radius r. Ideally, there is no magnetic field going through the electron trajectory area, experimentally, a magnetic field exists in the electron path.

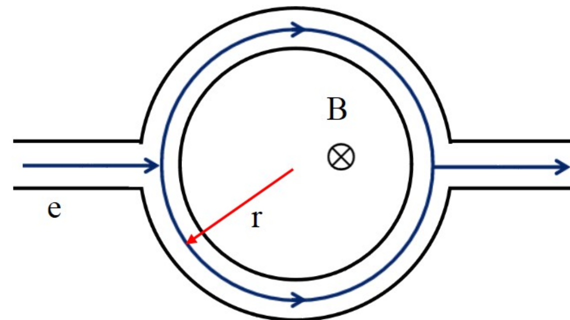

Figure 4.15: A schematic electron interferometer which can perform AB effect.

The Hamiltonian of an electron in a setup like Fig. 4.15 can be expressed as $H = 1/(2m)(-i\hbar\nabla + e\mathbf{A})^2$, the phase difference between of the upper and lower electron orbits is $\Delta\phi = e\Phi/\hbar$. Assuming a uniform magnetic field threads through a circle area with radius r, the flux can be expressed as $\Phi = B\pi r^2$. Therefore, for a given AB ring, the expected magnetic field period of AB oscillation is $B = (h/e)/(\pi r^2)$.

At 0.4 K, oscillations were observed over a wide range of B up to 0.6 T, consistent with the AB oscillations of the device. In the following content, AB oscillations are used to refer such oscillations. Figure 4.9 shows the measured results in a range of -0.3 T to 0.3 T. It also displays a quasi-periodic modulation with B. Figure 4.9(c) provides data from -0.3 T to 0.3 T, the modulation is apparent. A higher resolution view is given in Fig. 4.9(a) and (b). The next section will focus on the AB oscillations on a lower range of B, below 600 G.

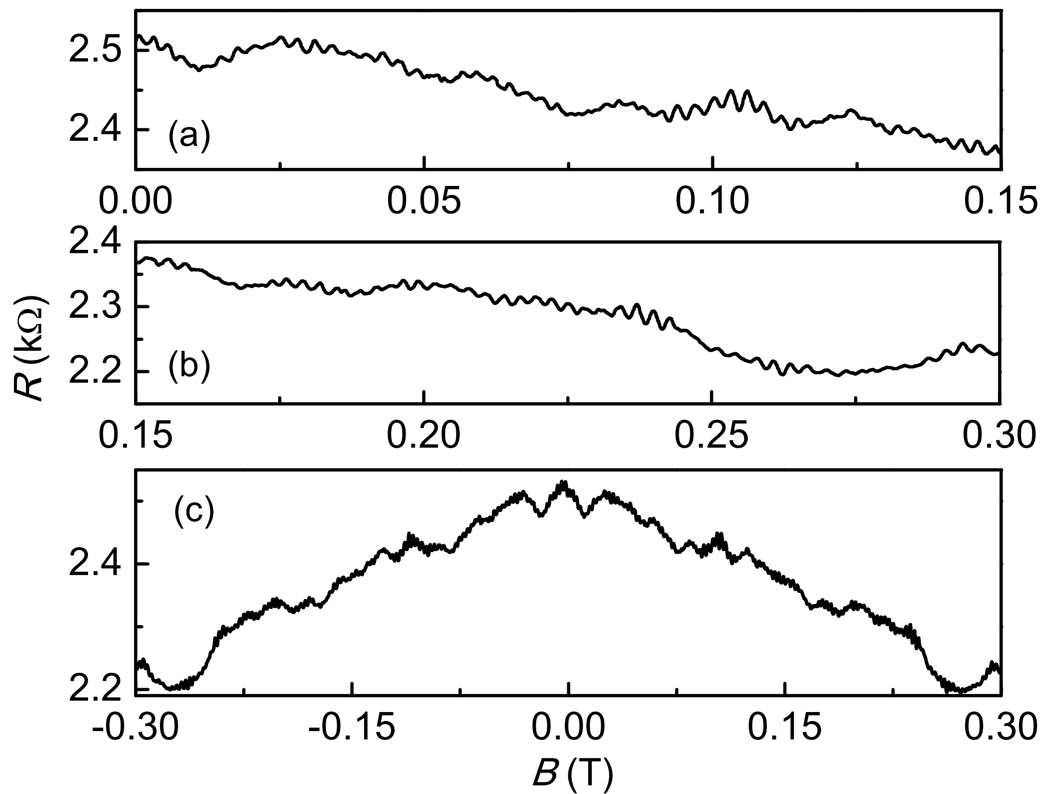

Figure 4.16: Measured Aharonov-Bohm magnetoresistance oscillations at 0.4 K, as ring resistance $R(B)$ versus B. Panels (a) and (b) show the ring magnetoresistance over smaller ranges of B than panel (c) which emphasizes a view of the modulation with B.

4.4.2 AB oscillations of a single AB ring at low magnetic field

The low B measurements are performed below 0.06 T at 0.4 K. A typical measurement around $B = 0$ T is presented in Fig. 4.10. Figure 4.10(a) contains the raw data, while Fig. 4.10(b) shows the same data after background magnetoresistance subtraction, and Fig. 4.10(c) presents the Fourier transform result. The Fourier transform displays a peak at $\sim$ 400 1/T, labeled as h/e, corresponding to the AB oscillations visible in Figs. 4.10(a) and (b), and corresponding to the h/e component of the spectrum. A smaller peak appears at $\sim$ 800 1/T, corresponding to the $h/(2e)$ component. The Fourier transform indicates a period in B of 25 G for the h/e component, consistent with the dimensions of the ring. Figures 4.10(a) and (b) show that the AB oscillation amplitude varies with a quasi-period of $\sim$ 200 G. A variation observed as described above was also addressed in detail in [34]. In the following two frameworks are provided to understand the modulation of the oscillation amplitude.

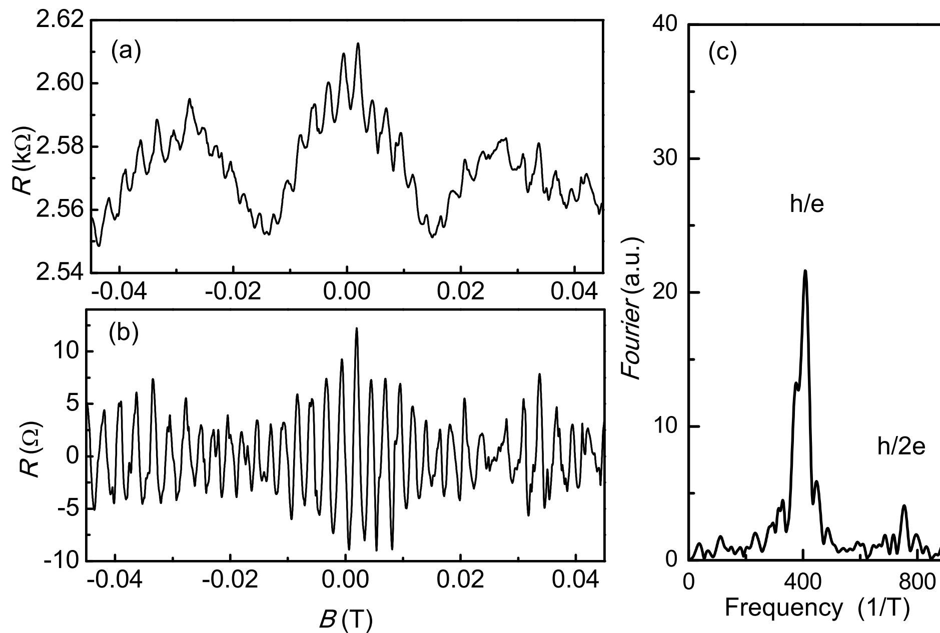

Figure 4.17: Aharonov-Bohm magnetoresistance oscillations around $B = 0$ at 0.4 K. Panel (a) shows the raw data, Panel (b) shows the data after background removal. Panel (c) contains the Fourier transform of (b), where h/e and $h/(2e)$ modes are indicated in the frequency spectrum.

Interferometer arms have a finite width w (lithographically in the present study, $w = 300$ nm, while the conducting width is narrower due to the existence of a depletion layer). The conducting arms form a mesoscopic system with properties, such as the complex transmis-

sion coefficient, that depend sensitively on the specific realization of the system. When the magnetic flux threading through the interferometer arms $\Phi_c = 2\pi r w B$ varies by $\sim \Phi_0$, a different realization is achieved and the ring's oscillation amplitude and phase are expected to be modified [34, 35]. The autocorrelation function in B of $R(B)$, expressed as $C(\Delta B) = \langle R(B)R(B+\Delta B)\rangle / \langle R(B)^2 \rangle$, decays according to the accumulated differences in realizations as the applied B varies. Its decay over ΔB, quantified by a correlation field B_c, is expected to form a measure of the magnetic flux necessary to delete correlations between realizations of the interferometer. Figure 4.11 presents the experimental $C(\Delta B)$ from the data in Fig. 4.10(b). Small-period oscillations in $C(\Delta B)$ should agree with the AB oscillation period [35], and indeed the fine oscillations in Fig. 4.11(a) show a period of 25 G. When performed on an infinite range of B, the envelope of $C(\Delta B)$ is expected to monotonically reach 0 as ΔB increases. Yet when performed on data necessarily finite over B, the envelope of the experimental $C(\Delta B)$ is non-monotonic, as Fig. 4.11 shows. The envelope [35] is expressed as $C(\Delta B/B_c) \sim (\frac{1}{(2\pi)^2} + \frac{1}{4\sqrt{2}\pi}\frac{\Delta B}{B_c} + \frac{1}{24}(\frac{\Delta B}{B_c})^2)\exp(-\frac{\pi}{\sqrt{2}}\frac{\Delta B}{B_c})$. Only the h/e component is considered in this expression, further valid for $T \to 0$. From Fig. 4.11 we deduce a fitted correlation field $B_c = 70$ G. The actual electrically conducting width w_e of the interferometer arms can then be estimated from $w_e = \Phi_0/(2\pi r B_c)$, yielding $w_e \approx 150$ nm. A depletion layer of 75 nm on each side of the arms lies within expectations for ICP-RIE etched InGaAs 2DESs at the n of the measurements. The view of the modulation as resulting from progressively uncorrelated realizations under varying B is hence in accordance with our data.

We now explore whether the quasi-periodic modulation can also be caused by existence of more than one preferred trajectory through the interferometer arms. In Fig. 4.10(c), two minor satellite peaks are noticed around the major h/e Fourier component. The satellites can be interpreted as originating from trajectories deviating from the geometric center of the arms, hence resulting in differing AB fluxes and periods. Careful analysis shows that the central major h/e Fourier component occurs at a frequency 408 1/T while the minor satellite peaks occur at 376 1/T and 447 1/T. Using these frequencies and their corresponding intensities, a simplified 3-component model is simulated as in Fig. 4.12. Comparing Fig. 4.12 with Fig. 4.10(b), we note the resemblance, quantified by the observation that the local minimum and local maximum points of the two curves' envelopes almost coincide. Corresponding to 408 1/T, 376 1/T and 447 1/T, the approximate radii are 734 nm, 704 nm and 768 nm respectively. These radii lie within the ring design. From this approach and using the observation that the fringes to the h/e component in the frequency spectrum extend over a wider range than considered in the simplified calculation, we can deduce that the electrically conducting width w_e must exceed 60 nm. The estimate $w_e > 60$ nm is consistent with the value $w_e \approx 150$ nm deduced from $C(\Delta B)$. While the use of $C(\Delta B)$ provides more quantitative information, both approaches to the amplitude modulation agree that the finite arm width and the resulting variation in magnetic flux can cause the modulation.

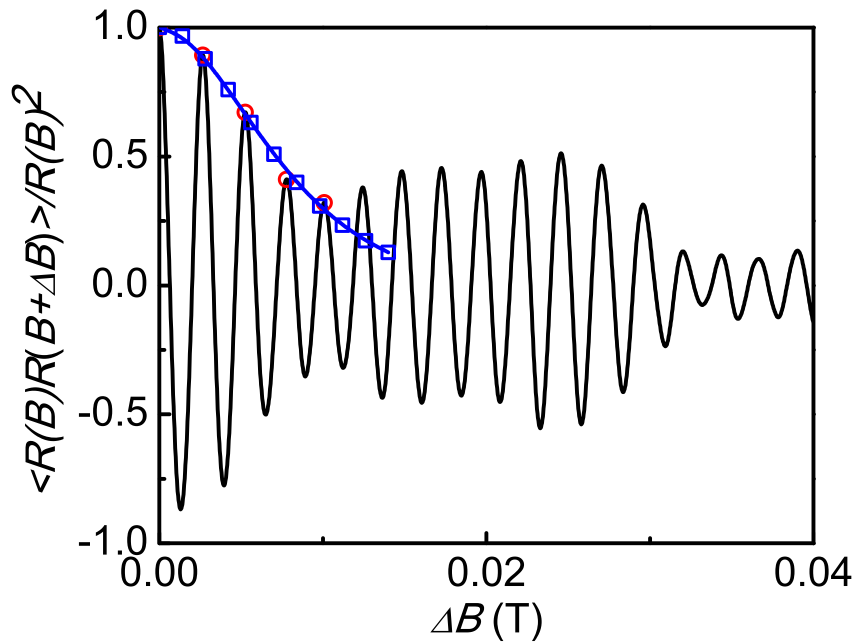

Figure 4.18: Black solid oscillatory line: the autocorrelation function in B of the Aharonov-Bohm oscillations in Fig. 4.10(b). Red open circles $\circ$: the maxima of the autocorrelation function, as a guide to the autocorrelation function envelope. Blue line with open squares $\square$: the fit to the autocorrelation function envelope, using the red open circles. The use of a finite range of B leads to deviations between fit and data at higher ΔB as discussed in the text.

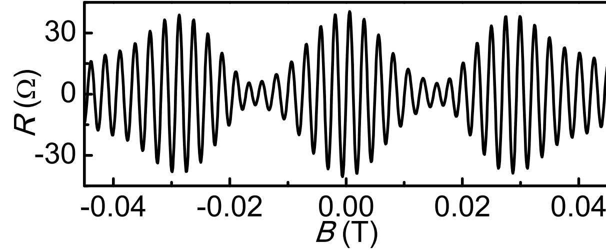

Figure 4.19: Modulation in the amplitude of Aharonov-Bohm oscillations simulated by using the 3 discrete frequencies deduced from the Fourier tansform in Fig. 4.10(c): 376 1/T, 408 1/T, 447 1/T, with intensities 13.2 Ω, 21.6 Ω, 5.89 Ω respectively.

4.4.3 AB oscillations of a single AB ring at higher magnetic field

AB oscillations are observed over a wide range of B. Figure 4.20 shows a typical measurement with B over -0.6 T to 0.6 T at 0.4 K. The AB oscillation period is too fine to be resolved on this scale. The AB oscillations occur on a background of universal conductance fluctuations, and of magnetoresistance caused by classical size effects. The inset of Fig. 4.20 shows a magnified view around 0.57 T, resolving the AB oscillations. At higher B, Shubnikov-de Haas oscillations gradually appear. Universal conductance fluctuations will be discussed more in other wire devices parts.

Experimentally, not all devices can perform well, yet this device shows good quality quantum interference. Thus, other measurements like the current and temperature dependence of AB oscillations, and the effect of an in-plane magnetic field on AB oscillations were performed. Further, an LED was used to improve the performance of this device in some measurements.

4.4.4 Current and temperature dependence of the AB oscillations in single AB ring

Transport measurements over the AB ring were performed under constant rms values of the ac excitation currents I and under constant T respectively for current and temperature dependence. Only the device "R082410" was used to study those properties. To ascertain the bias dependence of the AB oscillation amplitudes, the excitation voltage V_{exc} was calculated for each given I using the known ring resistance ($\approx$ 2.5 kΩ). For the bias dependence study, T was fixed to 0.4 K. For the study of the dependence on T, I was fixed at 20 nA, sufficiently low to achieve a saturation of the measured amplitudes, thereby ensuring that the finite excitation did not distort the results. The Thouless energy [37]

$$E_{\mathrm{c}} = \frac{\hbar}{\tau} = \frac{\hbar^2 k_{\mathrm{F}}}{m_e^* L} \tag{4.1}$$

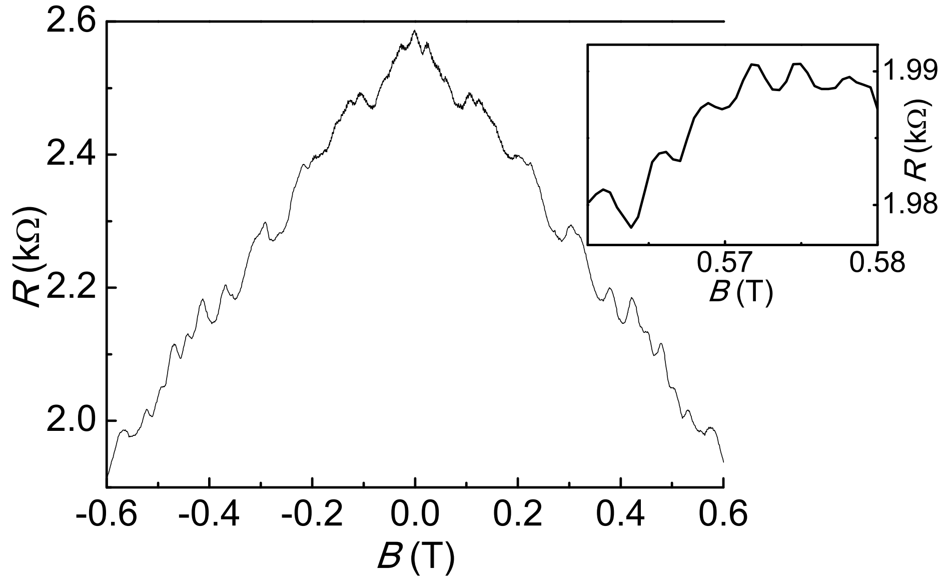

Figure 4.20: The ring magnetoresistance at 0.4 K over B from -0.6 T to 0.6 T. The Aharonov-Bohm magnetoresistance oscillations (not fully resolved on the scale of the graph) ride on universal conductance fluctuations. The inset shows a selected narrow range of B around 0.57 T to resolve the oscillations.

is used to as a critical energy scale to analyze the behavior of electrons, which is introduced in chapter 1.

Figure 4.21 shows that the oscillations weaken as I increases. For a detailed study of the relationship between I and AB oscillation amplitude, we selected a group of 10 adjacent periods from 0.01 T to 0.04 T, and calculated their mean amplitude. Results using this mean amplitude are depicted in Fig. 4.23(a). As I increases beyond a threshold, the amplitude overall decreases but shows a local maximum at $\sim$ 50 nA. Such non-monotonic behavior was also observed in other experiments [36], is called the lobe structure, and has been theoretically attributed to electron-electron interaction.

The T dependence is depicted in Fig. 4.22, showing a weakening of amplitudes with increasing T. For the analysis the same averaging method was applied as for the dependence on I, with results contained in Fig. 4.23(b). Within experimental uncertainty, the figure shows a mostly monotonic decrease with T.

We notice that variations in I and T do not modify the modulation in B, as can be ascertained from Figs 4.21 and 4.22. Unlike B, the parameters I and T hence do not induce new realizations of the entire mesoscopic system, at least not in the range used in this work. The AB oscillation amplitude decreases caused by I and T can be imputed to energy smearing, discussed above in the context of Eq. 4.1 expressing the Thouless energy scale E_{c}. Using

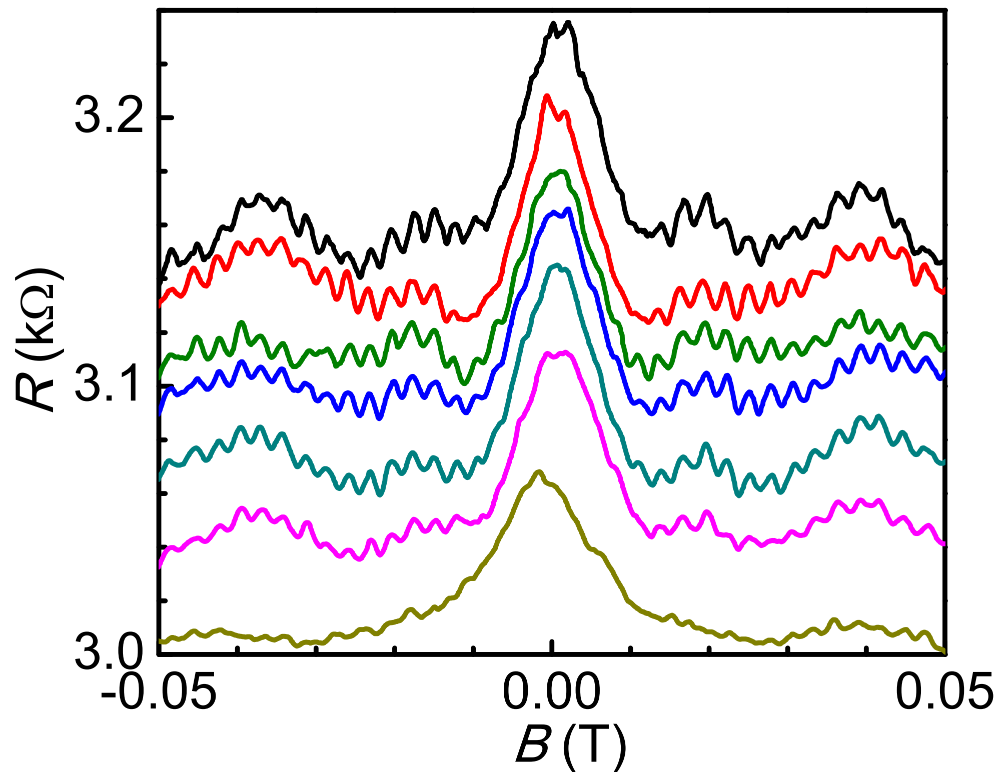

Figure 4.21: The excitation current dependence of the Aharonov-Bohm magnetoresistance oscillations at 0.4 K (data from the same sample as before, yet a different cool-down than for Figs. 4.9, 4.10 and 4.20). From top to bottom, the excitation current (rms values) is 5 nA, 10 nA, 20 nA, 50 nA, 100 nA, 200 nA and 500 nA respectively. Curves are offset, actual $R(B = 0) \approx 2.5$ kΩ.

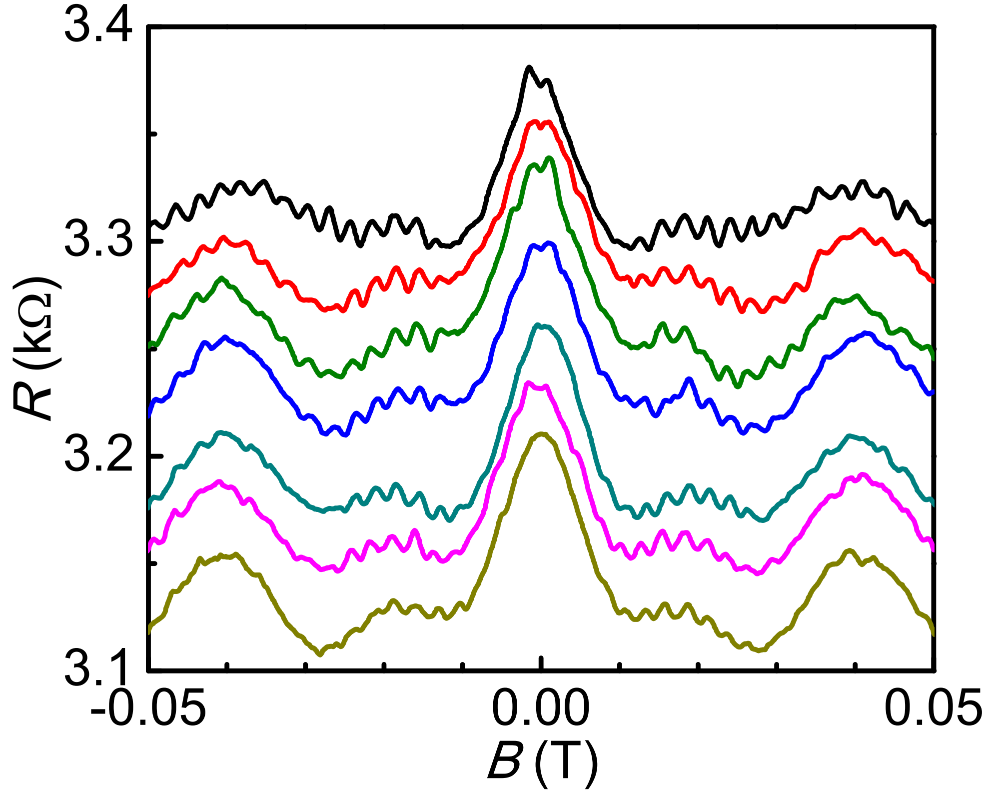

Figure 4.22: The T dependence of the Aharonov-Bohm magnetoresistance oscillations at 20 nA (data as in Fig. 4.21 from the first sample, yet a different cool-down than for Figs. 4.9, 4.10 and 4.20). From top to bottom T is 0.4 K, 0.6 K, 0.8 K, 1.0 K, 1.2 K, 1.4 K and 1.6 K respectively. Curves are offset, actual $R(B = 0) \approx 2.5$ kΩ.

$L = \pi r$ and the 2DES properties, Eq. 4.1 predicts an estimate of $E_\mathrm{c} = 2.4 \times 10^{-4}$ eV. A critical excitation current I_c can then be estimated by letting $\Delta E(I_\mathrm{c}) = E_\mathrm{c}$ (with $R = R(B = 0)$), and a critical temperature T_c by letting $\Delta E(T_\mathrm{c}) = E_\mathrm{c}$ (with $\kappa = 3$) [38]. The estimates yield $I_\mathrm{c} \approx 100$ nA and $T_c \approx 1.0$ K. When I or T exceed these critical values, averaging over incoherent channels gains in importance and the AB amplitude weakens proportionally to $\sqrt{E_\mathrm{c}/\Delta E}$ [39, 40]. The data in Fig. 4.23 is in accordance with the estimates of the critical values and with the $I^{-1/2}$ and $T^{-1/2}$ behavior predicted by Eq. 4.1. For finite mesoscopic systems relying on quantum coherence, such as the interferometric rings studied here, the Thouless energy hence serves as a predictor for loss of coherence.

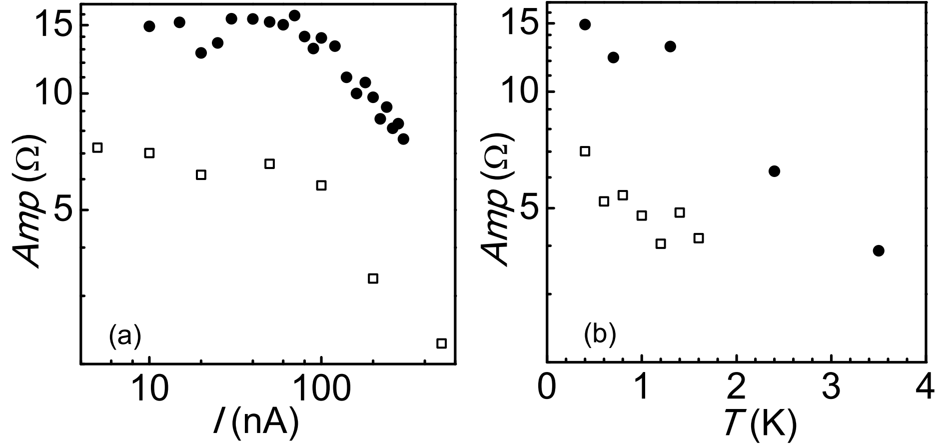

Figure 4.23: The excitation current and T dependence of the amplitude of the Aharonov-Bohm magnetoresistance oscillations (open squares □ and filled circles ∘ represent data from the first sample at different cooldowns). Panel (a) shows the excitation current dependence at 0.4 K with a logarithmic scale on both axes. Panel (b) shows the T dependence at 20 nA with a logarithmic scale on the vertical axis.

4.4.5 Spin-orbit Interaction and linear Rashba coefficient α

The spin-orbit interaction happens in this material as a result of structural inversion asymmetry (SIA) in $In_{0.64}Ga_{0.36}As/In_{0.45}Al_{0.55}As$ heterostructure. Electrons with opposite spin possess different Fermi wave vector which leads to two types of Shubnikov-de Haas oscillation. Figure 4.24 show the Fourier spectrum of Shubnikov-de Haas oscillation of this heterostructure $In_{0.64}Ga_{0.36}As/In_{0.45}Al_{0.55}As$ Hall bar at 0.4 K. $n_\downarrow$ and $n_\uparrow$ are used to denote the carrier density of the two energy bands with opposite electron spin. The two peaks marked with "spin down" and "spin up" are valued at $B_\downarrow = 20.4$ T and $B_\uparrow = 23.4$ T respectively. According to chapter 6 in book [80], $n_{\downarrow(\uparrow)} = eB_{\downarrow(\uparrow)}/h$, the Rashba coefficient α can be expressed as $\alpha = \sqrt{2\pi}\mu^*(\sqrt{n+\Delta n} - \sqrt{n-\Delta n}) = \mu^*|k_{F\uparrow} - k_{F\downarrow}|$, where n is the total carrier density, $\Delta n = |n_\uparrow - n_\downarrow|$, μ^* is the inverse effective mass $\mu^* = \hbar^2/(2m_e^*)$. Under this theory, the total electron density is $n = n_\downarrow + n_\uparrow = 1.05 \times 10^{16}$ m^{-2} which matches the value obtained by Hall effect measurement. Using electron effective mass $m_e^* = 0.035m_e$, Rashba coefficient is obtained as $\alpha = 1.9 \times 10^{-11}$ eVm. The effective magnetic field given by spin-orbit interaction is expressed as $B_{SOI} = (2k_F\alpha)/(g^*\mu_B)$, μ_B is Bohr magneton, k_F is the Fermi wave vector given by the total electron density, if g factor $g^* = 4$ for InGaAs is used, $B_{SOI} = 2.1$ T, which tells that there is strong orbit interaction in this $In_{0.64}Ga_{0.36}As/In_{0.45}Al_{0.55}As$ heterostructure. We also note that B_{SOI} is always in-plane and normal to the wave vector $\mathbf{k}$.

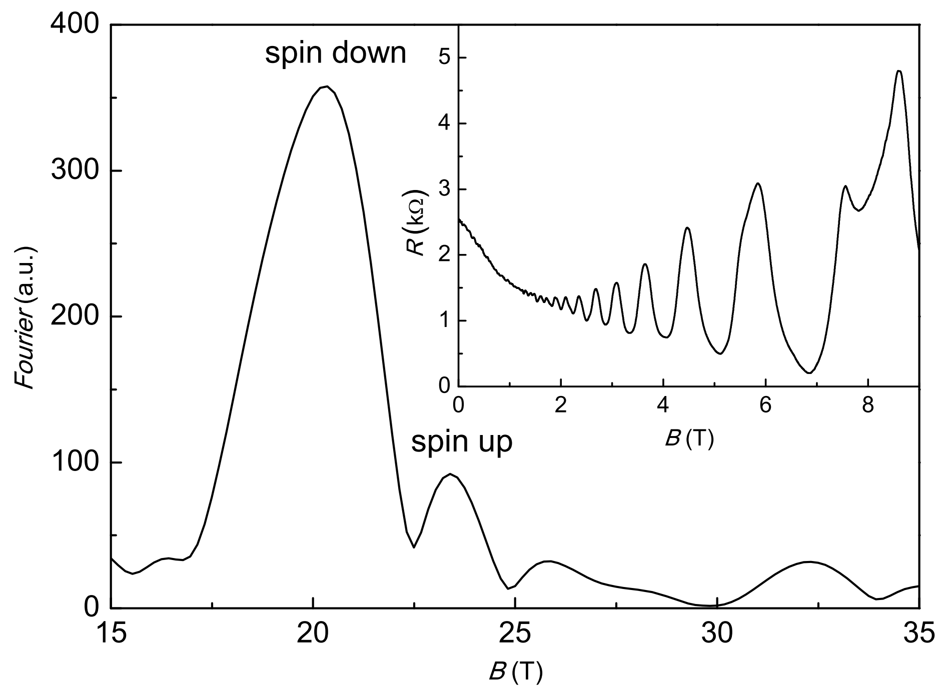

Figure 4.24: Fourier spectrum of Shubnikov-de Haas oscillation in the heterostructure InGaAs/InAlAs (Hall bar) at 0.4 K. The two peaks marked with "spin down" and "spin up" are the two frequencies of the Shubnikov-de Haas oscillations when plotted versus $1/B$. The inset shows the Shubnikov-de Haas oscillations up to 9 T.

4.4.6 Applying in-plane magnetic field to single AB ring

In order to apply an in-plane magnetic field to the device, we changed the probe to a probe with a rotatable socket which is introduced in chapter 3. As the direction of magnetic field of our setup is fixed vertically and the probe used above does not have a rotation mechanism. With this rotatable probe, a magnetic field with mixed perpendicular and in-plane components can be applied to a device.

Figure 4.25 depicts the setup for this measurement. B is perpendicular to the level line. The device can be rotated an angle between 0° to 90° by a built-in mechanism in the probe, thus an in-plane magnetic field component $B_{\parallel}$ can be applied to the device. As shown in Fig. 4.25, $B_{\parallel} = B\cos\beta$.

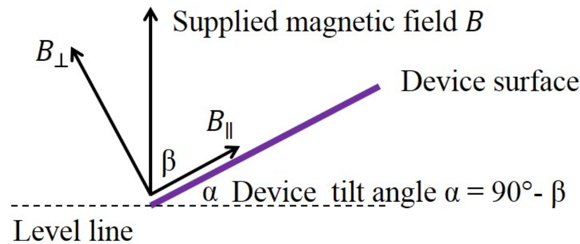

Figure 4.25: A schematic graph of the tilted setup.

With this setup, the in-plane magnetic field cannot be applied as exactly as the pure perpendicular magnetic field, and its range is also smaller. The tilt angle can be roughly set by the build-in mechanism. For each angle, a Hall effect measurement is made to calculate the actual angle as $\beta = \arcsin(R_H(\beta)/R_H(90°))$, where $R_H(\beta)$ and $R_H(90°)$ are Hall coefficients obtained by a linear fit to classic Hall effect measurements. Although β can be any value between 0° and 90° theoretically. As we tried to maintain the effective perpendicular magnetic field step the same in trials with different tilt angle, we cannot set the tilt angle too small. When β is below 5°, it requires a large sweep step, which may involve more error and uncertainty. The value of β used in experiments is not lower than 5°.

4.4.7 In-plane Zeeman effect induced Berry's phase and Aharonov-Casher phase change in single AB ring

The in-plane magnetic field is expected to generate a Zeeman effect to the 2D electron system. Zeeman effect can be expressed by $H_z = g^*\mu B$ in a Hamiltonian, which can introduce a phase difference to electrons with different magnetic moment in their propagation. As discussed before, the Thouless energy is the critical energy scale to indicate decoherence of a system. This study is performed in a regime where the Zeeman term is comparable to Thouless energy.

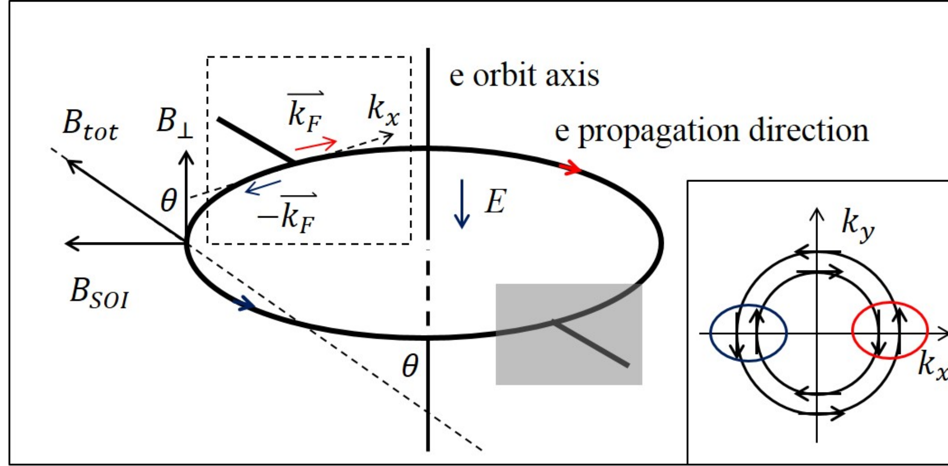

Figure 4.26: A schematic view of an AB ring with spin-orbit interaction. E is the effective electric field given by SIA of heterostructure. The inset depicts the spin splitting at Fermi surface due to SOI. In the dashed box, electrons propagate in two directions, the electrons' states can be described by the two circled positions in k space at the inset, and B_{SOI} is the effective magnetic field from SOI. The spin direction is parallel to B_{tot} due to the Zeeman effect, B_{tot} is the total magnetic field one electron feels. This graph only describes the case for one spin direction with a counterclockwise motion.

In this typical electron interferometer AB ring, not only AB oscillations can be observed, the Zeeman effect, a spin Berry's phase and a dynamical Aharonov-Casher (AC) phase are also revealed. The observation of Zeeman effect and Berry's phase and AC phase are all related in our device, and superposed on strong AB oscillations.

The following is an analysis of how the in-plane Zeeman effect causes the Berry's phase and AC phase to change, and further leads to a variation in periodicity of AB oscillation as seen in the Fourier spectrum of AB oscillation becoming broader around the main frequency when the in-plane magnetic field is large enough.

The AB effect is caused by the magnetic flux enclosed by two electron paths. Considering spin, two other kinds of phase can be involved, Berry's phase and AC phase, both requiring strong spin-orbit interaction (SOI) in the material. Figure 4.26 depicts a setup for this phenomenon, while the effective vector potential causing the AC phase is shown in Fig. 4.27.

In Fig. 4.26 it is assumed that the applied magnetic field is perpendicular to the 2DES and hence to the ring plane. In Fig. 4.26 it is also assumed that the spin $\boldsymbol{\sigma}$ and the magnetic moment $\boldsymbol{\mu}$ of the electron lie in the direction of B_{tot}, which is a vector sum of the applied $B_{\perp}$ and the in-plane B_{SOI}. Hence, the spin and magnetic moment are at angle θ to the normal. In Fig. 4.27 for clarity we assume $B_{\perp} = 0$, to illustrate the spin state under SOI. Due to SOI, the spin and momentum (k) are regarded as being locked normally to each other. The states are labeled as $\psi_{+/-}^{\uparrow/\downarrow}$, with $+/-$ indicating the k direction ($-$ means clockwise and $+$ means

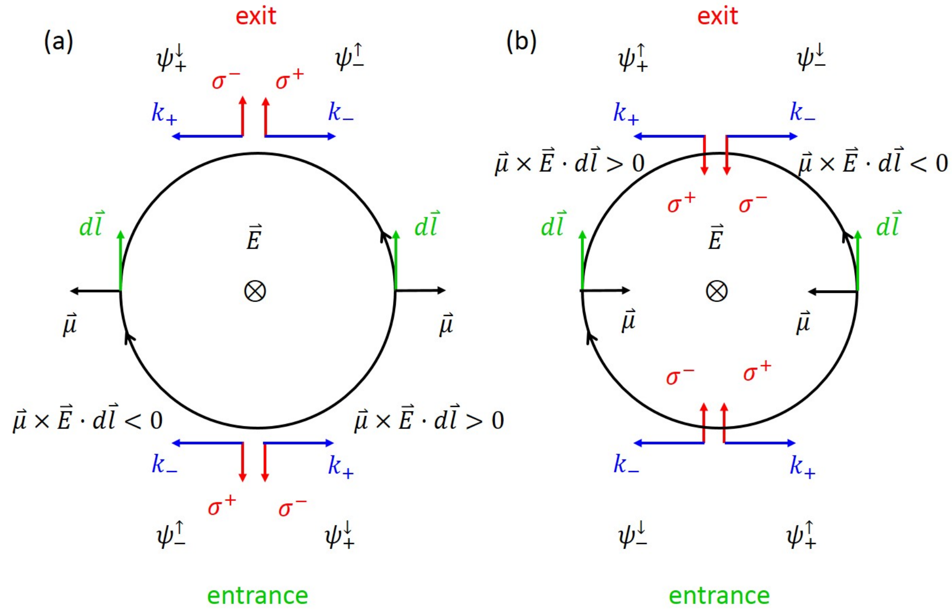

Figure 4.27: Schematic demonstration of AC effect. (a) and (b) demonstrate the same physics. For clarity, non orthogonal states for spin up and down are both shown in (a) and (b). Taking (a) as an example, it's a typical AB ring. Two electron waves propagate from the entrance point to the exit position through the left and right arms. The electron propagates through the left arm with spin up, the state is denoted as $\psi_-^\uparrow$. The electron propagates through the right arm with spin down, the state is denoted as $\psi_+^\downarrow$. $k_+/-$ denotes the propagating directions, k_+ means counterclockwise, k_- means clockwise. $\sigma^{+/-}$ denotes the spin directions, σ^+ means spin up, σ^- means spin down. The magnetic moment $\boldsymbol{\mu}$ is determined by spin $\boldsymbol{\sigma}$. The effective vector potential is determined by $\boldsymbol{\mu}\times\mathbf{E}$, where $\mathbf{E}$ is the effective electric field due to SOI. $\psi_-^\uparrow$ accumulates negative AC phase when it reaches exit point, $\psi_+^\downarrow$ accumulates positive AC phase when it reaches exit point.

counterclockwise) and $\uparrow / \downarrow$ the spin orientation relative to k. It can be shown [42, 43] that in a ring geometry only states with opposite k $(+/-)$ and opposite spin orientation relative to k $(\uparrow / \downarrow)$ will yield interference terms. Those opposite k states also, when propagating around the ring, will accumulate a relative phase difference due to AC phase. We regard the AC phase as originating in an effective vector potential $\mathbf{A}_{AC} = \frac{1}{c^2}\boldsymbol{\mu} \times \mathbf{E}$, where $\mathbf{E}$ is the effective Rashba electric field generated by the SIA in the heterostructure, and $\boldsymbol{\mu}$ lies in-plane and normal to k. In Fig. 4.27, the states $\psi_+^\downarrow$ and $\psi_-^\uparrow$, and the states $\psi_+^\uparrow$ and $\psi_-^\downarrow$ lead to interference terms ($\langle\psi_+^\downarrow|\psi_-^\uparrow\rangle \neq 0$, $\langle\psi_+^\uparrow|\psi_-^\downarrow\rangle \neq 0$). Two types of accumulated spin-induced phases will lead to a modulation of the interference. Firstly, $\mathbf{A}_{AC}$ will lead to a dynamical phase, akin to the AB phase, referred as $\phi_{AC}(B_\perp)$. Its dependence on an applied $B_\perp$ is made explicit here. Secondly, when applying $B_\perp$, the angle θ (Fig. 4.26) will induce a geometrical Berry's phase, $\phi_{Berry}(B_\perp)$. The applied $B_\perp$ also leads to the usual AB phase and accompanying interference.

There is a detailed discussion of Hamiltonian and wave functions considering SOI and its induced AC effects in the literature [42, 43, 44, 45, 46, 47]. In the setup as Fig. 4.26, using these theoretical results, we express the wave function of electron propagating counterclockwise and reaching the shadowed exit area of the ring in Fig. 4.26. If we denote by $\psi_{-,in}^\uparrow$ the wave function at the entrance of the ring (dashed box area), for clarity, we use the notations in Fig. 4.27, then $\psi_{-,out}^\uparrow = \psi_{-,in}^\uparrow \mathrm{exp}(\mathrm{i}(\phi_\mathrm{D} - \pi\pi \mathrm{r}^2\mathrm{B}/\phi_0 - 0.5\phi_\mathrm{Berry}(\mathrm{B}_\perp) - 0.5\phi_\mathrm{AC}(\mathrm{B}_\perp)))$, where ϕ_D is the dynamic phase $k\Delta L$ induced by the momentum over a path length ΔL, and the term $\phi_0 = h/e$ represents the flux accumulated by a 2π AB phase. We denote $\phi_{Berry}(B_\perp)$ as

$$\phi_{Berry}(B_\perp) = \pi(1 - \cos\theta) = \pi(1 - B_\perp/\sqrt{B_\perp^2 + B_{SOI}^2}) \tag{4.2}$$

and $\phi_{AC}(B_\perp)$ as

$$\phi_{AC}(B_\perp) = 2\pi m^* r\alpha \sin\theta/\hbar^2 = 2\pi m^* r\alpha B_{SOI}/(\sqrt{B_\perp^2 + B_{SOI}^2}\hbar^2) \tag{4.3}$$

Those phases are accumulated over a fulll revolution around the ring, hence the factors 0.5. Similarly, $\psi_{+,out}^\downarrow = \psi_{+,in}^\downarrow \mathrm{exp}(\mathrm{i}(\phi_\mathrm{D} + \pi(\pi \mathrm{r}^2\mathrm{B}_\perp)/\phi_0 + 0.5\phi_\mathrm{Berry}(\mathrm{B}_\perp) + 0.5\phi_\mathrm{AC}(\mathrm{B}_\perp)))$. The signs before $\pi(\pi r^2 B_\perp)/\phi_0$, $\phi_{Berry}(B_\perp)$ and $\phi_{AC}(B_\perp)$ of the two half opposite directed trajectories are always opposite. We note that the $\sin\theta$ in ϕ_{AC} appears due to the fact that $\boldsymbol{\mu}$ lies parallel to B_{tot} (Fig. 4.26) and hence $\boldsymbol{\mu} \times \mathbf{E} = \mu E \sin\theta$.

If spin is ignored, the interference term of two electron waves from the two arms of AB ring at the exit point in Fig. 4.27 can be expressed as $\langle\psi_+|\psi_-\rangle = A_- A_+ \cos(2\pi(\pi r^2 B_\perp)/\phi_0)$, where A_- and A_+ denoting the amplitudes of the two wave functions of the arms. This result assumes the left and right arms are symmetric, thus $\psi_-(B_\perp)$ and $\psi_+(B_\perp)$ gain an identical dynamic phase $\phi_D(B_\perp)$ which is canceled in $\langle\psi_+|\psi_-\rangle$. In a magnetotransport measurement, an oscillation with the expected periodicity of the AB effect appears. We denotes $\phi_{AB}(B_\perp) = 2\pi(\pi r^2 B_\perp)/\phi_0$.

The following demonstration of interference considering spin is based on Fig. 4.27. Interference of $\psi_+^\downarrow$ and $\psi_-^\uparrow$ yields $\langle\psi_+^\downarrow|\psi_-^\uparrow\rangle = A_+^\downarrow A_-^\uparrow \cos(\phi_{AB}(B_\perp) - \phi_{Berry}(B_\perp) - \phi_{AC}(B_\perp))$. Interference of $\psi_+^\uparrow$ and $\psi_-^\downarrow$ yields $\langle\psi_+^\uparrow|\psi_-^\downarrow\rangle = A_+^\uparrow A_-^\downarrow \cos(\phi_{AB}(B_\perp) + \phi_{Berry}(B_\perp) + \phi_{AC}(B_\perp))$. The notations of $A_{+/-}^{\uparrow/\downarrow}$ are the amplitudes of the corresponding wave functions.

Berry's phase and AC phase modify the periodicity of AB oscillation. However, this modification is not visible in a magnetotransport measurement. As the applied perpendicular field $B_\perp$ varies one period B_T (due to $\phi_{AB} + \phi_{Berry} + \phi_{AC}$) from $B_{i\perp}$ to $B_{f\perp}$, the AB phase change $\phi_{AB}(B_\perp)$ is almost 2π, Berry's phase change is $\Delta\phi_{berry} = |B_{f\perp}/\sqrt{B_{f\perp}^2 + B_{SOI}^2} - B_{i\perp}/\sqrt{B_{i\perp}^2 + B_{SOI}^2}|$, AC phase change is $\Delta\phi_{AC} = |B_{SOI}/\sqrt{B_{f\perp}^2 + B_{SOI}^2} - B_{SOI}/\sqrt{B_{i\perp}^2 + B_{SOI}^2}|$. In our experiment, B_T is around 0.0028 T, B_{SOI} is around 2.1 T calculated in previous section. If we take the initial perpendicular magnetic field $B_{i\perp} = 0.1$ T, we will get $\Delta\phi_{berry} = 0.001$ rad and $\Delta\phi_{AC} = 0.0001$ rad. Thus the effect of Berry's phase and AC phase on frequency of those oscillations in magnetotransport measurement is small. However, Berry's phase and AC phase can give an observable effect on modulation of amplitudes.

The oscillation part of total interference considering spin can be expressed as $P_o(B_\perp) = A_+^\downarrow A_-^\uparrow \cos(\phi_{AB}(B_\perp) - \phi_{Berry}(B_\perp) - \phi_{AC}(B_\perp)) + A_+^\uparrow A_-^\downarrow \cos(\phi_{AB}(B_\perp) + \phi_{Berry}(B_\perp) + \phi_{AC}(B_\perp))$. When a large enough in-plane magnetic field is applied, the condition for Berry's phase and AC phase to accumulate is strongly modified,because the in-plane magnetic field component $B_\parallel$ will be vectorially added to B_{SOI}. Berry's phase and AC phase will be modified in a complex way.

If assuming AB ring's left arm and right arm are symmetric and $A_+^\downarrow A_-^\uparrow = A_+^\uparrow A_-^\downarrow$, then

$$P_o(B_\perp) = 2A_+^\downarrow A_-^\uparrow \cos(\phi_{Berry}(B_\perp) + \phi_{AC}(B_\perp))\cos(\phi_{AB}(B_\perp)) \tag{4.4}$$

As B varies, $\cos(\phi_{Berry}(B_\perp) + \phi_{AC}(B_\perp))$ will modify the amplitude of AB oscillation. If only perpendicular magnetic field is applied, the amplitude modulation is caused by a mixture of Berry's phase and AC phase and other factors (only $B_\perp$ is considered) which were discussed in our previous paper [48] and other literature [34]. However, if an in-plane magnetic field is applied, it will modify $\phi_{Berry}(B_\perp) + \phi_{AC}(B_\perp)$ even without $B_\perp$ change. If an amplitude difference between two AB oscillations with different in-plane magnetic field $B_\parallel$ and the same perpendicular magnetic field $B_\perp$ is observed, this difference should be caused by the change of Berry's phase and AC phase (Eq. 4.5).

Our observation of the expected phenomenon is presented below. References [49, 50] also observed a similar phenomenon and denoted it as an AC phase. In their experiment, gate voltage was applied to change Rashba coefficient α, thus inducing a change in AC phase. In our experiment, in-plane magnetic field was applied to modify Berry' phase and AC phase.

Using the tilt setup, we can apply an in plane magnetic field to the AB ring. We performed this experiment at 1.2 K. The current through AB ring is 20 nA. Two regimes were focused on, perpendicular magnetic field $B_\perp$ around 0 T and $B_\perp$ around 0.15 T. Those measured

results are shown in Fig. 4.28.

Obvious modulation can be observed in almost every curve in Fig. 4.28. The main reason for the modulation was explain in [48]. The nonzero width of AB ring arm causes a flux modification for the AB oscillation. Shadowed stripes are used to separate the total data into 20 groups. Each group has the same perpendicular magnetic field. As we discussed before in [48], where only perpendicular magnetic field $B_{\perp}$ is considered, strong correlation happens within a region of 0.007 T on average. It means when $B_{\perp}$ varies by more than 0.007 T, the states in the 2DES tend to be changed. This change leads to a modification of the shape of AB oscillation, presenting as modulation. Thus it doesn't matter how to separate the data into groups, as long as the span range is not too large to reduce the difference between average amplitudes of different curves within one stripe.

The expression of Berry's phase and AC phase stated previously are valid when the in-plane Zeeman effect can be ignored. Using the Rashba coefficient of this heterostructure $\alpha = 1.9 \times 10^{-11}$ eVm obtained in last section, we have

$$\phi_{Berry} + \phi_{AC} = 11.3\pi\sin\theta + \pi(1 - \cos\theta) \tag{4.5}$$

θ is calculated by

$$\tan\theta = \mathrm{B_{SOI}}/\mathrm{B_{\perp}} \tag{4.6}$$

If the in-plane Zeeman effect is large enough, θ varies during one revolution. This causes $\cos(\phi_{Berry}+\phi_{AC})$ in Eq. 4.4 to vary at the same $B_{\perp}$ but different $B_{\parallel}$ and gives a modification to the amplitude of curves with different $B_{\parallel}$ at the same $B_{\perp}$ region. Taking the stripes 4, 8, 11, 15, 19 in Fig. 4.28 as examples, θ does not vary much in each group when in-plane Zeeman effect is small. The center $B_{\perp}$ in each group is used to calculate the value of $\cos(\phi_{Berry}+\phi_{AC})$ without considering the in-plane magnetic field. The center $B_{\perp}$ for stripes 4, 8, 11, 15 and 19 are 0 T, 0.08 T, 0.111 T, 0.166 T and 0.214 T. The corresponding values of $\cos(\phi_{Berry}+\phi_{AC})$ without considering in-plane magnetic field are 0.588, 0.699, 0.747, 0.833, 0.904. As $B_{\parallel}$ increases, $\cos(\phi_{Berry} + \phi_{AC})$ is modified, and AB oscillations amplitude changes even at the same perpendicular magnetic field.

Looking at the data in stripe 15, the oscillations amplitudes are small with larger tilt angles and become large when the tilt angle is 6°. This means $\cos(\phi_{Berry}+\phi_{AC})$ is small when only considering $B_{\perp}$ according to Eq. 4.4, but the value calculated above is 0.833. One possible reason for this mismatch is that Eq. 4.2 and Eq. 4.3 are sensitive to B_{SOI} and α. But B_{SOI} and α are obtained experimentally, and have errors. Thus we shouldn't rely on the concrete value, but the changing of $\phi_{Berry} + \phi_{AC}$. As $\phi_{Berry} + \phi_{AC}$ varies, the amplitudes of AB oscillations vary correspondingly.

The amplitude change may be caused by other reasons. If the same experiment is performed on a device without SOI and no amplitude change is observed, then we could be sure that the phenomenon happened in our experiment is caused by change of $\phi_{Berry} + \phi_{AC}$.

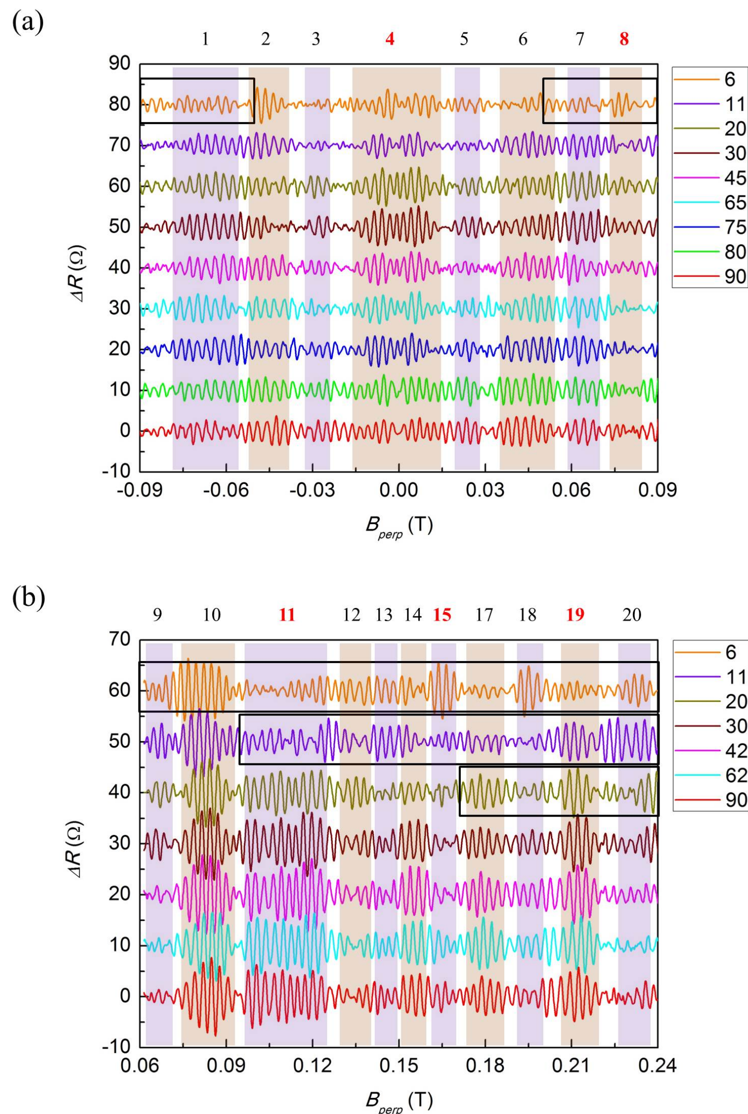

Figure 4.28: Measurements in a tilted setup as depicted in Fig. 4.25. The tilt angle β varies between 6° and 90° from top to bottom. In-plane magnetic field is $B_{\parallel} = B_{\perp}/\tan\beta$. The curves background was removed and curves' vertical positions are offset for clarity. (a) are results around 0 T, (b) are results around 0.15 T. Shadowed stripes on curves indicate a group of AB oscillations. As we discussed in [48], strong correlation is within a region of 0.007 T for $B_{\perp}$ averagely. There is no meaning to compare oscillations horizontally, only but vertically in each shadowed stripe. The total field is greater than 0.5 T in the regions marked with solid boxes. The value 0.5 T is obtained by setting the Zeeman energy to equal the Thouless energy.

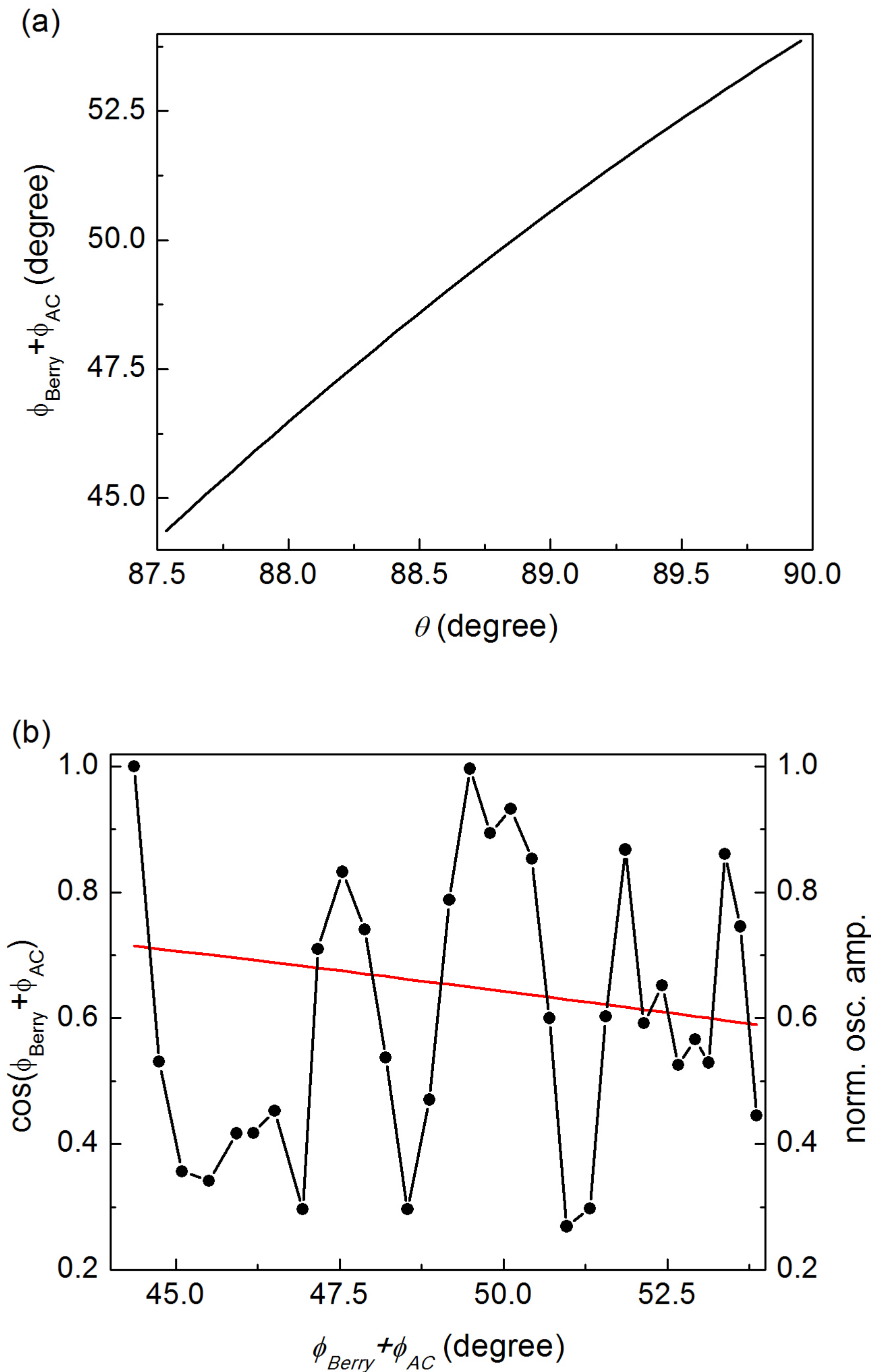

Figure 4.29: The figures are related to the 90° curve in Fig. 4.28(a). (a) depicts the relation of $\phi_{Berry} + \phi_{AC}$ and θ (Eq. 4.5). In (b), the red solid curve shows the value of $\cos(\phi_{\mathrm{Berry}} + \phi_{\mathrm{AC}})$, with $\phi_{Berry} + \phi_{AC}$ obtained in (a); the black line with dots shows the normalized oscillation amplitudes obtained from the 90° curve in Fig. 4.28(a), corresponding to the right vertical axis.

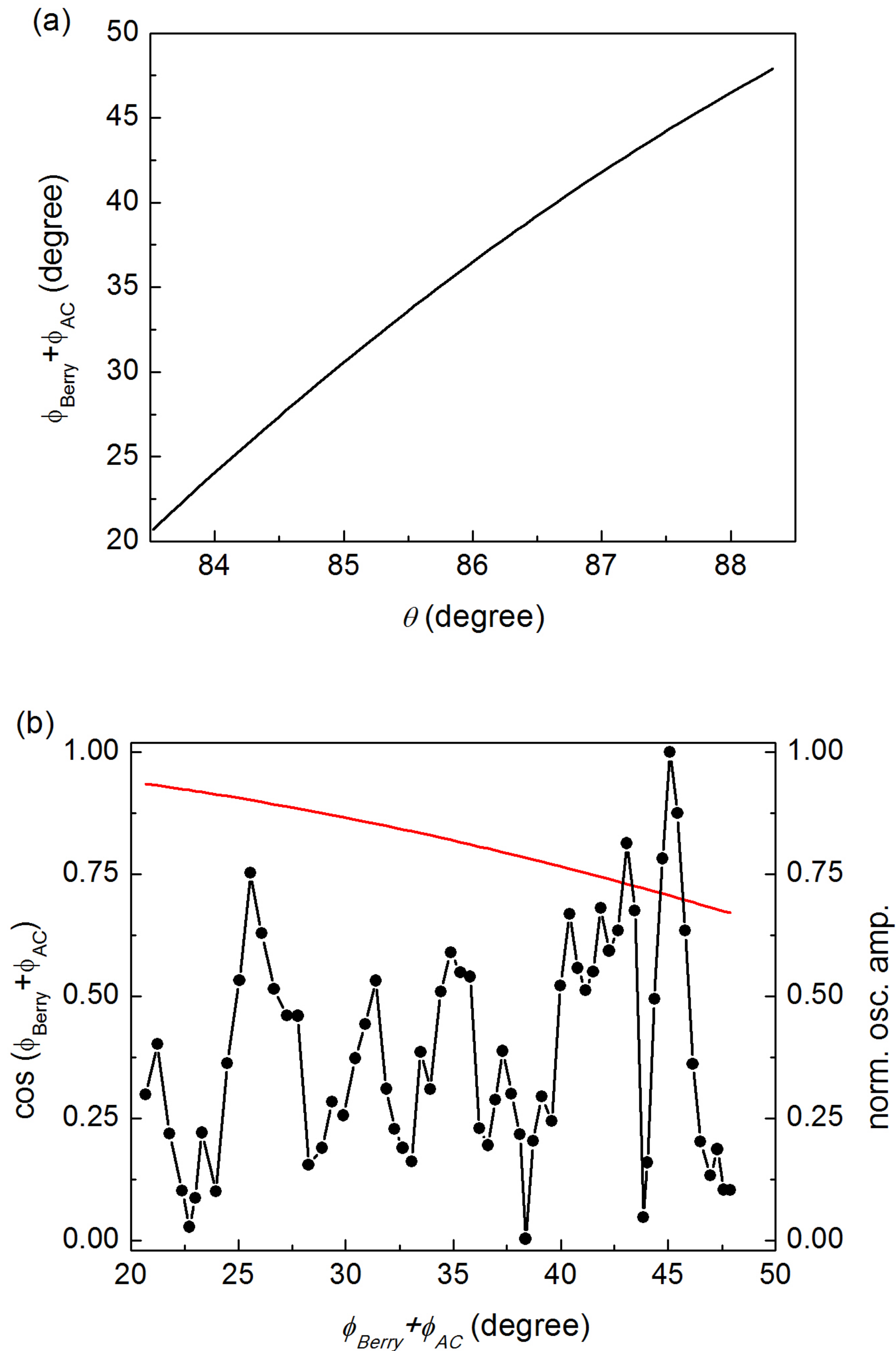

Figure 4.30: The figures are related to the 90° curve in Fig. 4.28(b). (a) depicts the relation of $\phi_{Berry}+\phi_{AC}$ and θ (Eq. 4.5). In (b), the red solid curve shows the value of $\cos(\phi_{\text{Berry}}+\phi_{\text{AC}})$, with $\phi_{Berry}+\phi_{AC}$ obtained in (a); the black line with dots shows the normalized oscillation amplitudes obtained from the 90° curve in Fig. 4.28(b), corresponding to the right vertical axis.

Figures 4.29 and 4.30 contain an analysis of the 90° curves in Fig. 4.28. We extracted the oscillation amplitudes and their corresponding $B_{\perp}$. With $B_{\perp}$, we obtained θ by Eq. 4.6. Then $\phi_{Berry} + \phi_{AC}$ was obtained by Eq. 4.5, which are shown in Fig. 4.29(a) and 4.30(a). Thus we could create datapoints of $(\phi_{Berry} + \phi_{AC}, normalized\ oscillation\ amplitude)$, with the data shown by the black curves with dots in Fig. 4.29(b) and 4.30(b). The solid red curves in Fig. 4.29(b) and 4.30(b) are $\cos(\phi_{\mathrm{Berry}} + \phi_{\mathrm{AC}}$ and $\theta)$. Those figures tell us that the value of $\cos(\phi_{\mathrm{Berry}} + \phi_{\mathrm{AC}}$ is not consistent with the experimental normalized oscillation amplitudes. This means the modulation is caused by more factors than $\phi_{Berry} + \phi_{AC}$, as we expected.

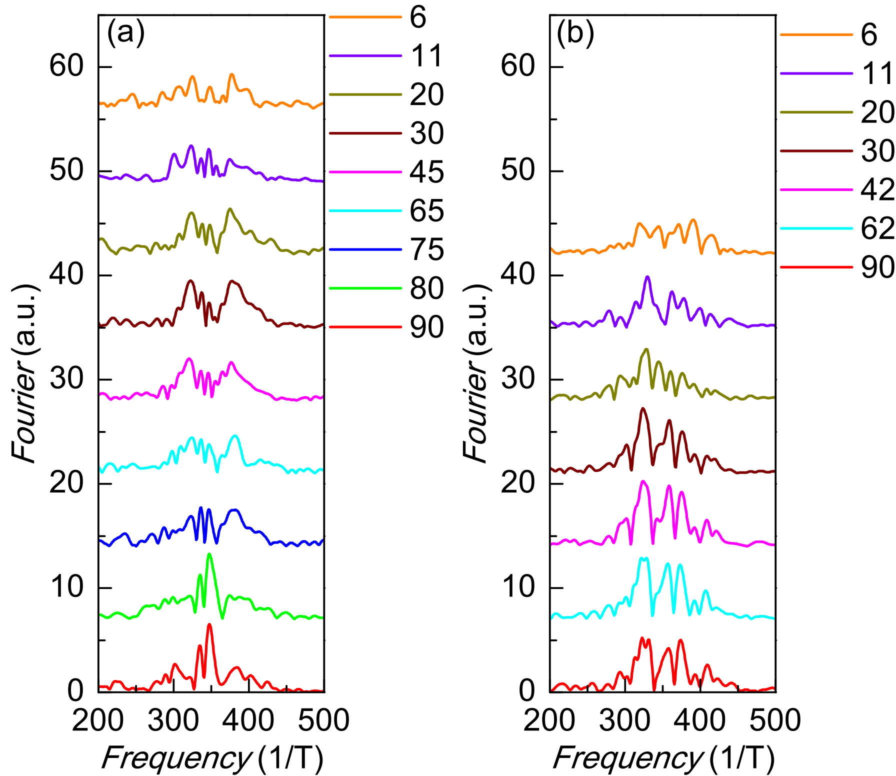

Figure 4.31: Fourier spectrum of the measurements in Fig. 4.28. (a) is for Fig. 4.28(a), and (b) is for Fig. 4.28(b). These Fourier spectrum curves are offset vertically for clarity.

Figure 4.31 shows the Fourier spectra for the results in Fig. 4.28. The peaks show the h/e AB oscillation mode. When the in-plane magnetic field $B_{\parallel}$ increases, Fourier spectra tend to have a more broad spectrum compared to the data with same $B_{\perp}$ but lower $B_{\parallel}$. This means that the quantum interference between states is increasingly affected by increasing $B_{\parallel}$. This leads us to identify another mechanism by which our AB oscillation data in in-plane magnetic field can be explained, possible operating in addition to the spin-induced mechanism explained above. This mechanism (below) is based on the concept of Thouless

energy. In [48] we used Thouless energy [37] E_{Th} as energy scale to indicate the effect of a perturbation on a 2DES. $E_{Th} = 0.24$ meV was obtained. If the perturbation energy is greater than this value, the features of AB oscillations change. Previously we discussed dephasing, now we look at the Fourier spectra of AB oscillations at different in-plane magnetic field. The Zeeman energy $H_Z = -g^*\mu_B B$ is a perturbation term. Setting $E_{Th} = g^*\mu_B B$, a critical field $B_c = 0.5$ T is obtained. In Fig. 4.28, the regions with total magnetic field greater than 0.5 T are marked by solid boxes. The Fourier spectra for those data sets with solid boxes have a more wide and fuzzy spectrum, which is consistent with the effect of Thouless energy E_{Th}.

4.5 AB ring array

The above single AB ring gives strong AB oscillations. This section will present oscillations in a 5×5 AB ring array. There are two types of interferometry involved in this device, Mach-Zehnder interferometry and Sagnac-type interferometry. Those two types interferometry are depicted in Fig. 4.32. MZ interferometry relies on spatial symmetry, Sagnac-type interferometry relies on time-reversal symmetry. In our experiments, the device is loaded into 0.4 K environment, and a perpendicular sweep magnetic field is applied. As the magnetic field varies, an oscillation of electron interferometry is observed, the oscillation of MZ interferometry is AB oscillation and the oscillation of Sagnac-type interferometry is AAS oscillation. AB oscillation has a periodicity in magnetic flux $\frac{h}{e}$, AAS oscillation has a periodicity in magnetic flux $\frac{h}{2e}$.

In the following discussion, two concepts are used, local flux and non-local flux, which are defined as Fig. 4.33 shows. In an ideal AB effect setup, magnetic flux only threads through the central area where electron is not passing, which is the non-local flux. Practically, we apply a uniform magnetic field to the device, and the magnetic flux threading the electron path, which is the local flux affects electron interference. When we calculate the periodicity of oscillations, only the non-local magnetic flux is counted. The local flux causes the AB oscillation to have a modulation over magnetic field which is discussed in previous section 4.4. In this section, we will discuss how the local flux breaks time-reversal symmetry by analyzing AAS oscillations over magnetic field.

4.5.1 Overview of AB and AAS oscillations in AB ring array

In a ring chain, the electron path's geometry is more complicated than a single ring, however, concerning the periodicity of oscillations, we can treat each ring individually. The phase information of each branch is in fact reserved when electron travels from one ring to another. Figure 4.34 depicts the situation of the AB effect in a chain of rings. Initially, an electron

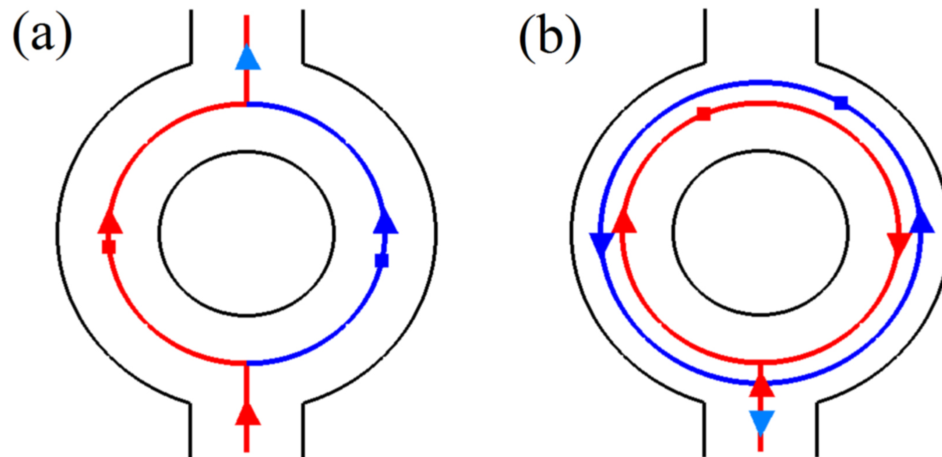

Figure 4.32: (a) Mach-Zehnder (MZ) interferometer, based on trajectories in spatially separate arms. (b) Sagnac-type interferometer, based on exact time-reversed trajectories (for clarity, trajectories are shown spatially non-overlapping).

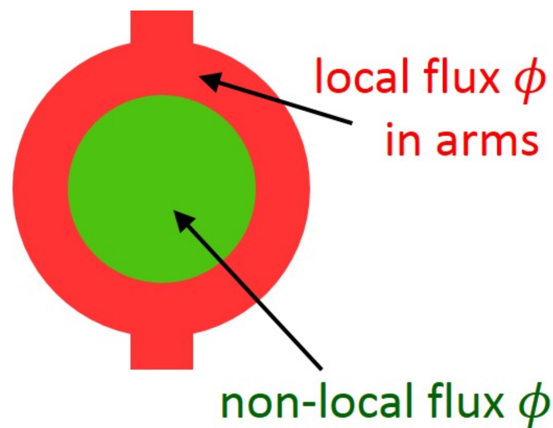

Figure 4.33: Schematic graph to show local flux and non-local flux, the red ring area is electron path, the green central area excludes electrons.

beam splits into two branches by the first ring, before electrons travel to the second ring, the two electron branches unite into a new beam with its own phase information, and this chain performs as a juxtaposition of two individual AB rings. There may exist some paths as the red dashed lines show, which is ignored in the analysis below.

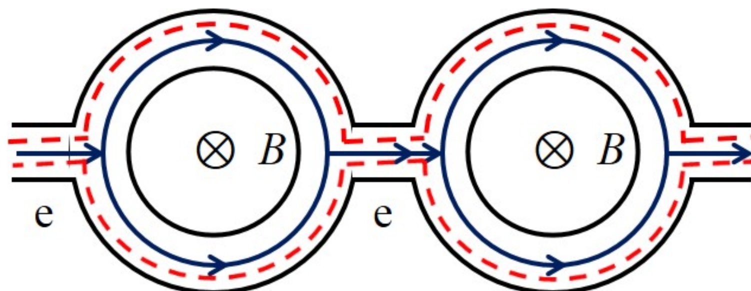

Figure 4.34: AB effect in a chain of rings, the first ring splits the original electron beam into two branches, before they travel to the second ring, these two branches unite into a new electron beam. Solid dark blue lines depict one most likely electron path, dashed red lines depict another choice of electron path.

For different parallel chain of rings, as the space between each chain is about 2.2 μm which is greater than the quantum interference scale, the interference between these chains can be ignored.

Therefore, as concerning the periodicity in B, the 5×5 AB ring array can be taken as 25 individual AB rings combined together, which simplifies the analysis a lot and turns out to be consistent with the observed result.

Sagnac-type interferometry (AAS oscillation) is slightly more likely to happen when AB rings are connected as a chain at low magnetic field. Figure 4.35 depicts the situation when Sagnac-type interferometry happens, solid green line and dashed red line indicate the two directed paths of electrons. Considering the counter-clock-wise solid green line electron path, if the structure only contains a single AB ring, there could be more possibility for the electron to go forward when half circle is passed than the situation when two AB rings are connected. When electron reaches the neck between these two rings, there is slightly more possibility for the electron to go backward along the ring than the single AB ring case. Then the electron forms a full circle path. This also happens to the clock-wise traveling electrons. Note that below we present the reason why the MZ interference oscillations are happened in an array. Electron interference happens when electrons in these two directed full circle paths meet at the incident position.

The AAS oscillations reveal the time-reversal symmetry of electrons in this mesoscopic system. When a large enough magnetic field is applied to this mesoscopic system, time-reversal symmetry is broken, however, while when the field is weak enough, AAS oscillation can still be observed.

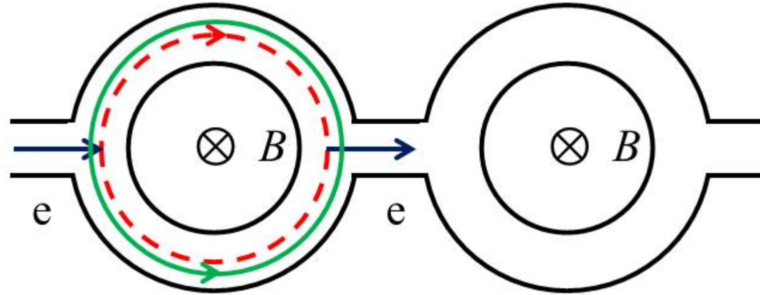

Figure 4.35: A schematic description of AAS oscillations in an AB ring. The solid green line and dashed red line indicate the two directed paths of electrons, they are time-reversed states of each other. A magnetic field is applied uniformly across the rings' surface.

In a single MZ interferometer the spatial asymmetry between the two arms, originating in fabrication and materials imperfections, can give rise to an additional phase shift between two partial waves if each samples only one arm [54, 55, 56]. Hence if a finite number of MZ interferometers are concatenated, ensemble averaging will diminish the measured conductance oscillation amplitude [57, 58, 59, 60, 61, 62]. Yet, trajectories through the interferometer arms exist which are immune to such spatial asymmetry, namely exact time-reversed trajectories which probe both interferometers arms in a time-reversed scattering sequence. Via the AB phase the time-reversed trajectories give rise to AAS conductance oscillations, and these survive ensemble averaging over a network of interferometers [54, 57, 63, 64, 65, 66]. Interference phenomena relying on time-reversed trajectories are typical of Sagnac-type interferometers (Fig. 4.32(b)).

The AAS oscillations, induced by the AB phase but relying on time-reversal symmetry, appear with a periodicity in ϕ of $h/2e$ since they enclose the flux twice. In the same mesoscopic ring geometries (Fig. 4.32), the AB phase thus induces both MZ interferometric oscillations relying on spatial symmetry and with periodicity h/e, and Sagnac-type interferometric oscillations (AAS oscillations) relying on time-reversal symmetry and with periodicity $h/2e$. In large arrays of interferometers, ensemble averaging and spatial asymmetry will lead to dominance of the $h/2e$ AAS oscillations over the MZ oscillations. Yet AAS oscillations require time-reversal symmetry, broken by B. If magnetic flux penetrates the interferometer arms (which we will refer to as local ϕ), rather than only the space between interferometer arms (non-local ϕ), then time-reversal symmetry in the arms will be broken and the AAS oscillation amplitude will decay [54, 58, 63, 66, 67, 68]. Typical experiments are performed by applying a uniform B, resulting in both local and non-local ϕ, and hence an AAS amplitude diminishing with $|B|$ is observed. This decay of the AAS quantum interference phenomenon is akin to the disappearance of the quantum corrections of weak-localization and antilocalization with increasing $|B|$. In contrast MZ oscillations relying on spatial symmetry, nominally survive to high B. In MZ interference, rather than a decay of the amplitude, a modulation of the amplitude approximately periodic in the local ϕ is observed [48].

Figure 4.36 depicts the measurement configuration of a 5×5 AB ring array. A low frequency AC current with constant RMS value is supplied through contacts 1 to 5, the voltage signal is collected from contacts 8 and 7 or 8 and 6. A magnetic field perpendicular to the surface is supplied during measurements, varying from -2.3 T to 2.3 T, with experimental steps below 1 G.

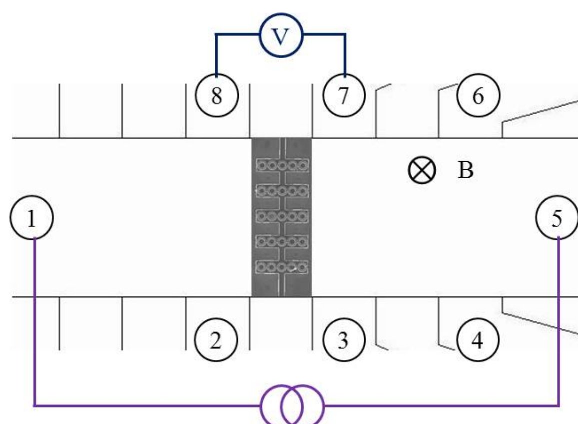

Figure 4.36: Schematic view of the measurement configuration of a 5×5 AB ring array.

Several cool-downs were performed on this device and a fine magnetic field step (about 1.15 G above 600 G, 0.7 G below 600 G) sweep was performed in the whole magnetic field range that this system can reach. AAS oscillations were observed in range -200 G to 200 G, AB oscillations were observed in the whole range -2.3 T to 2.3 T, the results are shown in Fig. 4.37, 4.38, 4.39.

The heterostructure material used for this AB ring array device is the same as the material for the previous AB ring device, however an LED was used for this device fo the measurements. Therefore the property of the 2DES was altered slightly. The 2DES density $n = 1.1 \times 10^{12}$ cm^{-2} is calculated from Hall coefficient at 0.4 K, the 2DES resistivity is $\rho_{2D} = 120\ \Omega/\Box$ at 0.4 K, the corresponding mobility is $\mu = 4.7 \times 10^4$ cm^{-2}/(Vs). These are the transport property values after LED shone on the device for a while to excite more carriers. Compared to the original material, n increases about 7%, ρ_{2D} increases and μ decreases, the mean free path l_e decreases from 1.73 μm to 1.54 μm.

4.5.2 AAS oscillations at different magnetic field regime

This Sagnac interferometer has strong oscillation signals at low field. The signal is a combination of AAS oscillations and AB oscillations. At high field, only AB oscillation exists, which can be seen clearly from Fig. 4.40. Figure 4.40 is Fourier spectrum of oscillations in different magnetic field ranges with a span of 400 G so as to contain a sufficient number of oscillations.

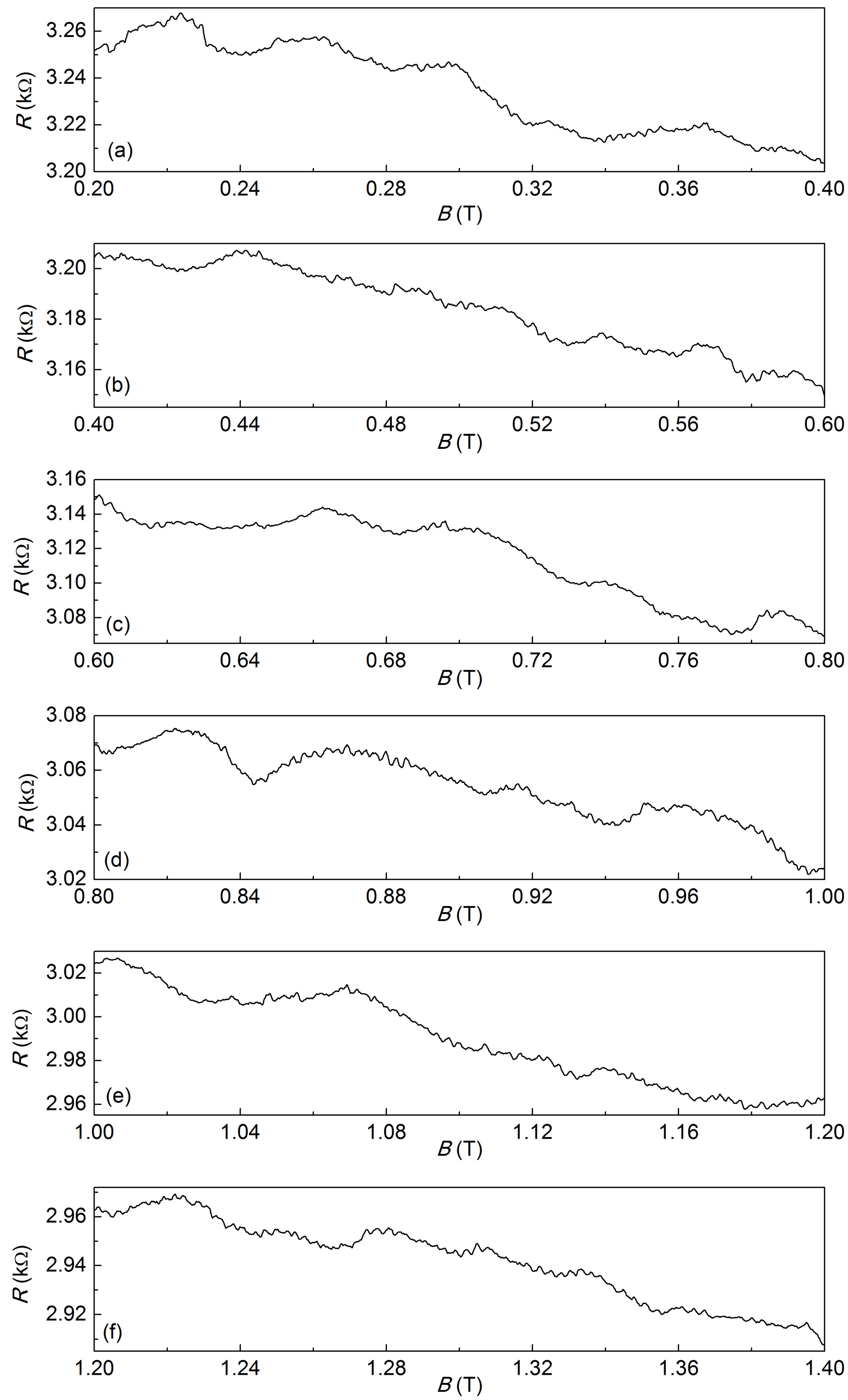

Figure 4.37: AB oscillations in a 5×5 AB ring array at magnetic fields from 0.2 T to 1.4 T.

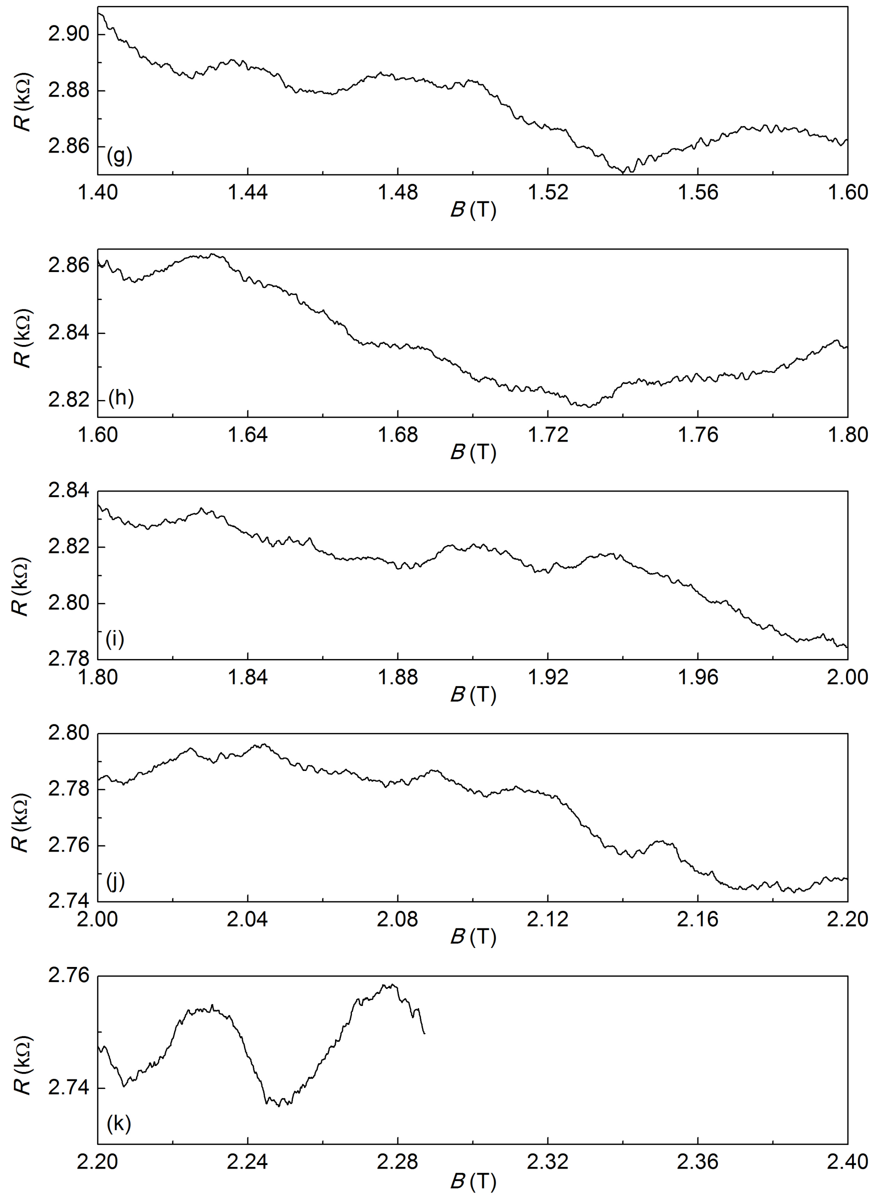

Figure 4.38: AB oscillations in a 5×5 AB ring array at magnetic fields from 1.4 T to 2.3 T.

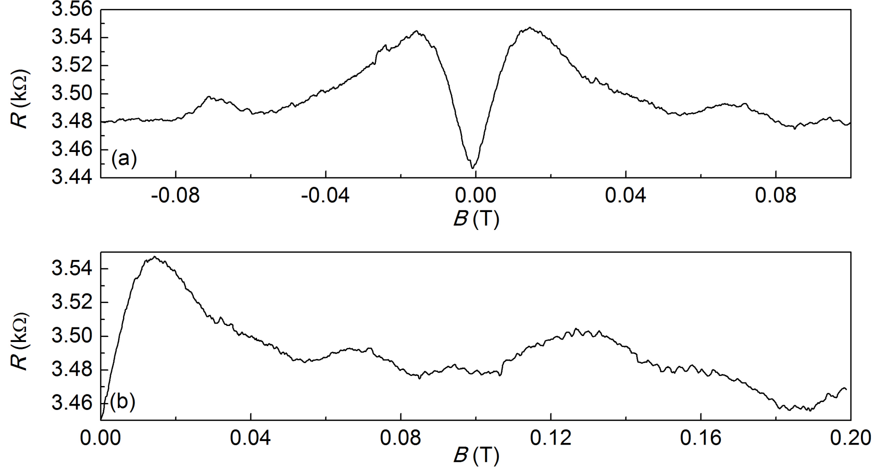

Figure 4.39: AAS and AB oscillations in a 5×5 AB ring array at magnetic fields from -0.1 T to 0.2 T. AAS oscillations are stronger in panel (a) than panel (b).

As shown in Fig. 4.39(a), the array yields a strong weak antilocalization (WAL) positive magnetoresistance background, on which interference oscillations ride. To enhance the visibility of the low magnetic field AAS oscillations, we remove the magnetoresistance background for further discussion of AAS oscillations.

Figure 4.41(a) focuses on R(B) versus B at low magnetic field, spanning ±200 G. Upon removal of the WAL background in Fig. 4.41(b), AAS oscillations clearly appear for $B <$ 50 G. The Fourier spectrum corresponding to Fig. 4.41(b) is contained in Fig. 4.41(c). In the spectrum the AB oscillations produce a maximum at $1/B = 360$ T^{-1}, corresponding to periodicity $\Delta B_{AB} = 27.8$ G, and the AAS oscillations produce a maximum at $1/B = 750$ T^{-1}, corresponding to periodicity $\Delta B_{AAS} = 13.3$ G. The Fourier transform confirms that $\Delta B_{AAS} \approx \frac{1}{2}\Delta B_{AB}$ and yields values close to geometrical expectations, hence corroborating the existence of AB h/e and AAS $h/2e$ oscillations in the range ±200 G.

Figure 4.40 depicts Fourier spectra illustrating the decay of AAS oscillations with increasing B, caused by time-reversal symmetry breaking and quantitatively described by the shortening of L_C with increasing B ($L_C = \sqrt{l_\phi^{-2} + L_B^{-2}}$ in chapter 1). It is noticeable that whereas the AAS oscillation amplitude decays with increasing B, the AB oscillations maintain approximately constant amplitude. Figure 4.38 also demonstrated that AB oscillations survive essentially unaffected at higher B. Figure 4.42(a) depicts the AAS (h/2e) Fourier amplitude versus B as obtained from Fig. 4.40. The coordinates contains the height of the $h/2e$ Fourier component, while the B axis corresponds to the center value B of the Fourier transform spans. Thus, the first data point lies at $B = 0.01$ T, and the subsequent data points at 0.04 T, 0.08 T, 0.12 T and 0.16 T. Figure 4.42(a) clearly shows the decay of the AAS oscillations amplitude with increasing B. We note that oscillations periodic in $h/2e$ can in principle also occur as higher harmonics of AB oscillations. However, AB oscillations contribution in

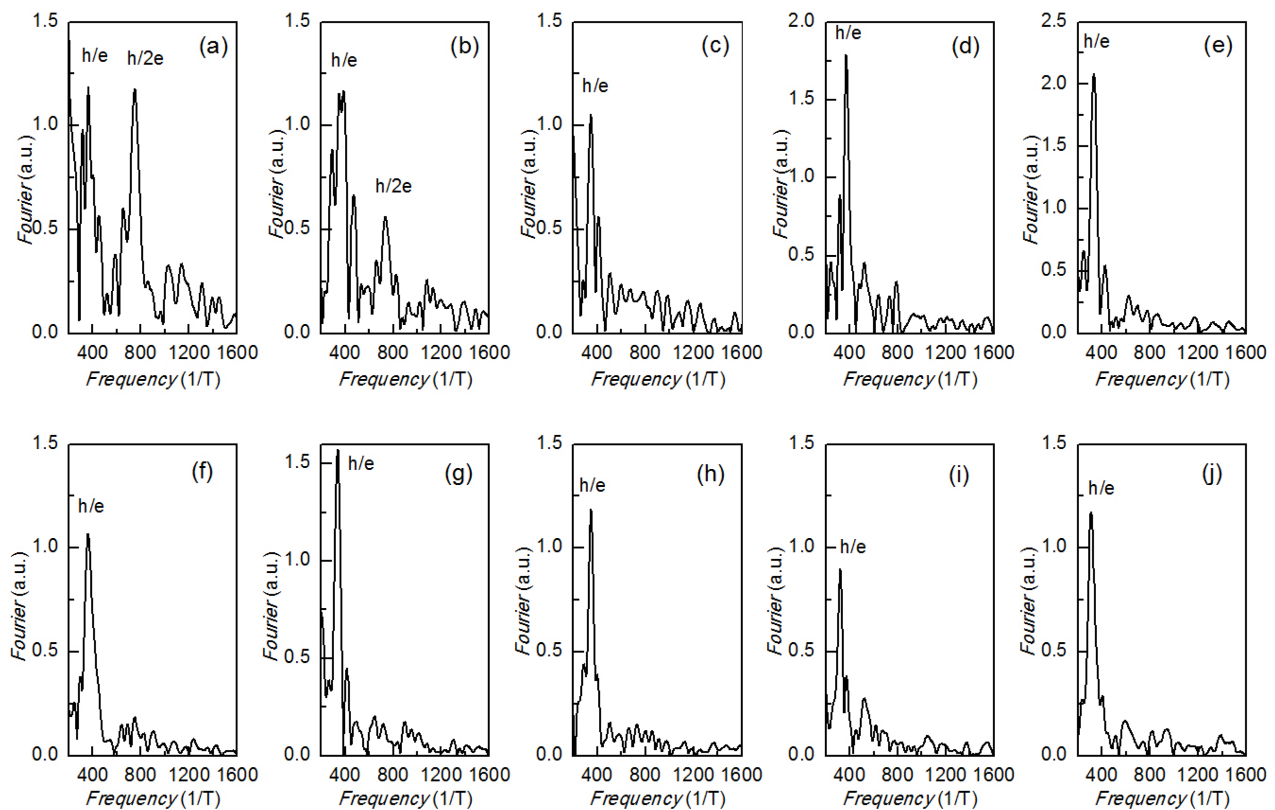

Figure 4.40: Fourier transformation of AAS and AB oscillations in the interferometer array. Fourier spectrum in (a) is for magnetic field -0.02 T to 0.02 T, (b) 0.02 T to 0.06 T, (c) 0.06 T to 0.10 T, (d) 0.10 T to 0.14 T, (e) 0.14 T to 0.18 T, (f) 0.32 T to 0.36 T, (g) 0.84 T to 0.88 T, (h) 1.32 T to 1.36 T, (i) 1.80 T to 1.84 T and (j) 2.16 T and 2.20 T. As the magnetic field increases, the AAS oscillation component in Fourier spectrum becomes less, and invisible finally, however, the AB oscillation component is almost unchanged.

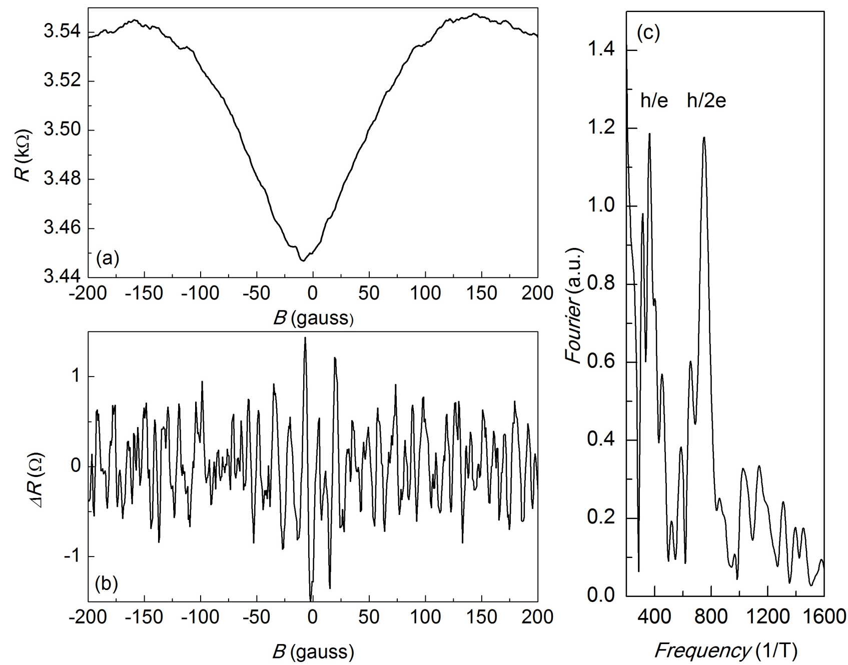

Figure 4.41: (a) R(B) versus B at low B spanning ± 200 G; (b) After removing the WAL positive magnetoresistance background from (a), AAS and AB oscillations clearly appear. (c) Fourier transform of the data in (a) with two peaks clearly marked out: the h/e peak corresponding to AB oscillation and the h/2e peak corresponding to AAS oscillation.

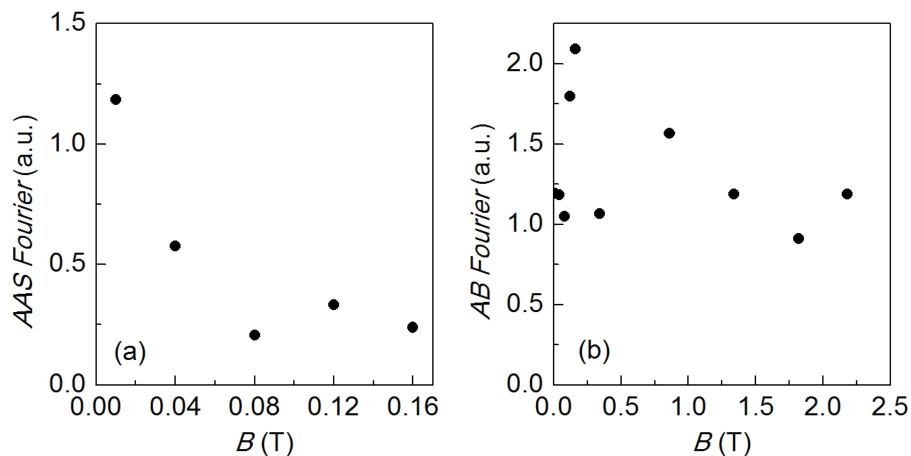

Figure 4.42: Fourier component amplitudes (arbitrary units) versus B ($B-$values determined as explained in the text). (a) AAS (h/2e) Fourier component versus B, illustrating the decay of AAS oscillations with increasing B. (b) AB (h/e) Fourier component versus B, illustrating the lack of monotonic decay of AB oscillations with increasing B.

ring array will be small due to ensemble averaging. The observed decay with increasing B of the $h/2e$ component also strongly favors its identification as an AAS contribution. Using the same method, Fig. 4.42(b) depicts the height of AB (h/e) Fourier component versus B over a wider range of B, demonstrating that although AB oscillation amplitude varies due to local magnetic flux, no monotonic decay with increasing B is apparent. The different behavior of AAS and AB oscillation originates in the different symmetries, respectively temporal and spatial which they are sensitive to.

4.5.3 Magnetic dephasing length $L_B(B)$ and time-reversal symmetry breaking

At low temperatures T in solid-state systems, many factors can contribute to reduction of oscillation amplitudes, such as decoherence by fluctuations in the electromagnetic background (Nyquist decoherence) [51, 68, 69, 70], by particle leakage from the quantum system (dwell-time-limited decoherence) [68, 71], and by energy smearing from excitation exceeding the Thouless energy [48]. These mechanisms lead to irreversible dephasing, referred to as decoherence [72], and determine the phase coherence length l_ϕ, defined as the distance electrons travel before their quantum phase is randomized by inelastic scattering processes. The characteristic length over which time-reversed partial waves dephase in B due to the accumulated AB phase is a magnetic length L_B, which can be estimated from the quantum interference effects of the AB phase. In an unconfined system, a closed trajectory will accumulate a unity quantum phase if the trajectory encloses a magnetic flux $\hbar/e$. Defining the area enclosed by the trajectory as L_B^2, we find $L_B = l_m \equiv \sqrt{\hbar/(eB)}$. L_B is the characteristic length for breaking of time-reversal symmetry and enters in expressions of decoherence analogously to l_ϕ. The corresponding decoherence and dephasing rates (inverse times) can be added according to Matthiessen's rule [67, 73, 74]. In a diffusive approach, l_ϕ and L_B are related to the phase coherence time τ_ϕ and magnetic dephasing time τ_B respectively by $l_\phi = \sqrt{D\tau_\phi}$ and $L_B = \sqrt{D\tau_B}$, where D is the diffusion coefficient. The effective coherence length L_C combining both effects hence is obtained as

$$L_C = \left(l_\phi^{-2} + L_B^{-2}\right)^{-\frac{1}{2}} \tag{4.7}$$

The expression $L_B = \sqrt{\hbar/(eB)}$ only applies to unconfined systems, and Eq. 4.7 supposes diffusive transport. Expressions for L_B have been derived extending the range of applicability to confined [73], and ballistic [75, 76] systems, as explained below. Yet, hitherto the expressions have not been put to a direct comparative experimental test. The work below demonstrates the applicability of the expressions for L_B to quantum transport at low T by using the intensity of AAS oscillation. A strong correlation between the Fourier amplitude of the AAS oscillations and a length L_B is observed. By fitting the Fourier amplitude of AAS oscillations, we experimentally derive values for the mesoscopic time-reversal symmetry breaking length L_B as function of B.

Due to spin-orbit interaction in the InGaAs/InAlAs heterostructure, a weak antilocalization (WAL) [64, 70, 74, 77, 78] background in the magnetotransport is also observed.

The magnetic dephasing length $L_B(B)$ assumes different forms depending on the relative values of $l_m \equiv \sqrt{\hbar/(eB)}$, l_e and w. As mentioned, in an unconfined system without impediment to flux accumulation over a closed path and where necessarily $l_m \ll w$ and $l_e \ll w$, we have the unconfined diffusive expression for $L_B(B)$

$$L_B = l_m \tag{4.8}$$

Still in the diffusive regime ($l_e < w$) and with diffusive boundary scattering, yet in a narrow wire and at low B with $l_m > w$, such that boundary conditions at the wire edges modify the Landau level states, we have [73]

$$L_B = \sqrt{3}l_m^2/w \tag{4.9}$$

In the diffusive regime but where $l_m \simeq w$, a crossover expression [79] can be applied,

$$L_B = \sqrt{l_m^2 + 3l_m^4/w^2} \tag{4.10}$$

In the ballistic regime where $l_e \geq w$, and at low B limited by $l_m > \sqrt{wl_e}$, we have an expression taking flux cancellation into account [75, 76]

$$L_B = l_m\sqrt{\mathrm{C}_1 l_m^2 l_e/w^3} \tag{4.11}$$

Still in the ballistic regime ($l_e \geq w$), and at intermediate B such that $w < l_m < \sqrt{wl_e}$, we have a crossover expression [75, 76]

$$L_B = l_m\sqrt{\mathrm{C}_1 l_m^2 l_e/w^3 + \mathrm{C}_2 l_e^2/w^2} \tag{4.12}$$

C_1 and C_2 are numerical constants with values depending on whether the boundary scattering at wire edges is specular or diffusive. Specular boundary scattering is expected in wires fabricated from the $In_{0.64}Ga_{0.36}As/In_{0.45}Al_{0.55}As$ heterostructure due to the presence of a depletion layer at the wire edge. For specular boundary scattering in a 2DES, $\mathrm{C}_1 = 4.75$ and $\mathrm{C}_2 = 2.4$. The ring array, with $w \simeq 100$ nm, and $l_e = 1.54$ μm, should satisfy the ballistic condition.

With knowledge of $L_B(B)$ and l_ϕ, Eq. 4.7 provides the effective coherence length $L_C(B)$. In order to determine which model (Eq. 4.8 - Eq. 4.12) fits the experimental data best, we have to introduce a method to map the AAS oscillation amplitude to the coherence length L_C. For a quantum-coherent interferometer array [64, 65], an expression more complex than an exponential decay with characteristic length L_C is appropriate as

$$A = \alpha(L_C/L)(1 - Tanh(L/L_C)) \tag{4.13}$$

where A is amplitude is AAS oscillation, α is a constant factor, and $L = \pi r$. At low B, we can assume $L_B \gg l_\phi$, such that $L_C \approx l_\phi = 3$ μm. We thus use the data point at

the lowest $B = 100$ G in Fig. 4.42(a) to calibrate α using $L_C = 3$ μm in Eq. 4.13. For the remaining 4 points, the value of $L_C(B)$ can then be obtained, and hence the value of $L_B(B)$ experimentally determined using Eq. 4.7. The results are depicted in Fig. 4.43. The calibration point at $B = 100$ G lies off the graph since for this data point L_B is assumed very long; a guideline was used to connect this point to the remaining data. Figure 4.43 also plots values of L_B calculated from Eq. 4.8 - Eq. 4.12. The model described by Eq. 4.12 provides the best match to the experimental values of L_B.

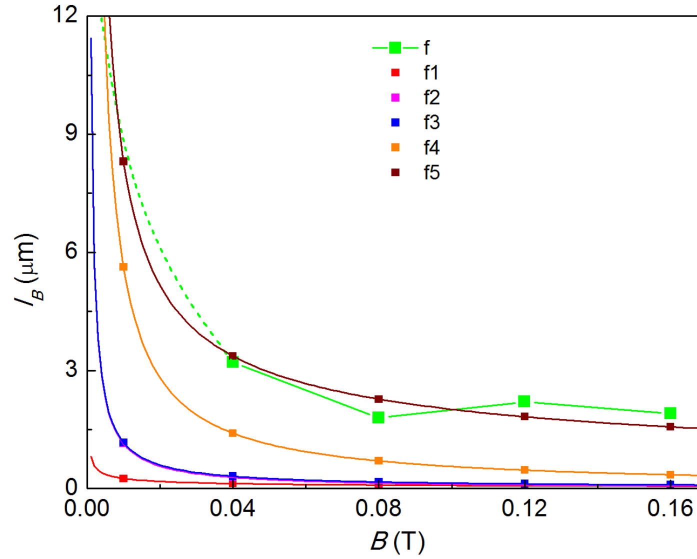

Figure 4.43: Calculated values of l_B according to different models, f1 is Eq. 4.8, f2 is Eq. 4.9, f3 is Eq. 4.10, f4 is Eq. 4.11, f5 is Eq. 4.12 (curves for Eq.4.9 and Eq.4.10 mostly overlap for the present paramters and cannot be distinguished on the graph). The data labeled with f shows the values calculated from experimental data according to Eq. 4.13. Details about the method are explained in the text.

The result that the calculated experimental data for $L_B(B)$ follows Eq. 4.12, is reasonable. The system is confined to a wire of width w and is in ballistic regime, with $l_e > w$. Hence Eq. 4.8, 4.9 and 4.10 are not expected to be suitable, and the data indeed bears out this observation. The condition $l_m > \sqrt{wl_e}$ for Eq. 4.11 implies that $B < 38$ G. In Fig. 4.43, B exceeds 38 G, and hence Eq. 4.11 is not expected to fit the data except at the lowest B where no independent data is available. Using the condition $w < l_m < \sqrt{wl_e}$, we obtain 38 G $<$ B $<$ 660 G. The condition implies that Eq. 4.12 is expected to match the data in this range of B. The experiment bears out that in fact Eq. 4.12 provides a good description of $L_B(B)$ not only in this range, but beyond $B = 660$ G. We also note that at the higher B, C_1 can be set to 0. However, since our data is obtained from -200 G to 1800 G, a range that includes low B, the full crossover expression given by Eq. 4.12 provides a prediction for $L_B(B)$ valid over a wide range of B in our ballistic system.

A single ring in the array has a circumference about 4 μm. We can thus expect that when $L_B(B)$ is smaller than this value, the AAS oscillation amplitude should decrease significantly. The data in Fig. 4.43 is consistent with this expectation, as the Fourier transform height of the AAS oscillations almost merges into the background for $L_B(B) \leq 3$ μm. We note that an increase in AAS oscillation amplitude can be achieved by excluding the local magnetic flux from the interferometer arms, although an experimental realization of this approach will prove challenging. Alternatively, narrowing w will yield a more practical avenue to increase the AAS oscillation amplitude, as in Eqs. 4.9-4.12 L_B will lengthen with narrowing w. Insight in this relation follows from considering that if a closed path is constrained to w along a transverse direction in a wire, acquiring a given AB phase will require that the partial wave travel over $\sim l_m^2/w$ in the longitudinal direction, which becomes the effective free length for AB phase accumulation, or hence the effective magnetic length and time-reversal symmetry breaking length. The lengthening of L_B with narrowing w hence has a geometrical origin, in a delay of accumulated local magnetic flux to higher B. The AB oscillations are not similarly affected by the local magnetic flux, as the AB interference does not rely on time-reversal symmetry and hence remains unaffected by L_B.

4.5.4 Phase coherence length in an AB ring array

The phase coherence length l_ϕ is defined as the distance electrons travel before their quantum phase is randomized by inelastic scattering processes, and, at low T, l_ϕ can reach a few μm [51]. The amplitude A of the AB oscillations observed in an electron interferometer exponentially decays [52, 53] with the electron path length l, as:

$$A(l) = \mathrm{A}_0 \exp(-l/l_\phi) \tag{4.14}$$

where A_0 is a prefactor dependent on energy smearing via the thermal energy k_BT (where k_B is the Boltzmann constant) and via voltage or current bias. For an AB ring, the h/e oscillation period corresponds to a path length $l = \pi r$ and is the strongest component in the frequency spectrum in $R(B)$. A weaker component at $h/2e$ often exists, corresponding to a path length $l = 2\pi r$. We can ignore the AAS oscillation when the magnetic field is high enough, as the following data was obtained above 0.12 T where the AAS oscillation is pretty weak from the above analysis. Rarely a component at $h/3e$ is observed, corresponding to a path length $l = 3\pi r$. From the experimentally observed amplitudes in the frequency spectrum and using the correspondence between the h/ne mode and the path length $l = n\pi r$, Eq. 4.14 allows l_ϕ to be deduced [53]. The mobility mean free path forms another important length scale, limited by elastic momentum scattering processes, and defined as $l_\mathrm{e} = v_\mathrm{F}\tau_e$, where v_F is the Fermi velocity, $\tau_e = \mu m_e^*/e$ is the momentum relaxation time derived from the mobility μ, and m_e^* represents the electron effective mass ($m_e^* = 0.035 m_e$ at the Γ-point in our system, where m_e represents the free-electron mass). Our rings are in the quasi-ballistic regime, where l_e approximately equals the path length πr, and ballistic, rather than diffusive, expressions are used to describe mesoscopic transport phenomena.

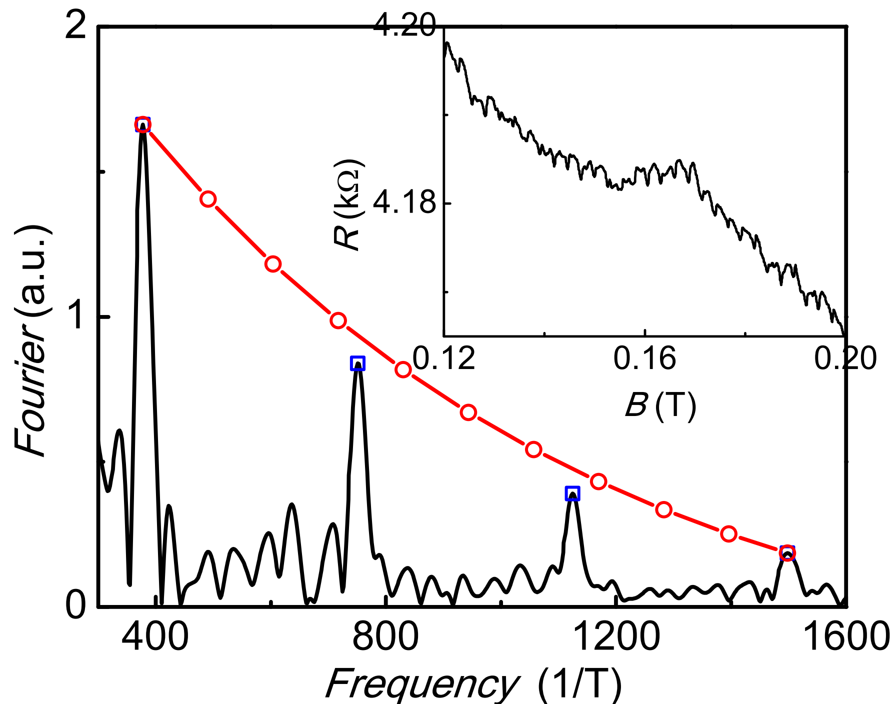

Figure 4.44: The fit to Eq. 4.14 to extract phase coherence length l_ϕ. The inset shows the Aharonov-Bohm magnetoresistance oscillations used for the Fourier transform, itself depicted as the black solid line in the main graph. The red line with open circles depicts the fit to Eq. 4.14.

The Fourier spectrum of $R(B)$ can be used to deduce l_ϕ by applying Eq. 4.14, as outlined in the introduction. Figure 4.44 demonstrates the process, yielding the value $l_\phi = 3$ μm at $T = 0.4$ K. The low excitation current ($I = 20$ nA rms) and low T used to obtain the data for the fit to Eq. 4.14 ensures that distortion of the value of l_ϕ by energy smearing is minimized. The value $l_\phi > l_e = 1.7$ μm shows that at low T inelastic phase breaking scattering events will indeed be rarer than elastic momentum scattering events. We note that phase coherence is in our samples mostly maintained over a length longer than πr, explaining the observation of a strong AB effect.

4.6 Mounting LED to improve device performance

Interference oscillations are very strong in our measurements, even at 1.2 K. But at the beginning of the experiments, the quantum interference usually decayed away when T reaches above 1.0 K. We improved the device performance by mounting an LED to in proximity to the sample. Figure 4.45 shows the device "R082410" mounted with an LED.

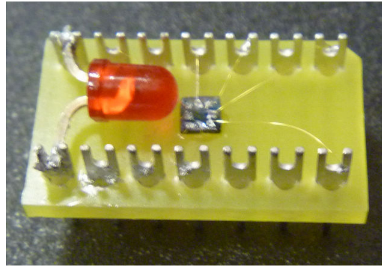

Figure 4.45: An LED is mounted on the device “R082410”.

This technique turns out very useful for our heterostructure (n-type). The LED was tested to work successfully from room temperature to 4.2 K before it was mounted to the real device, although I didn’t test it below 4.2 K. According to later results, this kind of LED works well below 4.2 K and above 0.4 K. Before using a particular type of LED, a test is necessary, as many types of LED won’t work even at liquid nitrogen temperature.

When the system’s temperature cools down to the target point, we turn on the LED at a current of 10 μA (this value may vary for a different type of LED) for several seconds. The device’s resistance decreases as photons excite more carriers in the device. When the LED is turned off, device’s resistance will increase and after a while it will stabilize for measurements. This process can be repeated several times if you are not satisfied about the results and not sure about the quality of the device. However, if measurements need to be compared with each other, LED use between different measurements is not recommended, as the state of the device will be changed by use of the LED.

Chapter 5

Hole system in p-type GaAs/AlGaAs

The materials used in this chapter are p-type GaAs/AlGaAs heterostructure (L. Pfeiffer, Princeton), a Si-doped asymmetric quantum well in GaAs/$Al_{0.35}Ga_{0.65}As$ (named M423) and a C-doped symmetric quantum well in GaAs/$Al_{0.24}Ga_{0.76}As$ (named 94121). They have much higher mobility than the n-type material we investigated before. We focused on studying magnetoresistance of thin wires to explore antilocalization, quantum coherence and spin coherence in these p-type GaAs/AlGaAs heterostructure.

5.1 M423 and 94121 hole systems

The heterostructure have a 2D hole system (2DHS) beneath the surface instead of a 2DES, and the 2DHS layer is located much deeper than the 2DES that we investigated previously. This small change requires corresponding adjustments in fabrication processes as described later.

Figure 5.1 shows the schematic structure of M423, the Si-doped p-type GaAs/$Al_{0.35}Ga_{0.65}As$ heterostructure, with the surface orientation (311)A. The 2DHS layer is located 100 nm beneath the surface. At 0.4 K, the 2DHS hole density is $p = 2.4 \times 10^{15}$ m^{-2}, the mobility in the direction $[01\bar{1}]$ is $\mu = 25$ m^2/Vs, mean free path is $l_e = 2.0$ μm. The quantum well is asymmetric.

Figure 5.2 shows the schematic structure of 94121, the C-doped p-type GaAs/$Al_{0.24}Ga_{0.76}As$ heterostructure with the surface direction orientation (001). The 2DHS is located 136 nm beneath the surface. The quantum well is symmetric. For such material, we can fabricate back or front gates to change its electronic transport properties by varying gate voltage in an appropriate range. Sometimes, even by barely fabricating a back gate without applying gate voltage, the electronic transport properties will be altered, and this is the case for us. We made several devices from 94121, however, only two of them will be discussed, one without

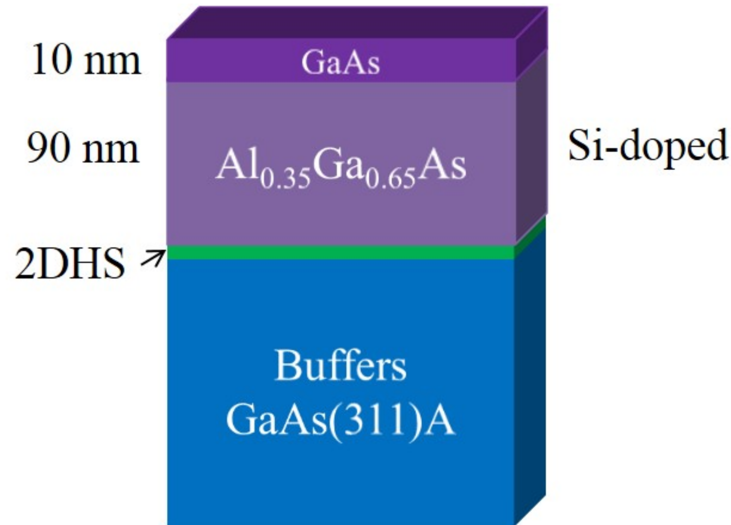

Figure 5.1: Schematic structure of M423 Si-doped p-type GaAs/$Al_{0.35}Ga_{0.65}$. The 2DHS layer is located 100 nm beneath the surface.

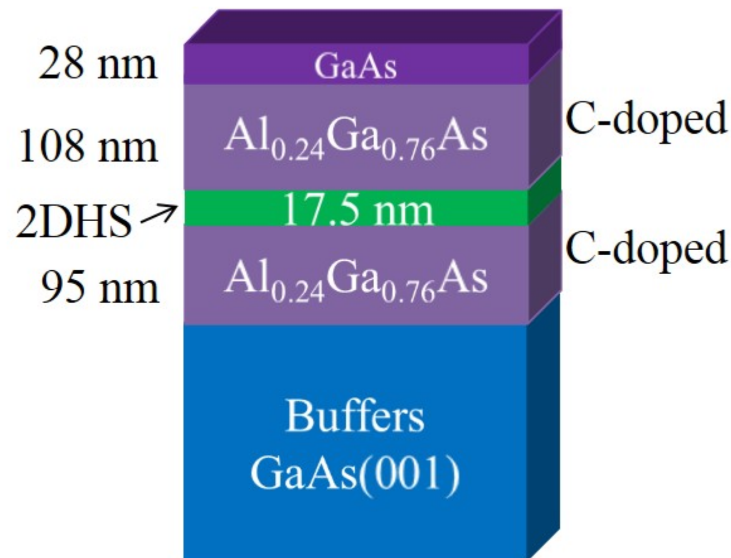

Figure 5.2: Schematic structure of 94121 C-doped p-type GaAs/$Al_{0.24}Ga_{0.76}As$. The 2DHS layer is located 136 nm beneath the surface.

back gate and one with back gate but without applying any gate voltage. At 0.4 K, for the device without back gate, the 2DHS hole density is $p = 14.5 \times 10^{14}$ m^{-2}, mobility is $\mu = 150$ m^2/Vs, mean free path is $l_e = 9.3$ μm; for the device with back gate, the 2DHS hole density is $p = 9.64 \times 10^{14}$ m^{-2}, mobility is $\mu = 130$ m^2/Vs, mean free path is $l_e = 6.6$ μm.

5.2 Pattern design and fabricated devices

Figure 5.3 shows the device made from material M423, as captured through an optical microscope. The base pattern is an L shaped Hall bar. A wires pattern is fabricated on one leg, the other is used to measure the electronic transport properties, the dimension of this Hall bar and a zoomed in view of the wires pattern is shown in Fig. 5.4. The width of this Hall bar is 80 μm, the separation of two legs on one side is 160 μm. During measurements, a magnetic field perpendicular to the 2DHS is applied, a constant low frequency AC current flows through the Hall bar. Lock-in amplifier techniques are used to pick up the voltage signals. This material has anisotropic properties, the mobility along direction $[\bar{2}33]$ is higher than direction$[01\bar{1}]$. Wires were fabricated along the high mobility direction $[\bar{2}33]$.

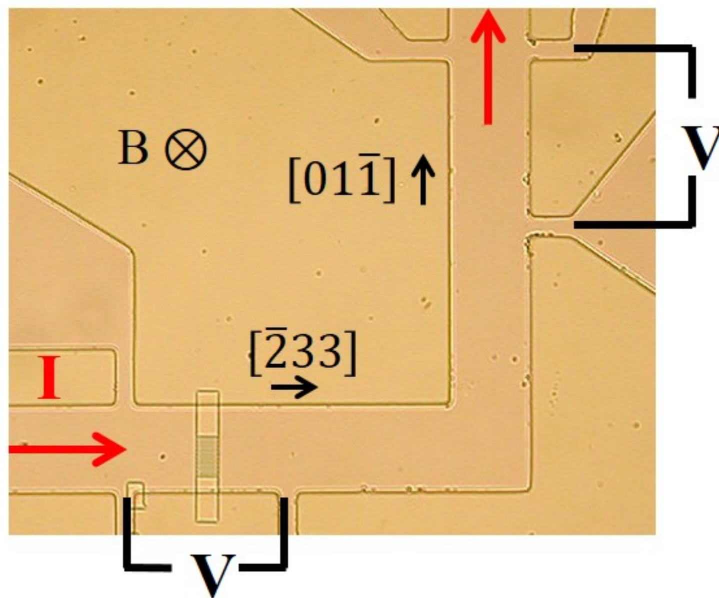

Figure 5.3: Optical microscope view of the device made from M423 and measurement configuration. The darker part is conducting, the light-colored parts are etched out by wet etching. A schematic measurement configuration and crystal directions are shown as well.

The wire pattern is a set of 10 parallel wires, each wire has designed width 0.7 μm and length 20 μm, the space between two neighbored wires is 2 μm. Figure 5.5 shows the

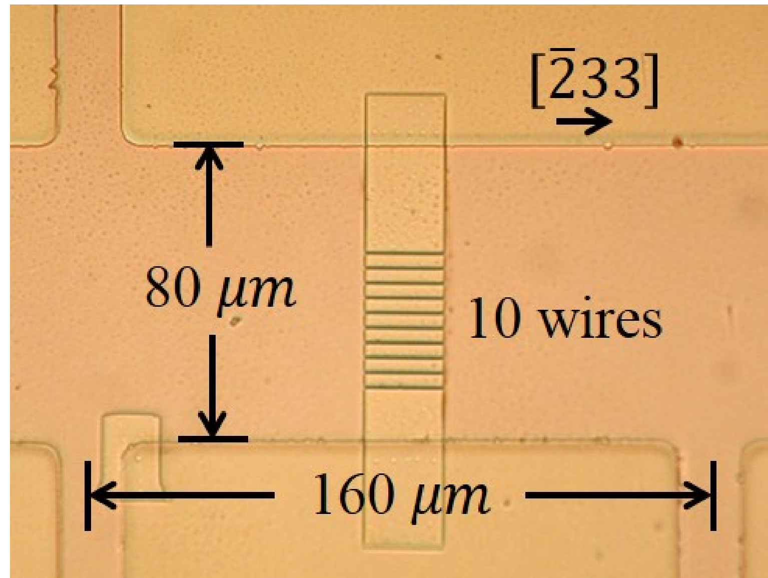

Figure 5.4: Optical microscope view of the wires patterned on the chip. The 10 parallel wires appear as 10 lines in this image as the resolution of the optical microscope is unsufficient.

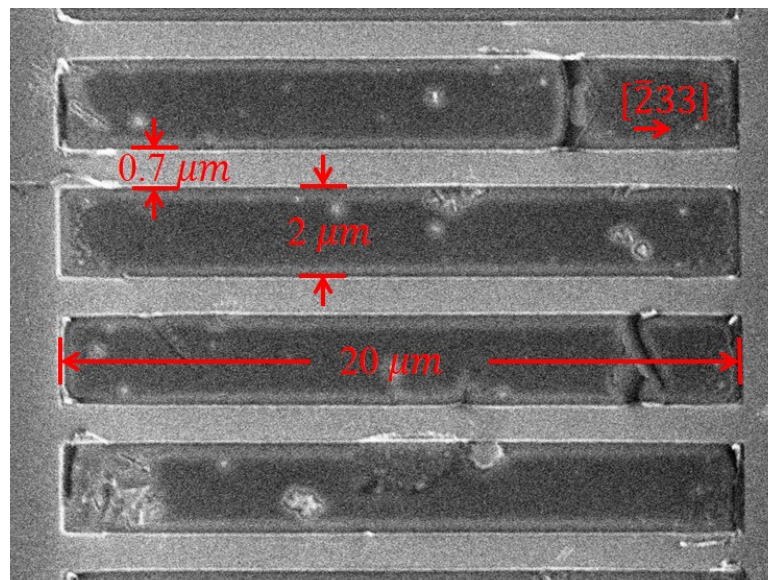

Figure 5.5: SEM view of part of the wire pattern with dimensions. The darker parts are etched out by ICP RIE, the light-colored part is conducting.

SEM picture of those wires, the darker parts are etched out by ICP RIE, the light-colored part is conducting. As the ICP RIE has a high fabrication accuracy, we can take the real dimension of those wires as designed. However, for such devices, the thin conducting part has significant depletion layers on its edges, the real conducting width has to be calculated through transport measurement.

The photolithography (AZ5206 was used) process for those materials is the same as before. However, the e-beam lithography (ZEP was used instead of PMMA) process needs to be altered slightly as the quantum well is deeper and ICP RIE requires a longer time. Usually, we try to minimize the time that a sample is exposed to ion plasma, with the dry etching depth just reaching the quantum well. The RIE time is 75 s for M423 and 120 s for 94121.

As those materials have high mobility, weak localization is suppressed. Thus we intended to introduce impurities artificially by designing antidots in a plain wire. Figure 5.6 shows a device made from material 94121 p-type C-doped GaAs/$Al_{0.24}Ga_{0.76}As$. This device has two wires with width 2 μm and 1.6 μm respectively. Several antidots were fabricated in each wire. The dimensions of the Hall bar and the measurement configuration are shown as well. Figure 5.7 shows an SEM image of the narrower wire with width 1.6 μm of this device. The two wires have length 6 μm, each antidot's diameter is 0.4 μm.

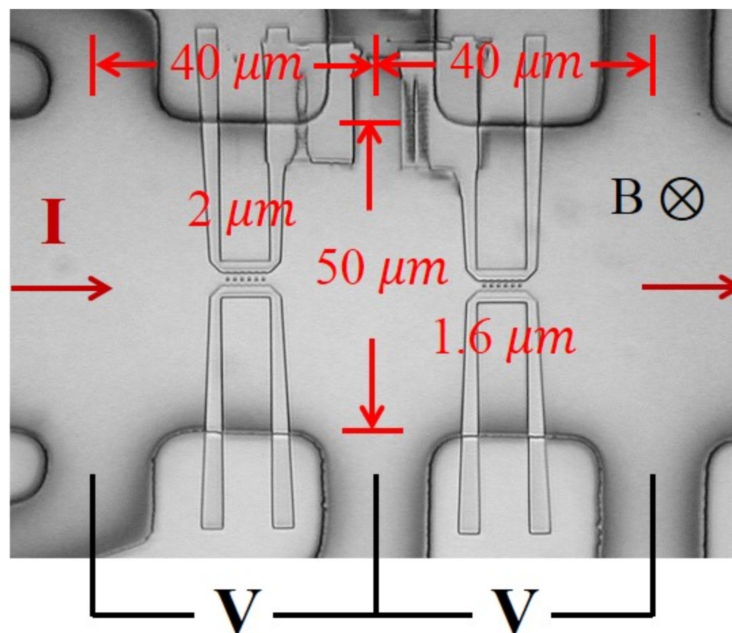

Figure 5.6: Optical microscope view of the device made from 94121 and measurement configuration.

Figure 5.8 shows another design for the material 94121, with details stated in the caption. This pattern was fabricated on an L shaped Hall bar as Fig 5.3. An optical microscope view

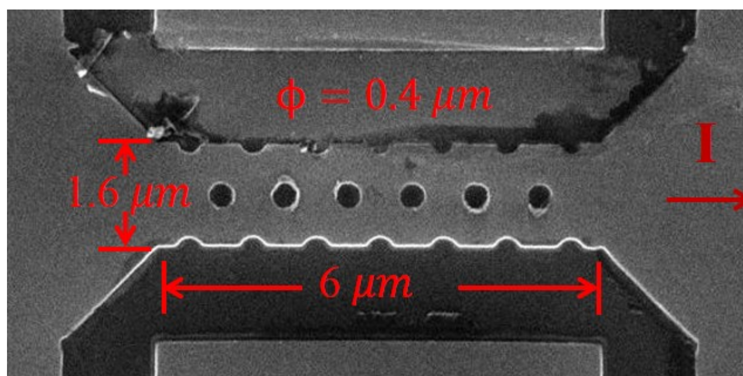

Figure 5.7: SEM view of the narrower wire on the 94121 device.

of the pattern after e-beam lithography is shown in Fig 5.9. Figure 5.10 shows the SEM view of this antidot array. This device is used to study commensurability oscillation.

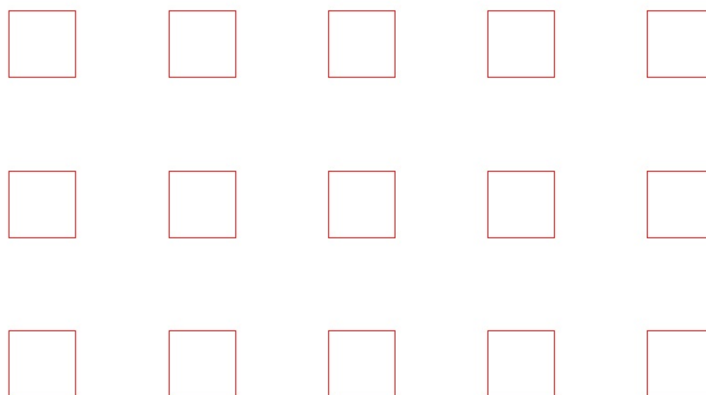

Figure 5.8: A design of antidot array, each square is an antidot. The side length of each square if 0.5 μm, the spatial periodicity of this antidot array is 1.2 μm, the separation between antidot is 0.7 μm. The whole design can cover more than 160 μm $\times$ 80 μm area, this view is part of the whole pattern.

5.3 Results and discussion

We investigated not only the quasi-one-dimensional (Q1D) hole wires, but also a bare Hall bar for antilocalization.

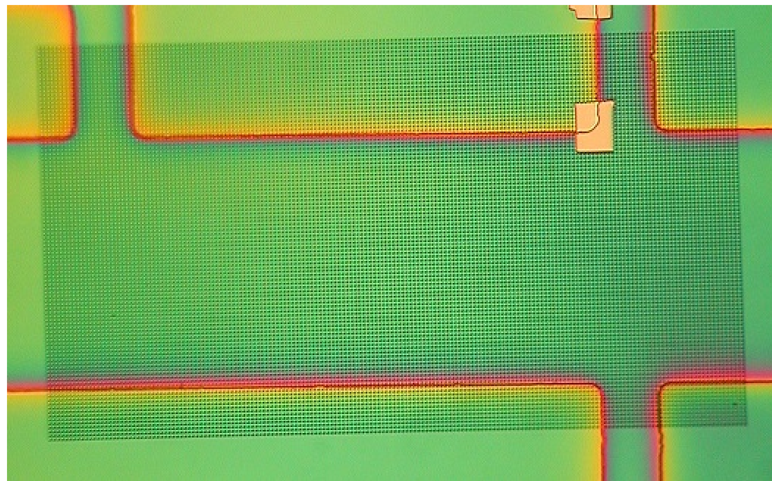

Figure 5.9: Optical microscope view of the pattern in Fig. 5.8 on a Hall bar after e-beam lithography.

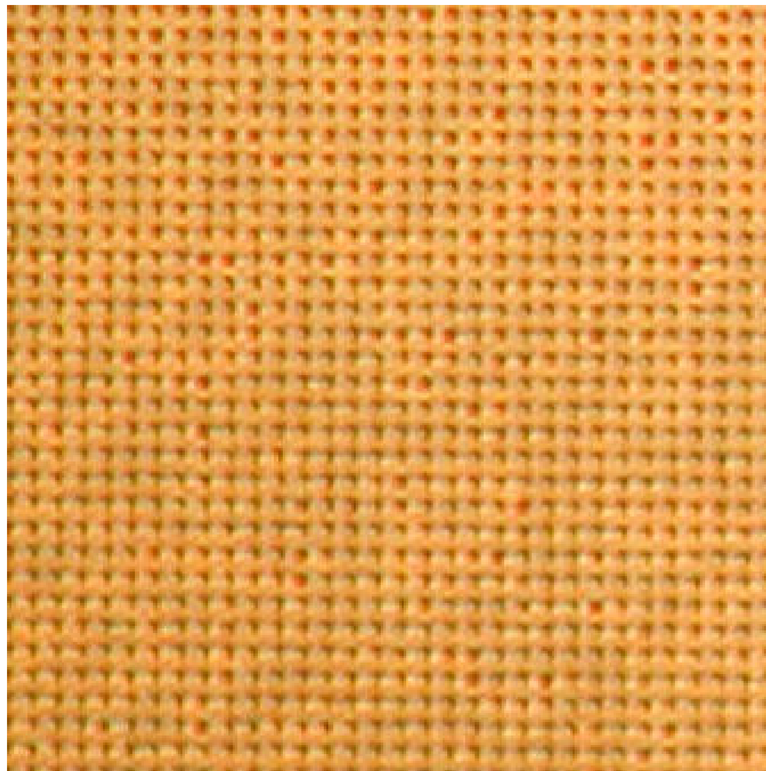

Figure 5.10: SEM view of the antidot array, the pits are the antidots. As stated in Fig. 5.8, each antidot has a size of 0.5 μm $\times$ 0.5 μm, the spatial periodicity of this antidot array is 1.2 μm.

5.3.1 Hall bar and wires on material M423

The material M423 has an asymmetric quantum well with an approximately triangular component potential. Previous research [80][add more] indicates that spin-orbit interaction (SOI) is strong in p-type GaAs heterostructures. The heavy hole subband splits into two subbands even without external magnetic field in such situation. Low field Shubnikov-de Haas (SbdH) oscillation measurements gave this expected results [81, 82, 83, 84, 85, 86]. Figure 5.11 shows the SbdH oscillation of a Hall bar along direction $[01\bar{1}]$ at 0.4 K. It has slightly different characters compared to a general SbdH oscillation, as beating is present at low magnetic field. The oscillation belows 3 T implies there is more than one frequency, indicating that this is an inversion asymmetric system with unequal population in SOI-split subbands.

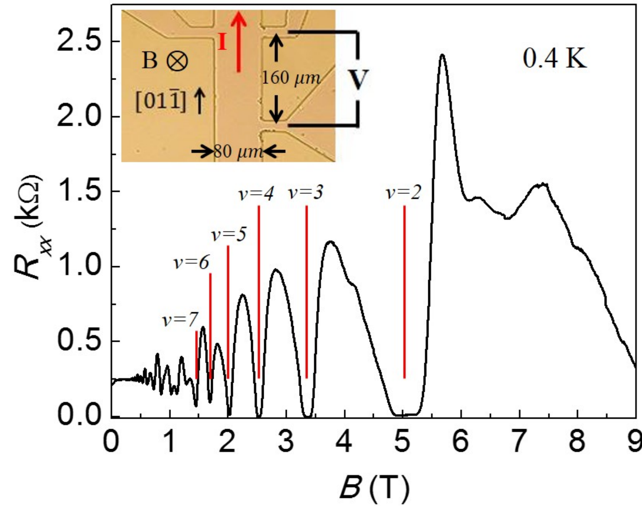

Figure 5.11: Shubnikov-de Haas oscillations on a Hall bar on material M423 along direction $[01\bar{1}]$ at 0.4 K. The inset graph shows the measurement setup, the red lines indicate the corresponding filling factors.

Figure 5.12 shows SbdH oscillations on a Hall bar along direction $[01\bar{1}]$ and on wires along direction $[\bar{2}33]$, below 2 T at 0.4 K. Although mobilities along the two directions have different values, SbdH oscillation has similar behavior and same filling factors which are marked with $\nu = 7$ and $\nu = 6$. We can deduce carrier density (denoted as N) from SbdH oscillation. Carrier density can be expressed as

$$N = \frac{e}{h(\Delta\frac{1}{B})} \tag{5.1}$$

where $\Delta\frac{1}{B}$ is the periodicity in $\frac{1}{B}$ of SbdH oscillations. In order to get $\Delta\frac{1}{B}$, we need to do

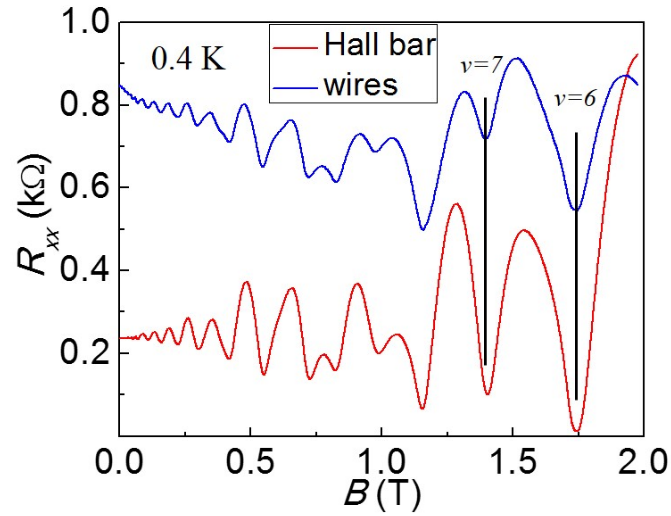

Figure 5.12: Shubnikov-de Haas oscillations of a Hall bar on material M423 along direction $[01\bar{1}]$ and on wires along direction $[\bar{2}33]$ below 2 T at 0.4 K.

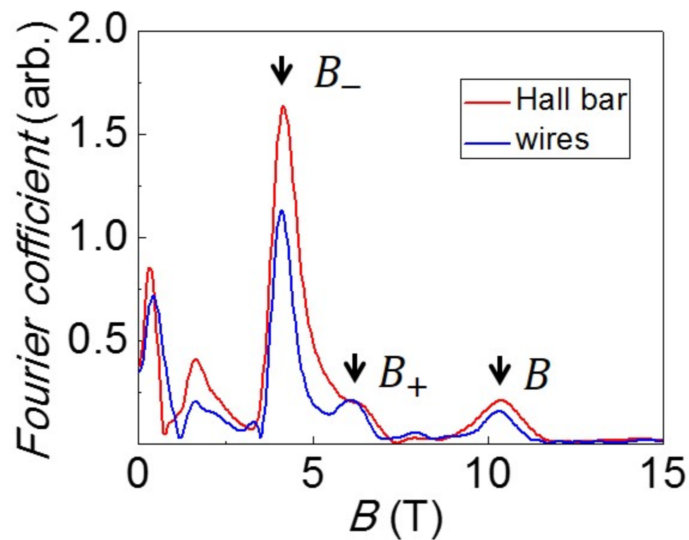

Figure 5.13: Fourier transform of the SbdH oscillations in Fig. 5.12.

a Fourier transform with B inversed to $\frac{1}{B}$. The result is showed in Fig. 5.13. Three maxima are marked as B_-, B_+ and B to indicate the SbdH oscillation frequency for the subband with spin-down holes, spin-up holes and degenerate holes respectively. We can get the densities for the spin-split subbands as $N_- = 1.00 \times 10^{15}$ 1/m^2 and $N_+ = 1.51 \times 10^{15}$ 1/m^2, and the total carrier density is $N = 2.49 \times 10^{15}$ 1/m^2. The total carrier density $N = N_- + N_+$ as expected, and it also matches the value obtained from Hall effect $N = 2.4 \times 10^{15}$ 1/m^2 in the previous section.

The strength of SIO can be quantified by assuming a cubic wave vector k dependence [80]

$$\Delta_{SO} = 2\beta k^3 \tag{5.2}$$

for heavy holes. The cubic Rashba coefficient β is [80]

$$\beta = \sqrt{\frac{2}{\pi}}\mu_h \frac{N(\tilde{N}_+ - \tilde{N}_-) + \Delta N(\tilde{N}_+ + \tilde{N}_-)}{6N^2 + 2\Delta N^2} \tag{5.3}$$

where $N = N_+ + N_-$, $\Delta N = N_+ - N_-$, $\tilde{N}_\pm = \sqrt{N \pm \Delta N}$, μ_h is the reciprocal effective mass of heavy hole $\mu_h = \frac{\hbar^2}{2m_h^*}$, $m_h^* = 0.34m_e$. Using the data obtained from SbdH oscillations, the cubic Rashba coefficient is $\beta = 1.78 \times 10^{-28}$ eVm^3. The splitting energy Δ_{SO} of the two subbands depends on wave vector k. The two subbands have different wave vectors, $k_\pm = \sqrt{4\pi N_\pm}$. for this calculation, we chose the wave vector k_- of the lower energy band and obtained $\Delta_{SO} = 0.50$ meV [86].

We also investigated the temperature dependence of antilocalization of the Hall bar and Q1D wires. Two methods are used to analyze the result, Hikami-Larkin-Nagaoka (HLN) theory and intersubband scattering hypothesis.

Figure 5.14 shows the temperature dependence of antilocalization in a Hall bar parallel to direction $[00\bar{1}]$. Temperature varies from 0.4 K to 3.0 K. When the temperature is low enough, we can see a significant negative magnetoresistance around zero magnetic field, almost disappearing at $T \approx 3$ T.

Figure 5.15 shows the metallic behavior of the material resistivity at low temperature, resistivity ρ is linear in T, which is consistent with the Coulombic interaction in this ballistic system [87, 88].

Briefly, HLN theory [89] describes weak localization in disordered electronic systems at low temperature. The simplified 2D HLN expression is

$$\begin{aligned}\Delta\sigma(B) = &-\alpha\frac{e^2}{\pi h}\left[\psi\left(\frac{1}{2} + \frac{H_e}{B}\right) - \psi\left(\frac{1}{2} + \frac{H_\phi + H_{SO}}{B}\right)\right.\\ &\left.+\frac{1}{2}\psi\left(\frac{1}{2} + \frac{H_\phi}{B}\right) - \frac{1}{2}\psi\left(\frac{1}{2} + \frac{H_\phi + 2H_{SO}}{B}\right)\right]\end{aligned} \tag{5.4}$$

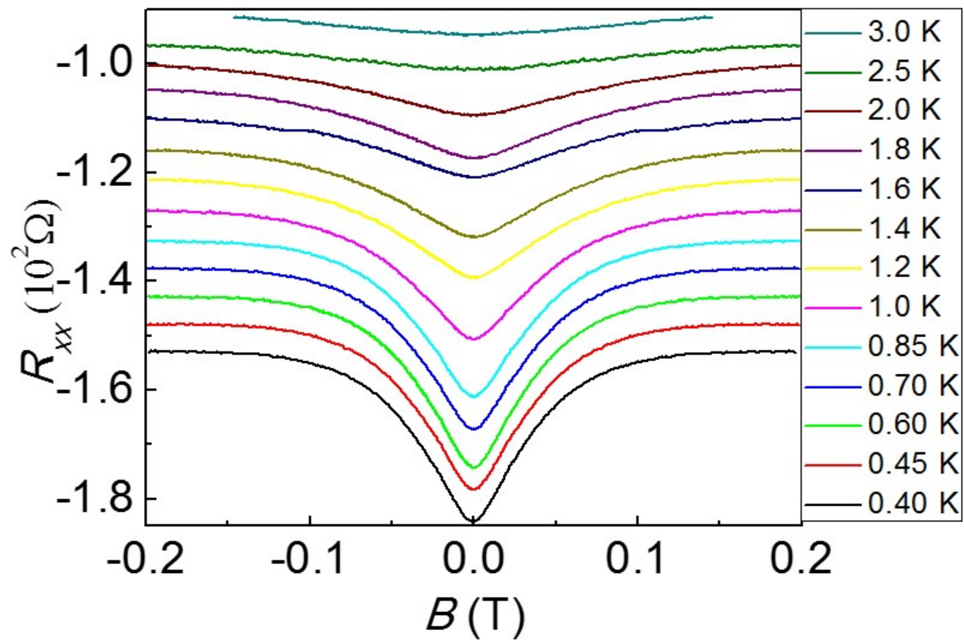

Figure 5.14: Temperature dependence of antilocalization of a Hall bar along $[00\bar{1}]$. Temperature varies from 0.4 K to 3.0 K, each curve is offset for clarity. The actual value of R_{xx} is about 200 Ω at $B = 0$.

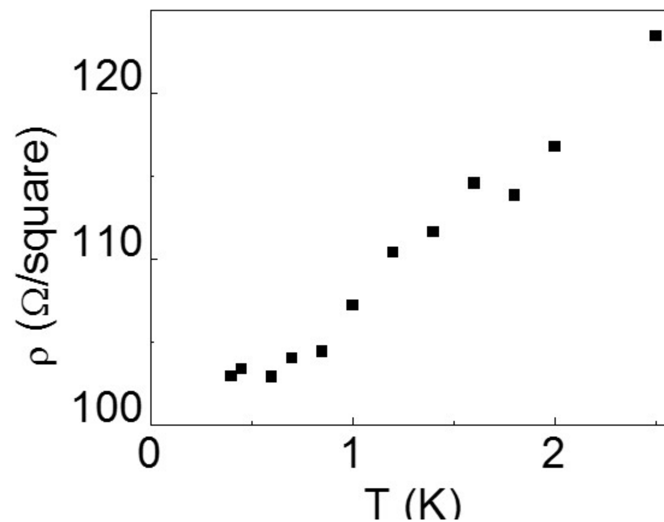

Figure 5.15: Metallic behavior of resistivity of M423 at low temperatures.

where the characteristic fields are related to the elastic scattering time τ_e, inelastic scattering time τ_ϕ and spin-orbit interaction dephasing time τ_{SO} as

$$H_e = \frac{\hbar}{4De\tau_e}, \quad H_\phi = \frac{\hbar}{4De\tau_\phi}, \quad H_{SO} = \frac{\hbar}{4De\tau_{SO}} \tag{5.5}$$

B is the external perpendicular magnetic field, $D = \frac{1}{2}v_F l_e$ is diffusion constant, ψ is digamma function.

Figure 5.16 shows one fit of HLN theory for the antilocalization data of a Hall bar at 0.4 K. We can obtain the corresponding characteristic times τ_{SO} and τ_ϕ from the fitting parameters. We performed the HLN fit for data at different temperatures, thus the temperature dependence of τ_{SO} and τ_ϕ can be derived. Those results are shown in Fig. 5.17. τ_{SO} is usually temperature independent, however, the phenomenon of temperature dependence of τ_{SO} in this material is not unique, a similar phenomenon was observed on InSb as well [90]. τ_ϕ follows rule $\tau_\phi \sim T^{-1}$, which is reasonable as this hole system is a Nyquist system. With those derived parameters, we can get the coherence length by multiplying the Fermi velocity $v_F = \frac{h}{m^*}\sqrt{\frac{N}{2\pi}} = 3.75\times10^4$ m/s (N is the total density without considering splitting) and the corresponding times. At 0.4 K $l_{SO} = 0.25$ μm and $l_\phi = 1.2$ μm, at 2.0 K $l_{SO} = 26$ nm and $l_\phi = 84$ nm.

Although the HLN gives good fitting and we have the above reasons to believe the result, we still take the result doubtful because of two reasons. τ_{SO} has a strong temperature dependence and phase coherence length is shorter than the mean free path. Further, that the theory is based on 1/2 spin electron systems and the data is from 3/2 spin hole systems.

We tried another method to analyze our data, this method assumes the magnetoresistance correction is caused by multiband inter- and intra-band scattering [86, 91]. From the previous SbdH oscillation analysis, the heavy hole band splits into two subbands with spin 3/2 and 1/2. According to this method, the longitudinal resistivity can be expressed as

$$\rho_{xx} = \frac{m^*}{e^2} Re\left[\frac{1}{TrN(K - i\omega_c I)^{-1}}\right] \tag{5.6}$$

where $I = \begin{pmatrix} 1 & 0 \\ 0 & 1 \end{pmatrix}$, $N = \begin{pmatrix} N_1 & \sqrt{N_1N_2} \\ \sqrt{N_1N_2} & N_2 \end{pmatrix}$, $K = \begin{pmatrix} K_1 & -K_{12} \\ -K_{12} & K_2 \end{pmatrix}$ and $\omega_c = \frac{eB}{m^*}$, N_1 and N_2 are subbands' densities, $K1$ and $K2$ are intra-subband scattering rates, the K_{12} is inter-subband scattering rate, m^* is the effective mass of the carrier. We fit this theory to the data of Fig. 5.14 to get parameters K_1, K_2 and K_{12}, those values versus temperature T are displayed in Fig. 5.18 and 5.19.

We performed a parabolic fit for the intra subband scattering rate. It reveals that $K_1, K_2 \sim T^2$, while the previous analysis (Fig. 5.15) shows resistivity ρ_{xx} is linear in T in the range of 0.4 K < T < 2 K. This may mean that the resistivity is not dominated by intra-subband scattering, and the inter-subband scattering could play an important role in resistivity.

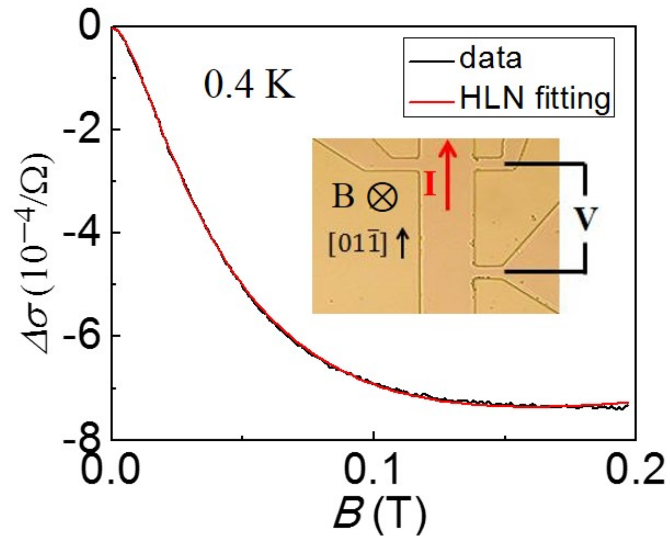

Figure 5.16: One HLN fit for the data of antilocalization on a Hall bar n material M423 at 0.4 K.

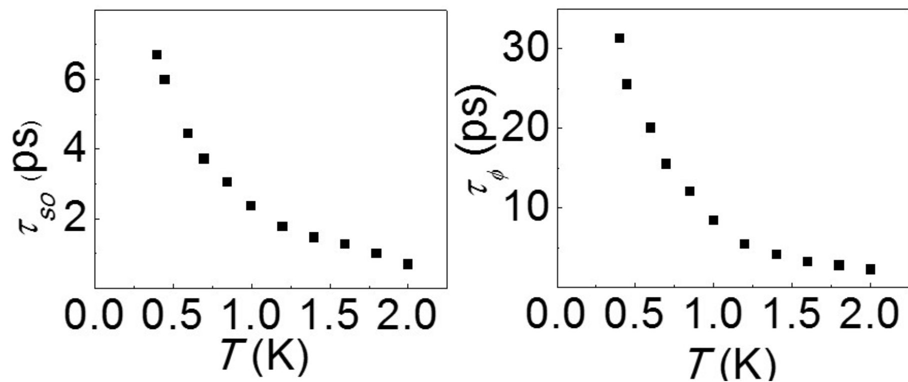

Figure 5.17: Temperature dependence of τ_{SO} and τ_{ϕ}.

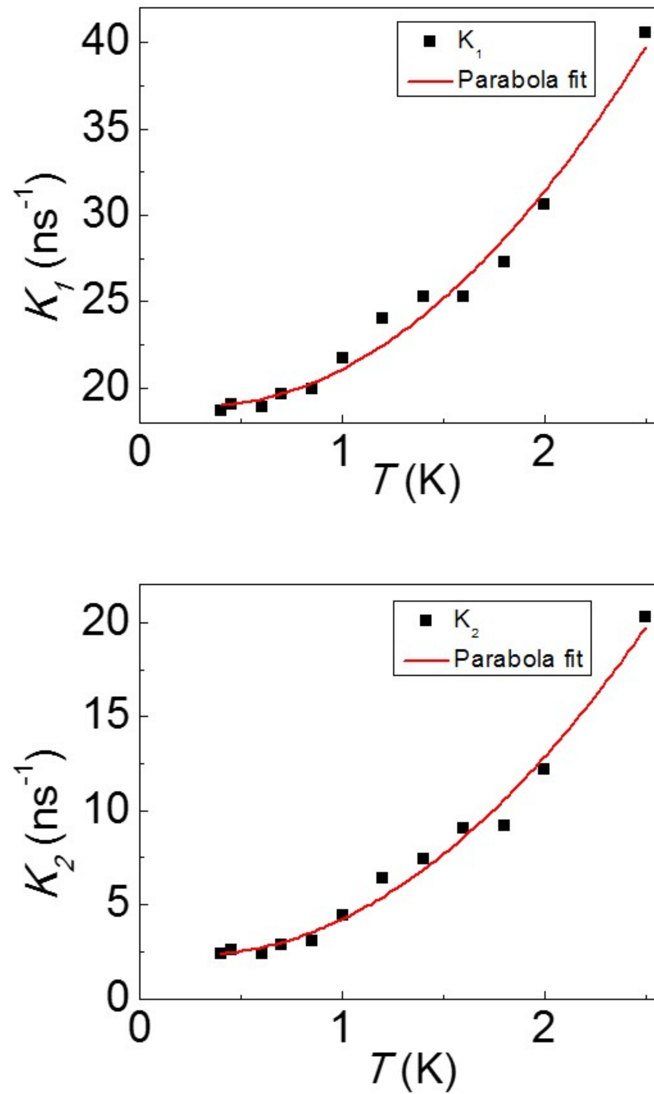

Figure 5.18: Intra-subband scattering rates K_1 and K_2 versus temperature T. The red line is a parabolic fit of temperature.

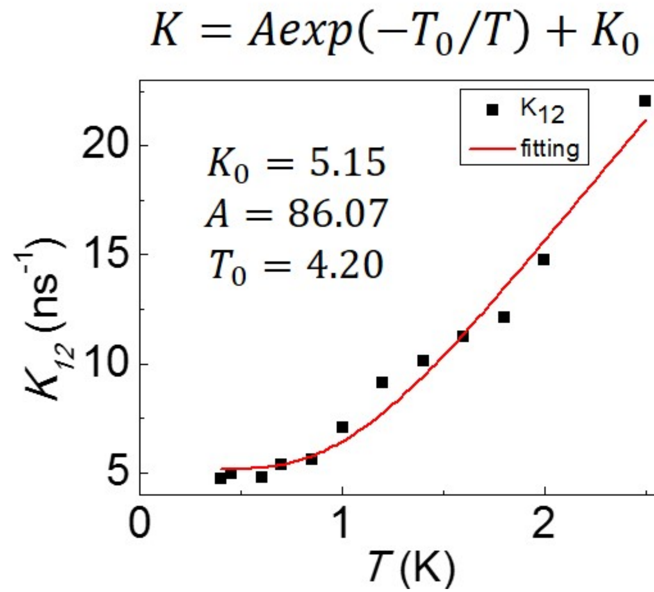

Figure 5.19: Inter-subband scattering rates K_{12} versus temperature T. An exponential model is applied to the data to obtain the activation characteristic energy between the two subbands.

An exponential model $K = Aexp(-T_0/T)+K_0$ is introduced for the inter-subband scattering rate to get the activation characteristic energy $E_0 = k_BT_0$ of the two subbands. We obtained $T_0 = 4.2$ K, and $E_0 \approx 0.36$ meV. This value is comparable to the heavy hole subband splitting energy 0.50 meV. The saturation of K_1, K_2 and K_{12} at low temperature is not fully understood so far by us.

The situation of the Q1D wires is more complicated. The 2D HLN and 2D multiband scattering are not suitable for this Q1D case. Figure 5.20 shows the temperature dependence of magnetoresistance in the Q1D wires. The shape of those curves are consistent with antilocalization under strong SOI. We tried to apply a model suitable for 1D with specular boundary scattering. The modified 1D HLN theory is described as [76, 92]

$$\Delta\sigma(B) = -\alpha\frac{e^2}{hL}\left(\sum_{m=\pm1,0}\tilde{L}_{1m} - \tilde{L}_{00}\right) \tag{5.7}$$

where $\tilde{L}_{1m}$ represents the triplet length, $\tilde{L}_{00}$ is the singlet length and L is the length of the wire. The triplet and singlet lengths in wires are given by [93]

$$\tilde{L}_{sm} = \left(L_\phi^{-1} + \nu_{sm}L_{SO}^{-2} + L_B^{-2}\right)^{-1/2} \tag{5.8}$$

with $\nu_{1\pm1} = 0.5$, $\nu_{10} = 1$, and $\nu_{00} = 0$. The 1D magnetic length is $L_B = l_m\sqrt{1+3l^2/w^2}$, where $l_m = \sqrt{\frac{\hbar}{eB}}$ represents the magnetic length in 2D and 3D. However, in this ballistic hole system, the mean free path is much greater than the wire width, we prefer to use the result for ballistic wires first introduced by Beenakker [76] in weak localization theory. The triplet and singlet lengths in ballistic Q1D wires become

$$\begin{aligned}\tilde{L}_{sm} = &\left(L_\phi^{-1} + \nu_{sm}L_{SO}^{-2} + L_B^{-2}\right)^{-1/2} \\ &- \left(L_\phi^{-1} + \nu_{sm}L_{SO}^{-2} + L_B^{-2} + 2l_e^{-2}\right)^{-1/2}\end{aligned} \tag{5.9}$$

where $\nu_{1\pm1} = 0.5$, $\nu_{10} = 1$, and $\nu_{00} = 0$ as before. In ballistic Q1D wires, L_B is expressed as

$$L_B = l_m\sqrt{\frac{C_1 l_m^2 l_e}{w^3} + \frac{C_2 l_e^2}{w^2}} \tag{5.10}$$

The values of C_1 and C_2 depend on whether the boundary scattering is specular or diffusive, for specular condition $C_1 = 4.75$ and $C_2 = 2.4$.

In order to extract the information about L_ϕ and L_{SO}, we fit the experimental data of Fig. 5.20 to Eq. 5.7. However, the result is imperfect as shown in Fig. 5.21. There are multiple reasons for this mismatch between theory and experimental data. The theory is derived for an electron system with spin 1/2, the experimental data is collected from a hole system with spin 3/2; hole-hole interaction is different from electron interaction; there may exist inter subband scattering which is not considering in the theory.

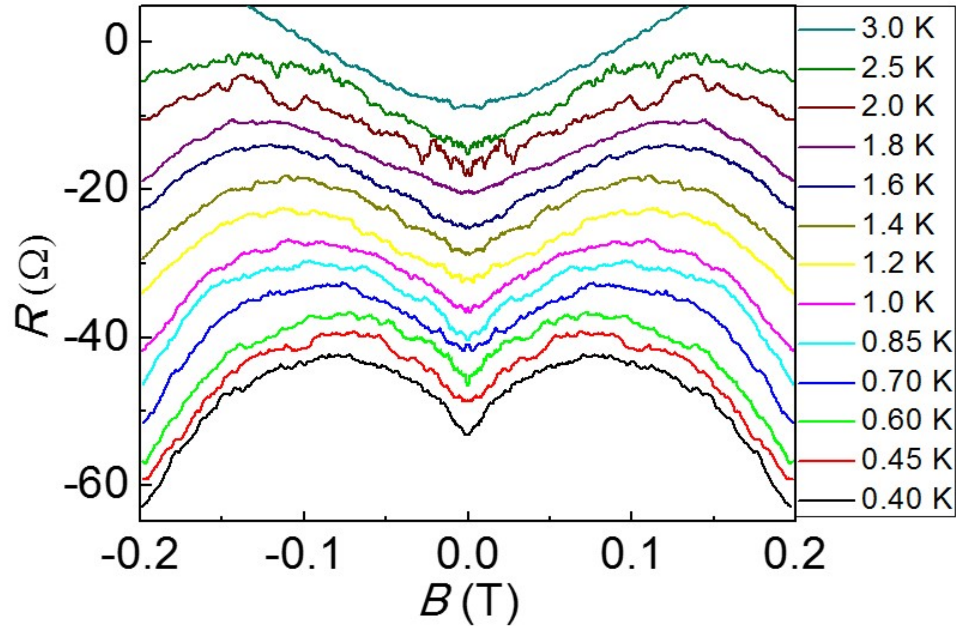

Figure 5.20: Temperature dependence of magnetoresistance of Q1D wires. Temperature varies from 0.4 K to 3.0 K, curves are offset for clarity. The typical value of R is about 800 Ω at zero magnetic field.

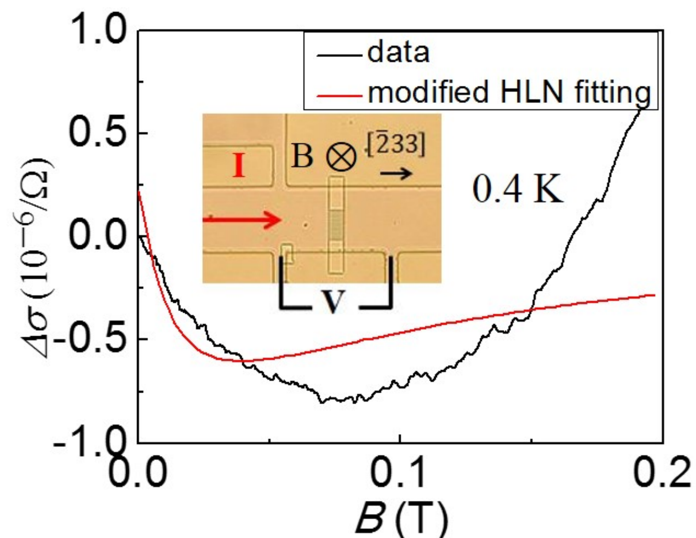

Figure 5.21: 1D antilocalization fit of experimental data. Inset shows the measurement configuration.

5.3.2 Hall bar and thin wire on material 94121

This device is designed to investigate weak localization and Altshuler-Aronov-Spivak (AAS) oscillation. It has two Q1D wires with antidots to introduce artificial impurities in the ballistic system. We didn't observed what we expected, however, there is no harm to elaborate what we observed with this device and to learn that such high quality pure ballistic system material yields unused results in the electronic transport coherence regime. This is highly due to the fact that ballistic transport features dominate over quantum coherent transport features. For this material, two trials were made, one without back gate and one with back gate.

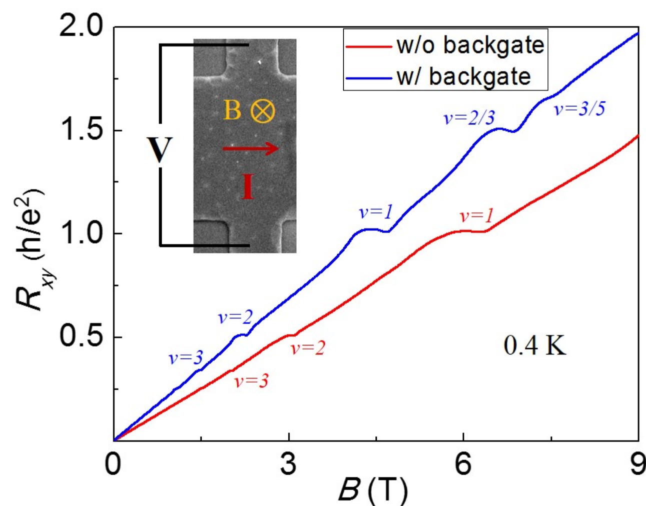

Figure 5.22: Quantum Hall effect in 94121 p-type C-doped GaAs/$Al_{0.24}Ga_{0.76}As$ heterostructure at 0.4 K, lower red line shows the result collected from the sample without back gate, upper blue line shows the result collected from the sample with back gate. Filling factors are marked on the corresponding plateaus. The inset graph shows the measurement configuration.

Figure 5.22 shows the quantum Hall effect in 94121 p-type C-doped GaAs/$Al_{0.24}Ga_{0.76}As$ heterostructure at 0.4 K. The interesting phenomenon is that fractional quantum Hall effect (the upper blue line) was observed when a back gate is applied to this device, which was also observed in a similar material [83].

We investigated the magnetoresistance of the wire pattern carefully from low field to high field. The device only gave some telegraph noise and universal conductance fluctuations (UCFs) (those could be noise as well, however, none contradiction observations, so we assume there are UCFs.). There is no obvious evidence of weak localization and energy band splitting, thus we cannot used the previous antilocalization theories and multiband scattering model. There are several reasons for this result. The 94121 heterostructure's quantum

well is buried deeper than the M423 heterostructure. This fact increases the difficulty of fabrication for material 94121, thus the quality of the sample is not guaranteed. While the 94121 heterostructure's hole mobility is greater, its hole density is lower than in M423, this means the hole-hole interaction is stronger that in M423. We tried an autocorrelation method to analyze the temperature dependence of UCFs and extract the phase coherence length. Fig. 5.23 shows the magnetoresistance of the 2 μm width wire with magnetic field from 1 T to 4 T at different temperatures 2.0 K, 1.0 K and 0.4 K. UCFs ride over the base shape.

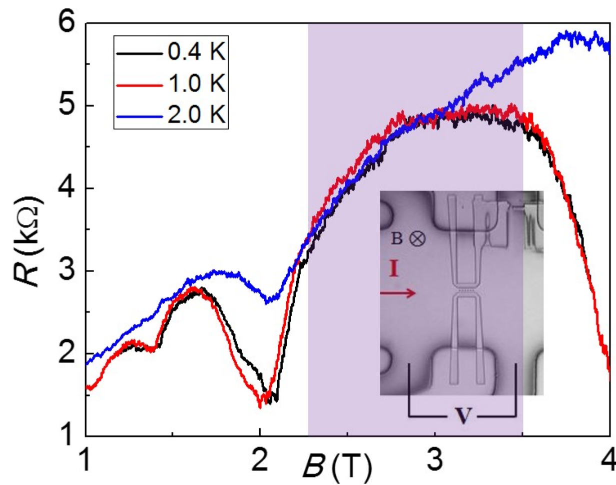

Figure 5.23: Magnetoresistance of the 2 μm width wire with magnetic field from 1 T to 4 T at different temperatures 2.0 K, 1.0 K and 0.4 K corresponding to curves from up to down. The inset shows the measurement configuration. The shadowed part is analyzed by autocorrelation in order to figure out the phase coherence length l_ϕ.

The quantity to be calculated in this autocorrelation method is correlation function

$$C_G(\Delta B) = \langle \delta G(B) \delta G(B + \Delta B) \rangle \tag{5.11}$$

where $\delta G(B) = G(B) - \langle G(B) \rangle$, $G(B)$ is the conductance of the Q1D structure in a magnetic field B, $\langle \delta G(B) \delta G(B + \Delta B) \rangle$ denotes the ensemble average value of $\delta G(B) \delta G(B + \Delta B)$, and thus $C_G(\Delta B)$ is B independent. Fig. 5.24 shows the calculated results. There is a way to relate this correlation function quantity to phase coherence length [94, 95],

$$\delta G = \frac{1}{\beta} \frac{e^2}{h} \sqrt{\frac{12(l_\phi/L)^3}{1 + [9/(2\pi)](l_\phi/L_T)^2}} \tag{5.12}$$

where l_ϕ is phase coherence length, $L_T = 11$ μm is thermal length [95], β is a constant factor, $\delta G = \sqrt{C_G(0)}$. With δG and Eq. 5.12, the phase coherence length l_ϕ could be obtained, shown in Fig. 5.25.

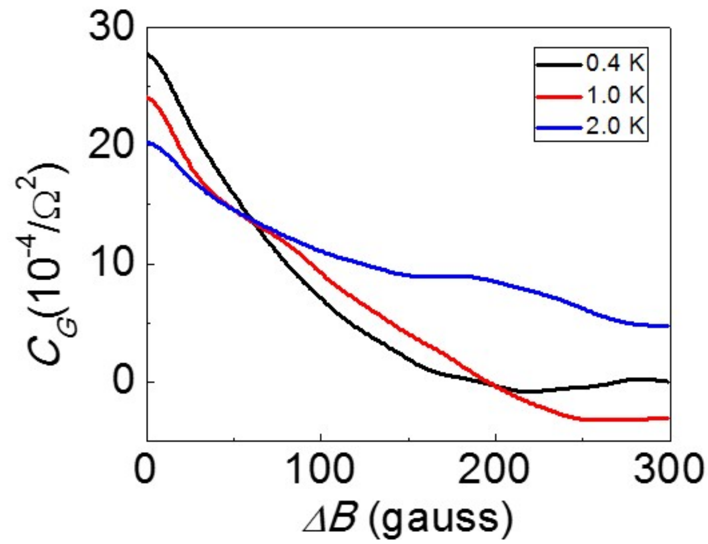

Figure 5.24: The autocorrelation function over magnetic field from 2.8 T to 3.0 T of a Q1D wire at different temperatures 0.4 K, 1.0 K and 2.0 K.

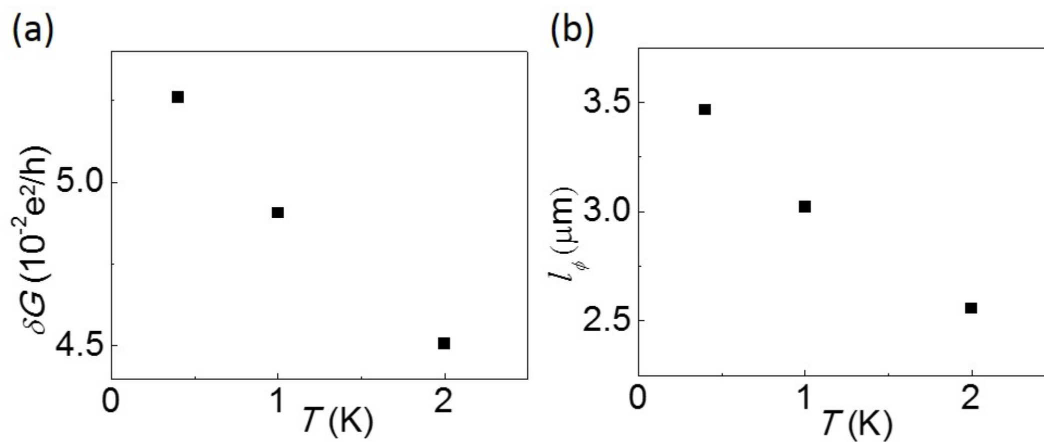

Figure 5.25: Calculated δG (a) and phase coherence length l_ϕ (b) versus T.

5.3.3 Antidot array on material 94121

This device is used to study the commensurability oscillations (COs) in the 2DHS of material 94121. The pattern of this device is an antidot array which was introduced in section 5.2. By studying the temperature dependence of COs resulting from one antidot, the temperature dependence of relative electron scattering rate was obtained.

The grid area has a different hole density and hole mobility from the bare Hall bar. At 0.4 K, the hole density is about $p = 9.5 \times 10^{14}$ m^{-2}, and the corresponding mobility is about $\mu = 8.7$ m^2/Vs.

Four-contact measurements of the longitudinal resistance of the antidot grid were made at different temperatures, ranging from 0.4 K to 3 K using standard lock-in techniques. Figure 5.26 shows the magnetoresistance of the grid area with a quadratic background subtraction at different temperatures. At low field, there are ballistic transport peaks near $B = \pm 0.1$ T and $B = \pm 0.025$ T. We call the peak at 0.1 T P1 and the peak at 0.025 T P2. The cyclotron orbit radius of P1 is $r_{P1} = 0.6$ μm and the cyclotron orbit radius of P2 is $r_{P2} = 2.5$ μm. This means that the P1 is caused by the electron localized around one antidot and the P2 is caused by the electron going around about a 9 antidots square, roughly matching the grid spatial periodicity.

The properties of the ballistic transport peaks as in Fig. 5.26 were studied before in different materials [96, 97]. Here I used the method in these literature [96, 97] to analyze the data in Fig. 5.26. The ballistic transport peak P and ballistic scattering rate τ_β follows

$$P1 \sim exp(-2\pi/\omega_c\tau_\beta) \tag{5.13}$$

where P1 denotes the amplitude of the peak P1, ω_c is the cyclotron frequency calculated at the field of peak P1, τ_β is the ballistic scattering rate. Since the proportional factor is not known, this relation only allows us to get the scattering rate with a constant offset which is chosen as the scattering rate at $T = 0.4$ K. The relative ballistic scattering rate $\Delta\tau_\beta$ is defined as

$$\Delta(1/\tau_\beta) = 1/\tau_\beta(T) - 1/\tau_\beta(T = 0.4 \text{ K}) \tag{5.14}$$

Figure 5.27 shows the temperature dependence of the relative ballistic scattering rate. Below 1.0 K, scattering rate is almost saturated, then it increases significantly as the temperature goes up above 1.0 K. $\Delta(1/\tau_\beta)$ roughly follows a T^2 law.

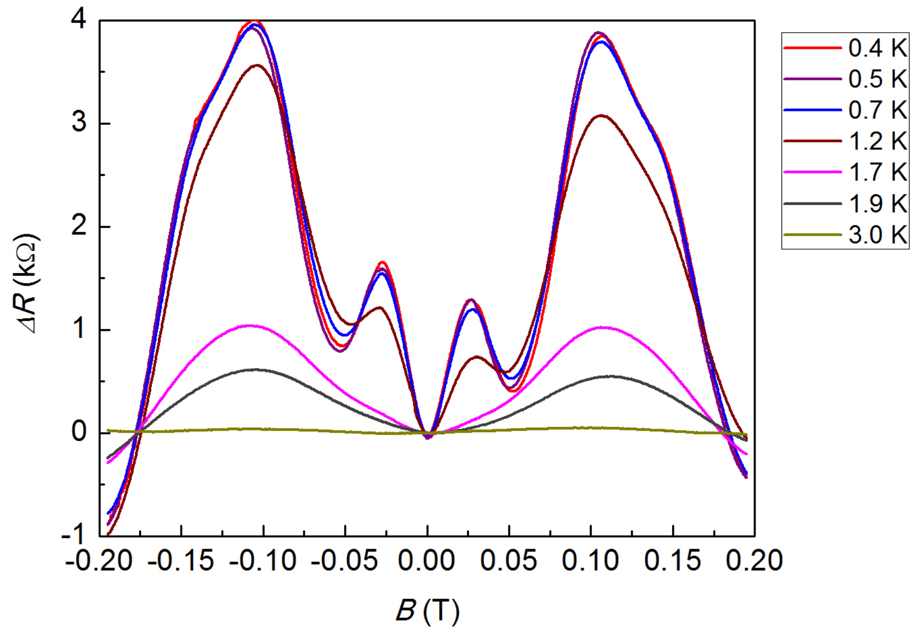

Figure 5.26: Ballistic transport peaks after subtracting a quadratic background at different temperatures of the grid area. From top to bottom: 0.4 K, 0.5 K, 0.7 K, 1.2 K, 1.7 K, 1.9 K, 3.0 K.

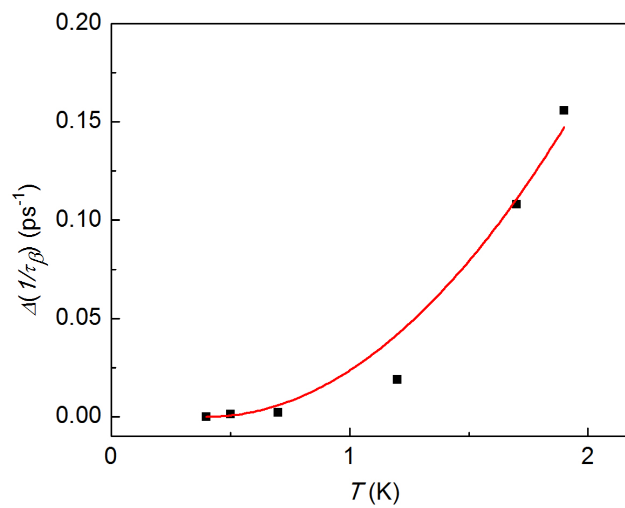

Figure 5.27: Temperature dependence of the relative ballistic scattering rate $\Delta(1/\tau_\beta)$ defined as Eq. 5.14. The red solid line is a quadratic fit to the data.

Chapter 6

Conclusions

Quantum interference is an important method to study the properties of mesoscopic systems. In this dissertation, we present quantum interference studies of confined 2D systems in InGaAs and GaAs. Both 2D electron systems and 2D hole systems are studied. They have relatively high carrier density and mobility, and are located about several tens to hundreds of nanometers beneath the semiconductor surface. Further, we used various fabrication techniques to laterally define structures on the 2D systems to form confined systems. The techniques include photolithgraphy, electron-beam lithography, wet etching, dry etching, chemical deposition, etc. The structures we studied are single Aharonov-Bohm (AB) rings, ring arrays, Hall bars, narrow wires, anti-dot arrays, etc.

In the 2D electron system, two types of interferometers are made, single ring (AB ring) and ring array. They are both confined ballistic systems. The single ring interferometer shows Mach-Zehnder interferometry, and yields AB oscillation with varying magnetic field. The ring array shows a combination of Mach-Zehnder interferometry and Sagnac-type interferometry, yielding AB oscillations and Altshuler-Aronov-Spivak (AAS) oscillations. The AB oscillations have a magnetic flux periodicity of h/e, and are sensitive to spatial symmetry. The AAS oscillations have a magnetic flux periodicity of $h/2e$, and are based on time-reversal symmetry.

In the single ring interferometer, AB oscillations were observed in a wide range of magnetic field, from 0 T to above 0.3 T. A clear modulation of the AB oscillation amplitude with magnetic field was observed as well. Fourier transformation was used to analyze the properties related to AB oscillations. The oscillation periodicity in magnetic field matches the AB prediction for the design. By determining the critical magnetic field of the decay of the autocorrelation function, we derived the quasi-period of the AB oscillation amplitude modulation. The AB oscillations spectrum is expected to be randomized when magnetic flux threading through the interference arms varies by h/e, due to change in mesoscopic representation (another example of this phenomenon are universal conductance fluctuations). Another method assumes that the arms of the ring have a finite width which tends to give

different orbit radii. The modulation of the oscillation is generated by the overlap of oscillations with different frequencies. Both autocorrelation function and multiple modes point to the finite width of the interferometer arms as the origin of the modulation. To study the temperature and current dependency of the AB oscillation amplitude, we introduced an energy scale, the Thouless energy, which depicts a critical excitation energy of a system. The dependence studies show the existence of critical excitation energies consistent with the Thouless energy. Quantum coherence in the mesoscopic interferometer is reduced for thermally or electrically induced excitations beyond the system's Thouless energy, with a concomitant decrease in the AB oscillation amplitude.

Further, an in-plane magnetic field was applied to the single ring interferometer. The heterostructure has a strong spin-orbit interaction (SOI). The Rashba coefficient α was obtained by analysis of the Shubnikov-de Haas oscillation. In-plane Zeeman effect induced Berry's phase and Aharonov-Casher (AC) phase change were studied. The effect of Berry's phase and AC phase in frequency of oscillations is negligible compared to AB effect, thus we cannot observe them directly. Berry's phase and AC phase are combined in the total phase. When an in-plane magnetic field is sufficiently high, it modifies the condition for Berry's phase and AC phase to accumulate. The total phase is then modified in a complex way and affects the amplitude of AB oscillations. The Fourier spectrum of AB oscillations with high in-plane magnetic field is more broad and fuzzy. The critical Zeeman energy is consistent with the Thouless energy as well.

In the ring array interferometer, quantum interference is strong. AB oscillations exist above 2.0 T. The strong AB oscillations allow us to determine the phase coherence length directly from the Fourier transformation of the quantum interference. Similar to the AB oscillation studied in the single ring interferometer, this ring array was used to study time-reversal symmetry breaking due to local magnetic flux. The mesoscopic dephasing length scale describing time-reversal symmetry breaking was measured using this ballistic interferometer array. This interferometer array has both AB oscillations and AAS oscillations. As in the single ring interferometer, the magnetic field periodicity of the AB oscillations matches the AB prediction of the design. The magnetic field periodicity of the AAS oscillations is about half of the value of the AB oscillations, which corroborates the existence of AAS oscillations. Fourier transformations over short magnetic field segments were used to quantify the amplitudes of oscillations. The component of the AB oscillations does not have a monotonic decay with increasing magnetic field, which keeps to a high value even above 2.0 T. The component of the AAS oscillations decays fast over magnetic field. When the magnetic field is above 0.16 T, it is hardly resolved from the background. As AAS oscillations rely on time-reversal symmetry, the decay of the AAS oscillations indicates time-reversal symmetry breaking. This result confirms that the AB oscillations are unaffected by time-reversal symmetry breaking under an applied magnetic field, whereas AAS oscillation is erased by time-reversal symmetry breaking. An experimental effective magnetic length was obtained from the intensity of the AAS oscillations, which was compared to predictions from several theoretical models. The theoretical models can calculate effective magnetic length directly

from magnetic field B. Our study allows experimental determination of dephasing length associated with time-reversal symmetry breaking, which is equivalent to effective magnetic length.

In the 2D hole system, the cubic Rashba coefficient β was calculated from the beat of low field Shubnikov-de Haas oscillation. Antilocalization of a 2D Hall bar and a quasi-1D wire was also studied. The 2D Hikami-Larkin-Nagaoka (HLN) theory and intersubband scattering hypothesis were used to analyze the 2D antilocalization results. Both methods gave reasonable results, but didn't completely explain the experimental data. The antilocalization of quasi-1D wires is more complicated, and the modified 1D HLN theory didn't fit data well. A possible reason: the theories are based on electron systems with low carrier interactions, but the experiments were performed in a hole system with strong interaction due to the low density in the heterostructure studied.

The C-dope 2D hole system we used turned out less suitable for quantum interference experiments also, likely due to the dominant of ballistic transport effects. Universal conductance fluctuations of a wire and commensurability oscillations of an anti-dot array were studied.

Bibliography

[1] Y. Aharonov and D. Bohm, *Phys. Rev.* **115**, 485 (1959)

[2] Y. Aharonov and D. Bohm, *Phys. Rev.* **123**, 1511 (1961)

[3] R. G. Chambers, *Phys. Rev. Lett.* **5**, 3 (1960)

[4] Akira Tonomura, Tsuyoshi Matsuda, Byo Suzuki, Akira Fukuhara, Nobuyuki Osakabe, Hiroshi Umezaki, Junji Endo, Kohsei Shinagawa, Yutaka Sugita, and'Hideo Fujiwara, *Phys. Rev. Lett.* **48**, 1443 (1982)

[5] Nobuyuki Osakabe, Tsuyoshi Matsuda, Takeshi Kawasaki, Junji Endo, and Akira Tonomura, *Phys. Rev. A* **34**, 815 (1986)

[6] Akira Tonomura, Tsuyoshi Matsuda, Takeshi Kawasaki, Junji Endo, and Nobuyuki Osakabe, *Phys. Rev. Lett.* **54**, 60 (1985)

[7] R. A. Webb, S. Washburn, C. P. Umbach, and R. B. Laibowitz, *Phys. Rev. Lett.* **54**, 2696 (1985)

[8] Al'tshuler B. L., Aronov A. G., Spivak B. Z. , *JETP lett.* **33**, 94 (1981)

[9] S. Datta and S. Bandyopadhyay, *Phys. Rev. Lett.* **58**, 717 (1987)

[10] C. H. Wu and G. Mahler, *Phys. Rev. B* **48**, 5012 (1991)

[11] A. V. Maslov and D. S. Citrin, *Phys. Rev. B* **67**, 121304(R) (2003)

[12] A. F. Morpurgo, J. P. Heida, T. M. Klapwijk, B. J. van Wees, and G. Borghs, *Phys. Rev. Lett.* **80**, 1050 (1998)

[13] Jeng-Bang Yau, E. P. De Poortere, and M. Shayegan, *Phys. Rev. Lett.* **80**, 146801 (2002)

[14] M. V. Berry, *Proc. R. Soc. Lond. A* **392**, 45 (1984)

[15] Y. Aharonov and A. Casher, *Phys. Rev. Lett.* **53**, 319 (1984)

[16] Gerd Bergmann, *Phys. Rev. B* **28**, 2914 (1983)

[17] C. W. J. Beenakker and H. van Houten, *Solid State Physics* **44**, 1 (1991)

[18] Gerd Bergman, *Phys. Rev. Lett.* **48**, 1046 (1982)

[19] A. B. Fowler, A. Hartstein, and R. A. Webb, *Phys. Rev. Lett.* **48**, 196 (1982)

[20] P. A. Lee and A. Douglas Stone, *Phys. Rev. Lett.* **55**, 1622 (1985)

[21] P. A. Lee, A. Douglas Stone, and H. Fukuyama, *Phys. Rev. B* **35**, 1039 (1987)

[22] A. Douglas Stone, *Phys. Rev. Lett.* **54**, 2692 (1985)

[23] *Model 124A Lock-in Amplifier*, Princeton Applied Research Corporation

[24] Yang Ji, Yunchul Chung, D. Sprinzak, M. Heiblum, D. Mahalu and Hadas Shtrikman *Nature* **422** 415 (2003)

[25] Preden Roulleau, F. Portier, and P. Roche, A. Cavanna, G. Faini, U. Gennser, and D. Mailly, *Phys. Rev. Lett.* **100** 126802 (2008)

[26] L. V. Litvin, H.-P. Tranitz, W. Wegscheider, and C. Strunk, *Phys. Rev. B* **74**, 033315 (2007)

[27] L. V. Litvin, A. Helzel, H.-P. Tranitz, W. Wegscheider, and C. Strunk, *Phys. Rev. B* **78**, 075303 (2008)

[28] J. P. Bird, K. Ishibashi, M. Stopa, Y. Aoyagi, and T. Sugano, *Phys. Rev. B* **50**, 14983 (1994)

[29] Nobuyuki Osakabe, Tsuyoshi Matsuda, Takeshi Kawasaki, Junji Endo, and Akira Tonomura, *Phys. Rev. A* **34**, 815 (1986)

[30] R. G. Chambers, *Phys. Rev. Lett.* **5**, 3 (1960)

[31] Akira Tonomura, Tsuyoshi Matsuda, Byo Suzuki, Akira Fukuhara, Nobuyuki Osakabe, Hiroshi Umezaki, Junji Endo, Kohsei Shinagawa, Yutaka Sugita, and'Hideo Fujiwara, *Phys. Rev. Lett.* **48**, 1443 (1982)

[32] C. P. Umbach, C. Van Haesendonck, R. B. Laibowitz, S. Washburn, and R. A. Webb, *Phys. Rev. Lett.* **56**, 386 (1986)

[33] A. Yacoby, R. Schuster, and M. Heiblum, *Phys. Rev. B* **53**, 9583 (1996)

[34] M. A. Castellanos-Beltran, D. Q. Ngo, W. E. Shanks, A. B. Jayich, and J. G. E. Harris, *Phys. Rev. Lett.* **110**, 156801 (2013)

[35] Eran Ginossar, Leonid I. Glazman, Teemu Ojanen, Felix von Oppen, William E. Shanks, Ania C. Bleszynski-Jayich, and J. G. E. Harris, *Phys. Rev. B* **81**, 155448 (2010)

[36] Y. Yamauchi, M. Hashisaka, S. Nakamura, K. Chida, S. Kasai, T. Ono, R. Leturcq, K. Ensslin, D. C. Driscoll, A. C. Gossard, and K. Kobayashi, *Phys. Rev. B* **79**, 161306 (2009)

[37] J T Edwards and D J Thouless, *J. Phys. C: Solid State Phys.* **5**, 807 (1972)

[38] Harmans C, *Mesoscopic Physics, an Introduction* (lecture notes, Delft University of Technology) pp 19, 99, 102 (2003)

[39] L C Mur, C J P M Harmans and W G van der Wiel, *New J. Phys.* **10**, 073031 (2008) 1too

[40] C. Kurdak, A. M. Chang, A. Chin, and T. Y. Chang, *Phys. Rev. B* **46**, 6846 (1992)

[41] Winkler R, *Spin-orbit coupling effects in two-dimensional electron and hole systems* New York: Springer 2003

[42] Diego Frustaglia and Klaus Richter, *Phys. Rev. B* **69**, 235310 (2004)

[43] Fumiya Nagasawa, Diego Frustaglia, Henri Saarikoski, Klaus Richter and Junsaku Nitta, *Nat. Commun.* **4**, 2526 (2013)

[44] Tie-Zheng Qian and Zhao-Bin Su, *Phys. Rev. Lett.* **72**, 2311 (1994)

[45] Junsaku Nitta, Frank E. Meijer, and Hideaki Takayanagi, *Appl. Phys. Lett.* **75**, 695 (1999)

[46] C. R. Hagen, *Phys. Rev. Lett.* **64**, 2347 (1990)

[47] Holstein B. R., *Am. J. Phys.* **57**, 1079 (1988)

[48] S L Ren, J J Heremans, C K Gaspe, S Vijeyaragunathan, T D Mishima and M B Santos, *J. Phys.: Condens. Matter* **25**, 435301 (2013)

[49] M. König, A. Tschetschetkin, E. M. Hankiewicz, Jairo Sinova, V. Hock, V. Daumer, M. Schäfer, C. R. Becker, H. Buhmann, and L. W. Molenkamp, *Phys. Rev. Lett.* **96**, 076804 (2006)

[50] Fanming Qu, Fan Yang, Jun Chen, Jie Shen, Yue Ding, Jiangbo Lu, Yuanjun Song, Huaixin Yang, Guangtong Liu, Jie Fan, Yongqing Li, Zhongqing Ji, Changli Yang, and Li Lu, *Phys. Rev. Lett.* **107**, 016802 (2011)

[51] J. J. Lin and J. P. Bird, *J. Phys.: Condens. Matter* **14**, R501 (2002)

[52] F. P. Milliken, S. Washburn, C. P. Umbach, R. B. Laibowitz, and R. A. Webb, *Phys. Rev. B* **36**, 4465(R) (1987)

[53] A. E. Hansen, A. Kristensen, S. Pedersen, C. B. Sorensen, and P. E. Lindelof, *Phys. Rev. B* **64**, 045327 (2001)

[54] Aronov A. G. and Sharvin Yu V., *Rev. Mod. Phys.* **59**, 755 (1987)

[55] Buttiker M., *Phys. Rev. Lett.* **57**, 1761 (1986)

[56] A. D. Benoit, S. Washburn, C. P. Umbach, R. B. Laibowitz, and R. A. Webb, *Phys. Rev. Lett.* **57**, 1765 (1986)

[57] Felicien Schopfer, Francois Mallet, Dominique Mailly, Christophe Texier, Gilles Montambaux, Christopher Bauerle, and Laurent Saminadayar, *Phys. Rev. Lett.* **98**, 026807 (2007)

[58] M. Ferrier, L. Angers, A. C. H. Rowe, S. Gueron, H. Bouchiat, C. Texier, G. Montambaux, and D. Mailly, *Phys. Rev. Lett.* **93**, 246804 (2004)

[59] Ludwig T. and Mirlin A. D., *Phys. Rev. B* **69**, 193306 (2004)

[60] F. E. Meijer, A. F. Morpurgo, T. M. Klapwijk, T. Koga, and J. Nitta, *Phys. Rev. B* **69**, 035308 (2004)

[61] Stone D. A. and Imry Y., *Phys. Rev. Lett.* **56**, 189 (1986)

[62] C. P. Umbach, C. Van Haesendonck, R. B. Laibowitz, S. Washburn, and R. A. Webb,*Phys. Rev. Lett.* **56**, 386 (1986)

[63] R.B. Lillianfeld, R.L. Kallaher, J.J. Heremans, Hong Chen, N. Goel, S.J. Chung, M.B. Santos, W. Van Roy, G. Borghs, *Phys Procedia* **3**, 1231 (2010)

[64] Doucot B. and Rammal R., *Phys. Rev. Lett.* **55**, 1148 (1985)

[65] G. J. Dolan, J. C. Licini, and D. J. Bishop, *Phys. Rev. Lett.* **56**, 1493 (1986)

[66] M. Ferrier, A. C. H. Rowe, S. Gueron, H. Bouchiat, C. Texier, and G. Montambaux, *Phys. Rev. Lett.* **100**, 146802 (2008)

[67] Christophe Texier, Pierre Delplace, and Gilles Montambaux, *Phys. Rev. B* **80**, 205413 (2009)

[68] M. Treiber, O. M. Yevtushenko, F. Marquardt, J. von Delft, and I. V. Lerner, *Phys. Rev. B* **80**, 201305(R) (2009)

[69] B. L. Al'Altshuler, A. G. Aronov, and A. Y. Zyuzin, *Sov. Phys. JEPT* **59**, 415 (1984)

[70] R. L. Kallaher, J. J. Heremans, W. Van Roy, and G. Borghs, *Phys. Rev. B* **88**, 205407 (2013)

[71] B. Hackens, S. Faniel, C. Gustin, X. Wallart, S. Bollaert, A. Cappy, and V. Bayot, *Phys. Rev. Lett.* **94**, 146802 (2005)

[72] Akkermans Eric and Montambaux Gilles, *Mesoscopic Physics of Electrons and Photons*, (Cambridge University Press) (2007)

[73] Altshuler B. L. and Aronov A. G., *J. Exp. Theor. Phys.* **33**, 499 (1981)

[74] Bergmann G., *Phys. Rep.* **207**, 1 (1984)

[75] Dugaev V. K. and Khmelnitskii D. E., *Sov. Phys. JEPT* **59**, 1038 (1984)

[76] Beenakker C. W. J. and van Houten H., *Phys. Rev. B* **38**, 3232 (1988)

[77] S. Hikami, A. I. Larkin and Y. Nagaoka, *Prog. Theor. Phys.* **63**, 707 (1980)

[78] S. V. Iordanskii, Y. B. Lyanda-Geller and G. E. Pikus, *JEPT Lett.* **60**, 206 (1994)

[79] S. Kettemann, *Phys. Rev. Lett.* **98**, 176808 (2007)

[80] R. Winkler, *Spin-Orbit Coupling Effects in Two-Dimensional Electron and Hole Systems*, Springer Tracts in Modern Physics, Vol. 191 (Springer-Verlag, Berlin, 2003)

[81] H. L. Stormer, Z. Schlesinger, A. Chang, D. C. Tsui, A. C. Gossard, and W. Wiegmann, *Phys. Rev. Lett.* **51**, 126 (1983)

[82] J. P. Eisenstein, H. L. Stormer, V. Narayanamurti, A. C. Gossard, and W. Wiegmann, *Phys. Rev. Lett.* **53**, 2579 (1984)

[83] B. Grbic, C. Ellenberger, T. Ihn, K. Ensslin, D. Reuter and A. D. Wieck, *Appl. Phys. Lett.* **85**, 2277 (2004)

[84] B. Habib, E. Tutuc, S. Melinte, M. Shayegan, D. Wasserman, S. A. Lyon, and R. Winkler, *Phys. Rev. B* **69**, 113311 (2004)

[85] B Habib, M Shayegan and R Winkler, *Semicond. Sci. Technol.* **24**, 064002 (2009)

[86] Boris Grbic, Renaud Leturcq, Thomas Ihn, Klaus Ensslin, Dirk Reuter, and Andreas D. Wieck, *Phys. Rev. B* **77**, 125312 (2008)

[87] H. Noh, M. P. Lilly, D. C. Tsui, J. A. Simmons, E. H. Hwang, S. Das Sarma, L. N. Pfeiffer, and K. W. West, *Phys. Rev. B* **68**, 165308 (2003)

[88] Gabor Zala, B. N. Narozhny, and I. L. Aleiner, *Phys. Rev. B* **64**, 214204 (2001)

[89] Shinobu Hikami, Anatoly I. Larkin, and Yosuke Nagaoka, *Prog. Theor. Phys.* **63**, 707 (1980)

[90] R. L. Kallaher, J. J. Heremans, N. Goel, S. J. Chung, and M. B. Santos, *Phys. Rev. B* **81**, 075303 (2010)

[91] E. Zaremba, *Phys. Rev. B* **45**, 14143 (1992)

[92] R. L. Kallaher, J. J. Heremans, N. Goel, S. J. Chung, and M. B. Santos, *Phys. Rev. B* **81**, 035335 (2010)

[93] S. Kettemann, *Phys. Rev. Lett.* **98**, 176808 (2007)

[94] C. W. J. Beenakker and H. van Houten, *Phys. Rev. B* **37**, 6544 (1988)

[95] Thomas Heinzel, *Mesoscopic Electronics in Solid State Nanostructures*, WILEY-VCH GmbH & Co.KGaA, Weinheim (2003)

[96] J. Heremans, B. K. Fuller, C. M. Thrush, and V. Bayot, *Phys. Rev. B* **54**, 2685 (1996)

[97] Hong Chen, J. J. Heremans, J. A. Peters, N. Goel, S. J. Chung, and M. B. Santos, *Appl. Phys. Lett.* **84**, 5380 (2004)